



UNIVERSITY OF LEEDS

This is a repository copy of *Tectonics of the Isua Supracrustal Belt 2: Microstructures Reveal Distributed Strain in the Absence of Major Fault Structures*.

White Rose Research Online URL for this paper:
<https://eprints.whiterose.ac.uk/170613/>

Version: Published Version

Article:

Zuo, J, Webb, AAG, Piaolo, S orcid.org/0000-0001-7723-8170 et al. (4 more authors)
(2021) *Tectonics of the Isua Supracrustal Belt 2: Microstructures Reveal Distributed Strain in the Absence of Major Fault Structures*. *Tectonics*, 40 (3). e2020TC006514. ISSN 0278-7407

<https://doi.org/10.1029/2020TC006514>

© 2021. American Geophysical Union. All Rights Reserved. This is an author produced version of an article, published in *Tectonics*. Uploaded in accordance with the publisher's self-archiving policy.

Reuse

Items deposited in White Rose Research Online are protected by copyright, with all rights reserved unless indicated otherwise. They may be downloaded and/or printed for private study, or other acts as permitted by national copyright laws. The publisher or other rights holders may allow further reproduction and re-use of the full text version. This is indicated by the licence information on the White Rose Research Online record for the item.

Takedown

If you consider content in White Rose Research Online to be in breach of UK law, please notify us by emailing eprints@whiterose.ac.uk including the URL of the record and the reason for the withdrawal request.



eprints@whiterose.ac.uk
<https://eprints.whiterose.ac.uk/>

Tectonics

RESEARCH ARTICLE

10.1029/2020TC006514

Key Points:

- Microstructures of the Isua supracrustal belt show two dominant opposing shear senses and quasiuniform strain intensities
- Deformation of the Isua supracrustal belt occurred under amphibolite facies conditions
- The Isua supracrustal belt could have formed via heat-pipe tectonics before ca. 3.7 Ga and deformed via a-type folding within ca. 3.66–3.5 Ga

Supporting Information:

- Supporting Information S1

Correspondence to:

J. Zuo and A. A. G. Webb,
jwzuo@connect.hku.hk;
aagwebb@hku.hk

Citation:

Zuo, J., Webb, A. A. G., Piazzolo, S., Wang, Q., Müller, T., Ramírez-Salazar, A., & Haproff, P. J. (2021). Tectonics of the Isua supracrustal belt 2: Microstructures reveal distributed strain in the absence of major fault structures. *Tectonics*, 40, e2020TC006514. <https://doi.org/10.1029/2020TC006514>

Received 10 SEP 2020

Accepted 28 JAN 2021

Tectonics of the Isua Supracrustal Belt 2: Microstructures Reveal Distributed Strain in the Absence of Major Fault Structures

Jiawei Zuo¹ , A. Alexander G. Webb¹ , Sandra Piazzolo² , Qin Wang³ , Thomas Müller^{2,4} , Anthony Ramírez-Salazar² , and Peter J. Haproff⁵ 

¹Division of Earth and Planetary Science and Laboratory for Space Research, University of Hong Kong, Hong Kong, China, ²School of Earth and Environment, University of Leeds, Leeds, UK, ³School of Earth Sciences and Engineering, State Key Laboratory for Mineral Deposits Research, Nanjing University, Nanjing, China, ⁴Geoscience Center, Department of Mineralogy, Georg-August-Universität Göttingen, Göttingen, Germany, ⁵Department of Earth and Ocean Sciences, University of North Carolina, Wilmington, NC, USA

Abstract Archean geological records are increasingly interpreted to indicate a ≤ 3.2 Ga initiation of plate tectonics on Earth. This hypothesis contrasts with dominant plate tectonic interpretations for the Eoarchean (ca. 4.0–3.6 Ga) Isua supracrustal belt (southwest Greenland). Alternatively, recent work shows the belt could have formed via heat-pipe tectonics. Predicted strain distributions across the belt vary between models. Plate tectonic models predict a dominant unidirectional shear sense, corresponding to subduction vergence, and strain localization within ~ 10 -m-scale shear zones. In contrast, the proposed heat-pipe model predicts two opposing shear senses, corresponding to opposite limbs of 0.1-m to km-scale a-type folds (i.e., sheath and curtain folds), with relatively equal strain distributed across the belt. Here, we present the first microstructure study using thin-section petrography and electron backscatter diffraction analysis on quartz of oriented samples from throughout the Isua supracrustal belt. Key findings are: (1) the Eoarchean Isua supracrustal belt was deformed at $\sim 500^{\circ}\text{C}$ – 650°C , with potential postdeformational recovery at similar or lower temperatures, (2) the spatial distribution of the two opposing shear senses which dominate the belt (top-to-southeast and top-to-northwest) appears to be random, and (3) the strain intensity across the belt appears to be quasiuniform as evidenced by the uniformly low (mostly < 0.1) M-indexes of quartz fabrics, such that no ≤ 100 -m-scale shear zones can be detected. Our findings are only consistent with the predictions of the heat-pipe model and do not require plate tectonics, so the geology of the belt is compatible with a ≤ 3.2 Ga initiation of plate tectonics.

1. Introduction

Plate tectonic theory is the most renowned solid-Earth geoscience discovery of the 20th century, and yet there is no consensus hypothesis for how and why plate tectonics developed on Earth (e.g., Gerya et al., 2015; Hansen, 2007; Rey et al., 2014; C. Tang et al., 2020). Similarly, there is little agreement as to what planetary cooling mechanism preceded plate tectonics (e.g., Collins et al., 1998; Hopkins et al., 2008; Moore & Webb, 2013; O'Neill & Debaille, 2014). Nonetheless, over roughly the past decade, an increasingly rich and diverse body of work has indicated a ca. 3.2–2.5 Ga onset of some form of subduction tectonics that was either episodic or continuous. This work includes isotopic (e.g., Naeraa et al., 2012), geochemical (e.g., M. Tang et al., 2016), petrological (e.g., Brown & Johnson, 2018), geological (e.g., Pease et al., 2008), geochronologic (e.g., Condie & Puetz, 2019), and paleomagnetic (Brenner et al., 2020) studies supporting the onset of plate tectonics during the Meso and/or Neoarchean, alongside numerical modeling explorations and reconstructions suggesting > 3.2 Ga operation of hot stagnant-lid tectonics (Johnson et al., 2017; Moore & Webb, 2013). As such, it can be argued that the scientific community now approaches a consensus concerning when plate tectonics initiated, which would allow a stronger focus on addressing how and why this process occurred.

However, the Eoarchean (ca. 3.8–3.6 Ga) Isua supracrustal belt of southwest Greenland (Figure 1) stands out as a counterexample versus proposed ≤ 3.2 Ga emergence of plate tectonics. The belt and its adjacent metatonalite bodies represent one of Earth's largest and best-preserved Eoarchean granitoid-greenstone terrane (e.g., Nutman & Friend, 2009). Such terranes have been diversely interpreted to record plate tectonic

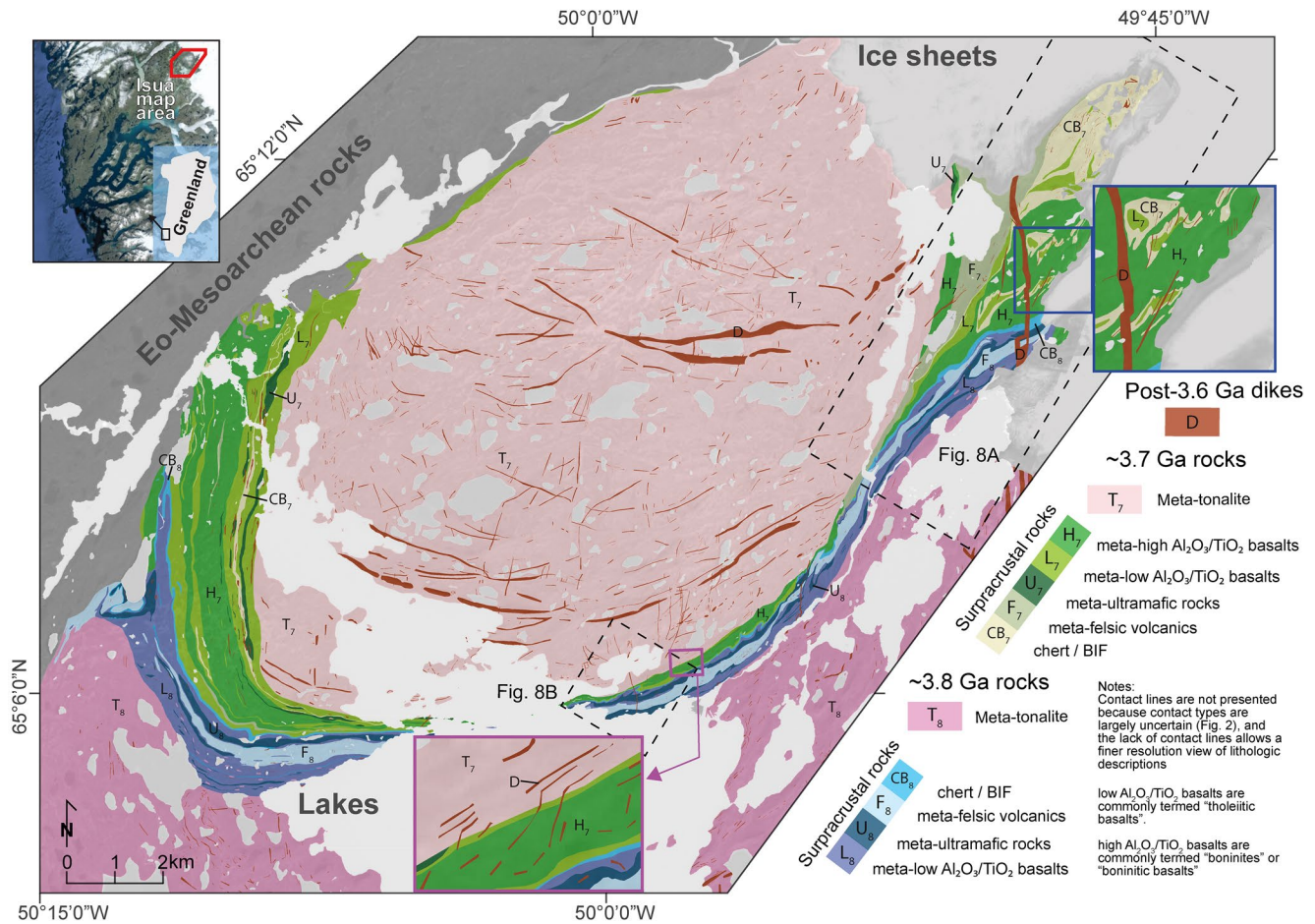


Figure 1. Map showing key geology of the Isua supracrustal belt (modified from Nutman and Friend [2009]). Insets show ca. 3.5–3.2 Ga dikes cross-cutting the pre-3.5 Ga contacts and structures. In the right inset, deformed rocks show bullseye map patterns of km-scale sheath folds (a la Alsop & Holdsworth, 1999). The dikes in the bottom inset are thought to be deformed in Neoproterozoic time (Nutman et al., 2004; White et al., 2000), but they cut the pre-3.5 Ga contacts at high angles. Therefore, this late deformation is thought to be weakly expressed in this area. This map does not show the ca. 3.66 Ga Inaluk dike and ca. 3.66–3.61 Ga granite and pegmatite sheets because these occur in minor volumes. Their locations are presented in the Figure S2 (for granite and pegmatite sheets) or in the original map in Nutman and Friend (2009). The Inaluk dikes intruded both ca. 3.7 and ca. 3.8 Ga tonalites whereas granite and pegmatite sheets intruded ca. 3.7–3.8 Ga tonalites and supracrustal rocks (Crowley, 2003; Crowley et al., 2002; Nutman & Friend, 2009). Abbreviation: BIF, banded iron formation.

and/or stagnant-lid tectonic processes (e.g., Van Kranendonk, 2010; Van Kranendonk et al., 2007). In the case of the Isua supracrustal belt, nearly every site-specific study has concluded that it preserves a plate tectonic terrane collision (e.g., Friend & Nutman, 2011; Hanmer & Greene, 2002; Komiya et al., 1999; Nutman et al., 2020; Nutman & Friend, 2009; Polat & Hofmann, 2003). Only recently has an alternative tectonic model involving heat-pipe cooling been proposed (Webb et al., 2020). If terrane collision did occur, and does record plate tectonics, then the emerging consensus of a 3.2–2.5 Ga onset of plate tectonics would need to be abandoned. Further examination of Isua’s record and its implications is therefore warranted.

A classical approach to testing regional tectonic evolution models is determining the pressure-temperature-time-deformation (P-T-t-d) history recorded across the different rock units and structural domains of a system. For the Isua supracrustal belt, questions of P-T-t-d evolution indeed remain, which could permit model testing. Some plate tectonic models predict metamorphic gradients, which the belt may or may not contain (e.g., Arai et al., 2015; Nutman et al., 2020; Webb et al., 2020). Likewise, complex sequential deformation patterns have been predicted in plate tectonic models (e.g., Nutman et al., 2013b), but strain records have been only sparsely investigated across the belt. For example, published shear sense information has been limited to few localities, including the western edge of the Isua supracrustal belt (Hanmer & Greene, 2002; Hanmer et al., 2002), one location on the boundary of the belt and north metatonalite,

one location on the boundary of the belt and south metatonalite (Komiya et al., 1999), and 15 field-based shear senses concentrated in the central northeast portion of the belt (Webb et al., 2020). Therefore, the deformation style and its relationships to local magmatic and metamorphic events are poorly constrained. One consequence is that the two main plate tectonic interpretations involve opposing subduction directions (cf., Komiya et al., 1999; Nutman & Friend, 2009). As such, the work presented here seeks to improve our understanding of the nature and sequence of deformation across the belt, and a complementary study (Ramírez-Salazar et al., 2021) seeks to improve our understanding of the belt's metamorphic evolution.

In this study, we conduct petrographic and quantitative crystallographic orientation analysis using electron backscatter diffraction (EBSD) analyses on thirty-three quartz-bearing samples from across the eastern half of the Isua supracrustal belt (Table 1) to examine their deformation fabrics (Figure 1; Tables 1 and 2). On the bases of field-based structural measurements and oriented sampling, EBSD can determine the crystallographic preferred orientations (CPOs) of quartz grains to explore strain histories, including deformation temperature (Kruhl, 1998; Stipp et al., 2002), strain magnitude (Heilbronner & Tullis, 2006), kinematic vorticity (Law, 1990; Law et al., 2004), and/or shear sense (Law, 1990; Schmid & Casey, 1986; Zibra et al., 2020). With such information, we test proposed tectonic models for the Eoarchean Isua supracrustal belt (Figure 2).

2. Geological Background

2.1. Regional Geology

The Eoarchean Isua supracrustal belt is a ~35 km long, ~1–3 km wide folded terrane located in southwest Greenland near the edge of the glacial ice sheet (Figure 1) (e.g., James, 1976; Keto & Kurki, 1967; Komiya et al., 1999; Nutman & Bennett, 2019; Webb et al., 2020). Zircon U-Pb ages show that the belt comprises two domains with an age difference of ca. 100 Myr: the ca. 3.7 Ga supracrustal belt to the north and the ca. 3.8 Ga supracrustal belt to the south (e.g., Crowley, 2003; Crowley et al., 2002; Nutman et al., 2002). These domains are separated by a nearly continuously exposed chert/banded iron formation (BIF) sedimentary unit along the central length of the belt. This unit has a unique detrital zircon age population with the youngest age peak of 3.75 Ga, and it has been termed the “dividing sedimentary unit” (Nutman & Friend, 2009; Nutman et al., 2009). To the north and south, the Isua supracrustal belt is in contact with ca. 3.7 Ga or ca. 3.8 Ga metatonalite bodies, respectively (Nutman & Friend, 2009). The belt and metatonalites are intruded by the following plutonic suites: (1) ca. 3.66–3.57 Ga granite and pegmatite (Figure S2) (Crowley, 2003; Crowley et al., 2002; Nutman et al., 1997, 2007), (2) ca. 3.5–3.2 Ga noritic to doleritic Ameralik dikes (Nutman et al., 2004), and (3) ca 2.2 Ga norite dikes (Nutman et al., 2002). The metatonalites are also intruded by ca. 3.66 Ga meladioritic to tonalitic Inaluk dikes (Crowley et al., 2002; Nutman & Bridgwater, 1986).

Supracrustal rocks of the belt are predominantly metamorphosed basalts, felsic volcanic rocks, chert, and BIF, with minor ultramafic rocks and clastic sedimentary rocks (Figure 1) (e.g., Appel et al., 1998; Fedo, 2000; Nutman et al., 2020; Webb et al., 2020). The supracrustal rocks were originally deposited in a marine environment, evidenced by chemical signatures of seawater alteration (e.g., Nutman et al., 2010; Polat & Hofmann, 2003), the presence of basalt pillows (Appel et al., 1998; Komiya et al., 1999; Nutman et al., 2007), and potential stromatolite (Nutman et al., 2016, 2019) (cf., Allwood et al., 2018; Zawaski et al., 2020). Basalts show two chemical associations: one with low $\text{Al}_2\text{O}_3/\text{TiO}_2$ of ~10, featuring negative Nb-Ta anomalies and flat to slightly downward fractionation trends from left to right in the primitive-mantle normalized trace element diagrams; the other with high $\text{Al}_2\text{O}_3/\text{TiO}_2$ of ~53–89, showing negative Nb-Ta anomalies and slightly upward fractionation trends from left to right in the primitive-mantle normalized rare earth element diagrams (e.g., Polat & Hofmann, 2003; Szilas et al., 2015). Based on these geochemical features, the low $\text{Al}_2\text{O}_3/\text{TiO}_2$ basalts are commonly described as “tholeiitic basalts” (e.g., Nutman & Friend, 2009; Polat & Hofmann, 2003) that are generally interpreted to represent melts of a moderately depleted mantle source with an addition of crustal components in the source and/or via magmatic assimilation (e.g., Polat & Hofmann, 2003; Smithies et al., 2007), or melts of preexisting high-MgO (>18 wt.%) crust (Johnson et al., 2014). The high $\text{Al}_2\text{O}_3/\text{TiO}_2$ basalts are commonly termed “boninites” or “boninitic basalts” (e.g., Nutman & Friend, 2009; Polat & Hofmann, 2003) that were mostly interpreted as melts of a highly depleted mantle source with some contamination of crustal-derived materials (e.g., Pearce & Reagan, 2019; Polat & Hofmann, 2003). Tonalites show strong rare-earth-element fractionation and Nb-Ta-Ti depletion,

Table 1
Summary of Petrographic Data

Sample ID		Lithology	Mineral assemblage ^a	Sample locations relative to proposed shear zones (1A, 1B, 2-5) or proposed suture zones (H, L) ^a	Mineral mode (%) ^b								
"JZ17" samples	Age (Ga)				Qtz	Bio	Mus	Chl	Amphi	Fe-oxides	Grt	Fsp	Others
714-4	3.7	Metafelsic volcanics	Qtz+bio+mus+kfs+plg+ilm+car	H	20	10	5			<1		65	<1
714-5A	3.7	Garnet-biotite amphibolite	Qtz+bio+grt (pre or syn & post)+hbl+plg++ilm+chl (retro)+car+apa	2	40	20		5	15	<1	10	5	5
715-5A	3.7	Chert/BIF	Qtz+Fe-amphi+mgt	L	60				40	<1			
715-5C	3.7	Carbonated felsic rock	Qtz+bio+mus+kfs+car	5	40	10	20					10	20
715-5F	3.7	Garnet-biotite amphibolite	Qtz+bio+grt (syn & post)+chl (retro)+car±amphi	5	25	60		5	<1		15		<5
715-7 (bqtz) ^c	3.75	Chert/BIF	Qtz+Fe-amphi+mgt	1B	95				<5	<1			
715-7 (sqtz)	3.75	Chert/BIF	Qtz+Fe-amphi+mgt	1B	83				15	2			
715-9	3.8	Garnet-biotite amphibolite	Qtz+bio+grt (syn)+plg+amphi+ilm+car+rut+epi (retro)	H	40	30	2	<1	2	2	1	15	7
717-2A	3.8	Metatonalite	Qtz+bio+ilm+epi+tnn+plg	H	25	20				<1		30	15
717-4	3.8	Chert/BIF	Qtz+Fe-amphi+mgt	H	90				7	3			
717-5	3.8	Metafelsic volcanics	Qtz+bio+grt (syn) +plg+kfs+mus	H	40	20	5				1	30	<5
717-7	3.8	Metafelsic volcanics	Qtz+bio+plg+kfs+mus+car	H	30	20	10					25	15
718-1	3.7	Garnet-biotite amphibolite	Qtz+bio+amphi+grt (post) +plg+epi	3	20	15			50		<1	5	10
720-4	3.7	Chert/BIF	Qtz+Fe-amphi+mgt±chl	L	70			<1	20	10			
721-1A	3.7	Chert/BIF	Qtz+Fe-amphi+mgt±chl (retro)+car	L	75			<1	10	10			5
721-2A	3.7	Chert/BIF	Qtz+Fe-amphi+mgt±chl	L	70				5	25			<1
725-2C	3.7	Metafelsic volcanics	Qtz+bio+grt (syn)+plg+rut	H	25	20					3	50	2
725-4B	3.7	Garnet-biotite amphibolite	Qtz+bio+hbl+grt (syn)	H	20	20			10		50		
725-5B	3.8	Metafelsic volcanics	Qtz+bio+plg+car+kfs	H	20	15	10					45	10
726-1B	3.7	Metatonalite	Qtz+mus+plg+epi	H	40		10					50	
726-5	3.7	BIF	Qtz+mgt+grt (post)+epi+cpx±hbl	H	50				<1	15	15		20
726-6A	3.75	Metafelsic volcanics	Qtz+bio+ilm+grt (syn)+plg+mus	1B	30	20	5			<1	5	40	

Table 1*Continued*

Sample ID		Lithology	Mineral assemblage ^a	Sample locations relative to proposed shear zones (1A, 1B, 2–5) or proposed subterrane (H, L) ^a	Mineral mode (%) ^b								
“JZ17” samples	Age (Ga)				Qtz	Bio	Mus	Chl	Amphi	Fe-oxides	Grt	Fsp	Others
726-8	3.8	Metafelsic volcanics	Qtz+bio+ilm+mus+car±amphi	H	30	20	10		<1	<1	30	10	
729-1A	3.7	Metafelsic volcanics	Qtz+bio+ilm+grt (pre or syn)+mus+rut+chl (retro)	1A	50	<1	5	5		3	5	30	2
729-4	3.7	Chert/BIF	Qtz+Fe-amphi+mgt	L	90				10				<1
729-10	3.7	Quartz-bearing amphibolite	Qtz+hbl+bio±plg+car+chl (retro)	L	20	60			18			2	<1
730-2C	3.7	Chert/BIF	Qtz+Fe-amphi+mgt	1A	90				10	<1			
730-2F	3.75	Chert/BIF	Qtz+Fe-amphi+mgt	1B	80				20	<1			
801-1B	3.7	Amphibolite	Qtz+hbl+bio+plg+epi (retro)	4	50	15			10			5	20
801-4	3.7	Carbonated felsic rock	Qtz+bio+mus+epi+car+plg+kfs	L	50	25	10				5	3	7
801-6A	3.7	Chert/BIF	Qtz+Fe-amphi+mgt+chl	L	75			1	20	5			
801-8C	3.7	Metafelsic volcanics	Qtz+chl (retro)+plg+mus+rut+grt (pre or syn & post)+car±bio	2	30	<1	5	30		<1	10	25	
801-9A	3.7	Metafelsic volcanics	Qtz+bio+plg+grt (pre or syn)	H	10	10	10				<1	60	10
802-5	3.8	Metafelsic volcanics	Qtz+bio+mus+kfs±amphi	H	45	10	20		<1			20	5

Abbreviation: amphi, amphibole; bio, biotite; car, carbonate; chl, chlorite; cpx, clinopyroxene; epi, epidote; Fe-amphi, Fe-rich amphibole (e.g., grunerite & cummingtonite); Fsp, feldspar; grt, garnet; hbl, hornblend; kfs, K-feldspar; ilm, ilmenite; mgt, magnetite; mus, muscovite; plg, plagioclase; pre, pre-tectonic; post, post-tectonic; qtz, quartz; retro, retrograde; rut, rutile; syn, syn-tectonic; ttn, titanite.

^aThe locations of samples are in Figures 8a and 8b. Proposed shear zones are coded (Figures 8a and 8b) (e.g., Appel et al., 1998; Nutman & Friend, 2009) and showed if a sample is from a specific shear zone (1A and 1B are proposed terrane boundaries separating zones with different strain histories, 2–5 are proposed major shear zones inside these proposed subterrane). If a sample is not from a specific shear zone, the proposed subterrane it belongs to would be showed (L, a proposed subterrane with low strain; H, proposed subterrane with high strain). ^bMineral modes (%) are estimated from petrographic or SEM images. The absolute errors are up to 10%. ^cSample 715-7 is divided into two parts, one part (bqtz) with mostly >150 μm quartz grains, the other (sqtz) with mostly ~10–100 μm quartz grains (see Figure 7 for an illustration).

matching the modeling results of partial melting of metamorphosed hydrated supracrustal basalts (e.g., Nagel et al., 2012; Nutman et al., 2020). Granite and pegmatite are interpreted as crustal melt products of tonalites based on their (1) geochemistry, (2) zircon isotope characteristics, and (3) field relationships with tonalites (e.g., Crowley et al., 2002; Hiess et al., 2011; Nutman et al., 1996).

Ultramafic rocks occur in the Isua supracrustal belt and in the metatonalite, and have been variously altered to chlorite/talc schists or serpentinites (e.g., Dymek et al., 1988b). In few locations, some ultramafic lenses preserve characteristics of identifiable primary lithologies (dunite or harzburgite), specifically: ~10 km south of the belt, in the tonalite (Friend et al., 2002; van de Löcht et al., 2018, 2020) and near the eastern edge of the western Isua supracrustal belt, in the belt (Friend & Nutman, 2011; Nutman et al., 1996; Szilas et al., 2015)]. These ultramafic rocks show chemical associations with the Isua supracrustal basalts (Szilas et al., 2015; van de Löcht et al., 2020) or arguably with komatiite (Dymek et al., 1988b) (cf., Szilas et al., 2015). Some, but not all, geochemical characteristics of the least altered ultramafic rocks are similar to those of depleted mantle (Friend & Nutman, 2011; Friend et al., 2002; Szilas et al., 2015; van de Löcht et al., 2018). The least altered dunites in the belt show mineralogy of olivine + antigorite ± Ti-humite ± magnesite ± spinel (Friend & Nutman, 2011; Nutman et al., 2020), and the olivine crystals appear to have been deformed into B-type fabrics (Kaczmarek et al., 2016).

The Isua supracrustal belt has been reported to have experienced two main metamorphic events: (1) a lower to upper amphibolite facies metamorphic event before the ca. 3.5–3.2 Ga intrusion of Ameralik dikes (Nutman et al., 2004) and (2) an epidote amphibolite facies metamorphic event (<540°C and <0.5 GPa, Ramírez-Salazar et al., 2021) during Neoproterozoic time (e.g., Blichert-Toft & Frei, 2001; Nutman & Collerson, 1991; Nutman et al., 2013b; Rollinson, 2003). These two events can be differentiated by their associated petrological textures: the Neoproterozoic metamorphic event was static, as evidenced by static growth of garnet rims (e.g., Gauthiez-Putallaz et al., 2020), whereas the metamorphic minerals of the pre-3.5 Ga metamorphic event have been deformed and appear to preserve syn-tectonic textures (e.g., Nutman & Friend, 2009; Rollinson, 2002). Although it is widely agreed that there were at least two major metamorphic events, it remains unclear whether the pre-3.5 Ga syn-tectonic metamorphism was polyphase in nature (e.g., Nutman et al., 2013b; Gauthiez-Putallaz et al., 2020; Rollinson, 2002, 2003) or reflects a single prograde event (e.g., Arai et al., 2015; Ramírez-Salazar et al., 2021; Webb et al., 2020) that was overprinted by later retrogression and/or lower-grade static metamorphism events. The inferred temperature/pressure gradient(s) for this syn-tectonic metamorphism event is also controversial. Some authors propose diverse gradients ranging from <250°C/GPa to >1,000°C/GPa (Nutman et al., 2020) largely based on the mineral assemblages of metamorphosed dunites (Figure 10 of Nutman et al., 2020), partially melted amphibolitic enclaves in the north tonalite (Figure 7 of Nutman et al., 2013b), and other partially melted rocks located at ~150 km south of the Isua supracrustal belt (Nutman et al., 2020). In contrast, others suggest the observed mineral assemblage and metamorphic textures in rocks from the Isua supracrustal belt and tonalites could be viably interpreted as indicating semi-uniform temperature/pressure gradients across the belt (i.e., ~800°C–1,000°C/GPa, Ramírez-Salazar et al., 2021). The existence of a metamorphic gradient across the belt has also been questioned (Arai et al., 2015; Nutman et al., 2020; Webb et al., 2020). Several metasomatic events have been proposed to occur at ca. 3.74 Ga (Frei & Rosing, 2001), ca. 3.63 Ga (Frei et al., 1999) and ca. 2.85 Ga (Frei et al., 1999). However, temporal constraints of the earliest proposed metasomatic event may be invalid since the ca. 3.74 Ga age is from Pb-Pb step-leaching dating of metasomatic minerals in posttectonic veinlets, which conflicts with ca. 3.7–3.6 Ga deformation and amphibolite-metamorphism (see below) that would have overprinted any early metasomatic veinlets.

Most of the Ameralik dikes (ca. 3.5–3.2 Ga) are undeformed and cross-cut lithologic contacts, folds and foliations preserved in the Isua supracrustal belt and adjacent metatonalite bodies (Figure 1) (e.g., Nutman et al., 2004, 2007; White et al., 2000). However, some Ameralik dikes exposed in the north metatonalite near its south margin, the supracrustal belt, and the south metatonalite preserve lineation and foliation fabrics that are concordant to those of host rocks (e.g., Figure 5 in White et al., 2000). Nevertheless, some deformed dikes (e.g., the relatively larger dikes in the bottom inset of Figure 1, and area B of Figure 1 of White et al., 2000) cross-cut the Isua supracrustal belt at high angles. One interpretation is that some of the Ameralik dikes were deformed during Meso or Neoproterozoic time. We note that the nature and specific

effect of potential Meso or Neoproterozoic deformation within the Isua supracrustal belt remain little explored (e.g., Nutman et al., 2002). Consequently, here we follow previous observations that such deformation was weakly expressed in the already strongly deformed Isua supracrustal belt and adjacent metatonalite (e.g., Nutman et al., 2002, 2015a, 2020). Some ca. 3.66–3.61 Ga granite and pegmatite sheets show pre and/or syn-tectonic textures (e.g., Crowley et al., 2002; Nutman et al., 2002, 2013b), including a ca. 3.66 Ga deformed granite sheet that has been interpreted as a syn-tectonic intrusion within the supracrustal belt (Nutman et al., 2009) (Figure S2). Dated post-tectonic granite bodies are limited to two outcrops. One is a ca. 3.61 Ga granite inside the south metatonalite, where the granite is only slightly discordant to the local gneissic layering (Figure 9 of Nutman et al., 2002). The other is a ca. 3.57 Ga granodiorite within the belt (Figure S2) (Nutman et al., 1997). Therefore, the area presented in Figure 1, including the Isua supracrustal belt, is generally interpreted as having well-preserved pre-3.5 Ga (potentially pre-3.61 Ga) structural patterns (e.g., Crowley et al., 2002; Nutman et al., 2002, 2020).

The pre-3.5 Ga structures of the Isua supracrustal belt and adjacent metatonalite include (1) well-developed, steeply dipping foliation fabrics that are parallel to the belt margins and collectively define a fold axis parallel to the regional mineral stretching lineation, which parallelism is a characteristic of a-type folds; (2) penetrative mineral lineation fabrics plunging steeply to the southeast (Figure S1) (e.g., Bridgwater et al., 1974; Crowley, 2003; Crowley et al., 2002; Hanmer & Greene, 2002; James, 1976; Komiya et al., 1999; Nutman & Friend, 2009; Nutman et al., 2002; Webb et al., 2020); and (3) folds that have been interpreted as 0.1 m to km-scale sheath and curtain folds with fold axes subparallel to stretching lineations (e.g., Hanmer & Greene, 2002; Webb et al., 2020), including km-scale sheath folds that have bullseye map patterns (Figures 1 and S1) (also see Alsop & Holdsworth, 2012 for visualization of sheath folds and associated eye patterns). Accordingly, rocks preserved in the belt mostly appear as L-S tectonites (e.g., James, 1976; Webb et al., 2020), with minor occurrences of L-tectonites (Figure S1f; also see Figure DR2 of Webb et al. [2020]). These structures appear to have developed via intensive shearing and stretching, with up to 90% thinning (Fedo, 2000; Furnes et al., 2007; Webb et al., 2020). However, primary structures such as pillow basalts are locally recognizable. Some authors interpret this as local preservation in zones of relatively low strain (e.g., Appel et al., 1998; Nutman et al., 2007, 2016). Others interpret quasiuniform high strain across the belt, and argue the local visibility of primary structures is dependent on outcrop surface orientation and weathering characteristics (Webb et al., 2020).

Some workers have posited that in the Isua supracrustal belt there are multiple ~10-m-scale, pre-3.5 Ga shear zones (e.g., Hanmer & Greene, 2002; Komiya et al., 1999; Nutman & Friend, 2009; Nutman et al., 2013a, 2013b, 2020). These proposed structures are interpreted to juxtapose major features such as the 3.7 and 3.8 Ga parts of the supracrustal belt, as well as minor features such as two rock units with (a) interpreted age differences as small as a few million years and/or (b) interpreted minor metamorphic grade contrasts (see *tectonic models* for examples of proposed shear zones). In contrast, a recent work (Webb et al., 2020) claims that discrete shear zones do not exist and are not required to generate the geology of the Isua supracrustal belt, as the belt is interpreted to preserve quasi-uniformly distributed strain and similarly quasi-uniform pre-3.5 Ga metamorphic conditions. Furthermore, the existing geochronological constraints for the supracrustal rocks are sparsely distributed and too weak to confidently resolve Eoarchean age distinctions on the order of ≤ 30 Myr (Webb et al., 2020).

Finally, the northmost exposure of the northern metatonalite exhibits gently inclined stretching lineations that plunge to the north. This part of the metatonalite has been interpreted to preserve structural fabrics that are older than the pre-3.5 Ga structures observed in the Isua supracrustal belt (e.g., Crowley et al., 2002). Future investigations may reveal whether this area preserves an earlier fabric and/or different deformation styles developed during the same event(s) that has deformed the Isua supracrustal belt.

2.2. Tectonic Models

Several tectonic models have been invoked to explain the geology of the Isua supracrustal belt (e.g., James, 1976; Keto & Kurki, 1967; Komiya et al., 1999; Nutman et al., 2020). In our description of these models, we use tectonic model terminology (e.g., “plate tectonics,” “heat-pipe tectonics,” etc.) following the classification scheme of Lenardic (2018).

The earliest proposed model for the structural development of the Eoarchean Isua supracrustal belt involves an early quasi-homogenous deformation event related to uplift of the north metatonalite. The deformation is defined by series of isoclinal folds with axial traces that parallel the strike of the belt, which were deformed by a subsequent east-west-oriented shortening event that generated the belt's current shape (all cardinal directions are considered in current coordinates) (Keto & Kurki, 1967). The predictions for this earliest proposed model are similar to those of a later model in which the Eoarchean Isua supracrustal belt was deformed via top-to-southeast shearing during uplift of the northern tonalite, followed by top-east-northeast horizontal shearing and the development of (1) a km-scale fold with a north-northeast-trending axial trace that folded the belt into its current geometry; and (2) ~1–10 m-scale minor folds (Z-, S- and M-folds) that form the limbs of the km-scale fold (Figure 2a) (James, 1976).

More recently, geochemical, petrological and structural patterns of the Isua metatonalite and supracrustal rocks have been interpreted as indicating early subduction processes in plate tectonic settings (Figures 2b and 2c) (e.g., Arai et al., 2015; Hoffmann et al., 2014; Komiya et al., 1999; Nagel et al., 2012; Nutman et al., 2013a, 2015a, 2020; Polat & Hofmann, 2003; Polat et al., 2011). Two plate tectonic models have been proposed (Figures 2b and 2c) (e.g., Komiya et al., 1999; Nutman & Friend, 2009), which are described below.

In one plate tectonic model, the Isua supracrustal belt represents an accretionary prism with different panels of rocks separated by hundreds of subparallel, north-directed discrete thrusts that developed during southward subduction (e.g., Arai et al., 2015; Komiya et al., 1999) (Figure 2b). Subsequent exhumation of the metamorphosed accretionary prism via wedge extrusion is thought to have been accommodated by top-to-south and top-to-north south-dipping fault systems at the respective southern and northern margins of the belt (Arai et al., 2015). Proposed final emplacement of the variably metamorphosed wedge would have created a prograde metamorphic gradient across the present-day northeastern area of the belt: from greenschist facies at the northeast end of the belt to upper amphibolite facies to the southwest across a 4 km distance. Within the 4 km-long area, four zones of contrasting metamorphic facies are proposed to be separated by three discrete northwest-striking thrust faults with a top-to-the-southwest transport direction (Arai et al., 2015). The remainder of the belt farther west records upper amphibolite facies conditions.

The second plate tectonic model describes the Isua supracrustal belt as preserving two arc complexes that collided along a ca. 3.7–3.66 Ga, northward-dipping suture zone. During the proposed collision, the “dividing sedimentary unit” served as the top-to-south suture between the arc complexes (Figure 2c) (e.g., Nutman & Friend, 2009; Nutman et al., 2015a). Several collisional environments have been applied to explain the interpreted >3.66 Ga protolith origins and metamorphic facies of the supracrustal rocks and tonalites (e.g., Nutman et al., 2020). First, the formation of the metatonalite protoliths, two types of basalt, and the depleted mantle peridotites bearing B-type olivine fabrics and Ti-humite has been associated with slab fluxing and partial melting in low-temperature, high to ultrahigh-pressure environments (including subducting slab and mantle wedge settings) (e.g., Nagel et al., 2012; Nutman et al., 2020; Polat & Hofmann, 2003). Second, the intrusion of tonalites in the crust has been proposed to have caused interpreted high-temperature, low-pressure metamorphism (Friend & Nutman, 2005; Nutman et al., 2020). Third, interpreted amphibolite-granulite metamorphism within the Isua supracrustal belt and tonalite was related to crustal imbrication during the proposed collision (e.g., Nutman et al., 2013b, 2020). This plate tectonic model also involves shortening within each arc-complex to explain the presence of folds and the juxtaposition of rocks and/or hypothesized subterrane via 10-m-scale, top-to-south shear zones (e.g., Appel et al., 1998; Hanmer & Greene, 2002; Nutman & Friend, 2009; Nutman et al., 2007, 2013a, 2020). Several features have been interpreted to reflect this shortening strain. One example is a postulated subterrane in the northeastern portion of the belt that preserves lower strain (and hence some recognizable primary structures) and is separated by faults from other subterrane preserving seemingly higher strain (e.g., Appel et al., 1998; Nutman et al., 2016). In addition, the bullseye map patterns (Figures 1 and S1b) have been proposed to represent folding of thrust-intercalated rock panels with older-over-younger age distinctions of ~26 Myr (Nutman et al., 2016, 2020). The proposed collision is thought to be followed by ca. 3.66–3.61 Ga orogenic collapse and core complex formation via top-to-south extensional faulting (Nutman et al., 2013b). Several features have been interpreted to reflect the proposed core complex formation and associated extensional deformation at amphibolite to greenschist facies conditions, including a double-plunging anticline within the north

Table 2
Summary of Structural Data

Sample ID	Foliation		Lineation			Sample locations relative to proposed shear zones (1A, 1B, 2–5) or proposed subterrane (H, L) ^a	Quartz CPO pattern		Misorientation axes of quartz 2°–10° boundaries	Texture indexes ^b				
	“JZ17” samples	Age (Ga)	Dip direction	Dip	Trend		Plunge	Shear sense		Dominant slip system	Dominant slip system	J <c>	M Index	Point
<i>Samples featuring significant quartz aggregates/bands and ≥30% EBSD quartz modes (Figure S4)</i>														
714-4	3.7	117	60	161	51	H	Top-to-NW	Mixed	Prism <a>	1.38	0.02	0.05	0.13	0.82
714-5A	3.7	125	72	155	63	2	Coaxial	Mixed	Prism <a>	1.39	0.01	0.12	0.05	0.83
<u>715-5A</u>	3.7	080	57	120	53	L	Top-to-SE	Prism <a>	Prism <a>	2.95	0.03	0.10	0.16	0.74
715-5C	3.7	090	67	148	55	5	Coaxial	Mixed	Prism <a>	1.48	0.01	0.07	0.08	0.85
715-5F	3.7	090	67	148	55	5	Coaxial	Prism <a>	Prism <a>	1.40	0.01	0.03	0.12	0.85
<u>715-7 (bqtz)^c</u>	3.75	<u>150^d</u>	<u>85</u>	<u>150</u>	<u>72</u>	1B	Top-to-NW	Prism <a>	Prism <a>	2.95	0.09	0.32	0.13	0.55
715-7 (sqtz)	3.75	<u>150</u>	<u>85</u>	<u>150</u>	<u>72</u>	1B	Top-to-NW	Prism <c>	Prism <a>	1.56	0.02	0.15	0.10	0.75
715-9	3.8	134	78	120	70	H	Top-to-SE	Prism <a>	Prism <a>	1.20	0.01	0.08	0.03	0.89
<u>717-4</u>	3.8	145	71	095	67	H	Top-to-NW	Prism <a>	Prism <a>	3.23	0.18	0.46	0.14	0.40
717-7	3.8	130	50	145	54	H	Top-to-SE	Mixed	Prism <a>	1.40	0.02	0.05	0.24	0.71
718-1	3.7	082	58	147	52	3	Top-to-SE	Prism <c>	Prism <a>	1.24	0.01	0.03	0.05	0.92
720-4	3.7	054	90	122	88	L	Top-to-NW	Prism <c>	Prism <a>	1.27	0.01	0.08	0.01	0.91
<u>721-1A</u>	3.7	064	73	067	50	L	Top-to-SW	Basal <a>	Prism <a>	1.52	0.03	0.16	0.11	0.73
<u>721-2A</u>	3.7	068	79	152	50	L	Top-to-NW	Basal <a>	Prism <a>	1.56	0.03	0.03	0.38	0.59
725-2C	3.7	172	60	147	72	H	Top-to-SE	Prism <a>	Prism <a>	2.04	0.07	0.14	0.44	0.41
<u>725-4B</u>	3.7	183	80	200	78	H	Top-to-NW	Prism <a>	Prism <a>	2.86	0.09	0.28	0.33	0.39
<u>726-1B</u>	3.7	155	50	171	48	H	Top-to-NW	Prism <c>	Prism <a>	2.74	0.03	0.23	0.04	0.73
726-5	3.7	155	74	220	60	H	Coaxial	Basal <a>	Prism <a>	2.00	0.05	0.24	0.11	0.65
726-8	3.8	140	65	125	63	H	Top-to-SE	Mixed	Prism <a>	1.21	0.01	0.03	0.18	0.80
729-1A	3.7	057	47	054	80	1A	Top-to-NE	Prism <a>	Prism <a>	1.35	0.01	0.07	0.12	0.81
729-4	3.7	128	70	186	80	L	Top-to-N	Basal <a>	Prism <a>	1.79	0.03	0.17	0.15	0.68
<u>730-2C</u>	3.7	111	73	100	71	1A	Top-to-NW	Mixed	Prism <a>	3.26	0.13	0.17	0.63	0.20

Table 2
Continued

Sample ID	Foliation		Lineation			Sample locations relative to proposed shear zones (1A, 1B, 2–5) or proposed subterrane (H, L) ^a	Quartz CPO pattern		Misorientation axes of quartz 2°–10° boundaries	Texture indexes ^b					
	Age (Ga)	Dip direction	Dip	Trend	Plunge		Shear sense	Dominant slip system		Dominant slip system	J <c>	M Index	Point	Girdle	Random
“JZ17” samples															
730-2F	3.75	111	73	100	71	1B	Top-to-NW	Mixed	Prism <a>	1.90	0.02	0.09	0.14	0.77	
801-1B	3.7	115	65	114	65	4	Top-to-SE	Prism <c>	Mixed <a>	1.56	0.01	0.07	0.09	0.84	
802-5	3.8	139	71	160	71	H	Top-to-NW	Prism <c>	Prism <a>	1.26	0.01	0.10	0.03	0.87	
<i>Samples featuring isolated quartz grains and less than 20% EBSD quartz modes (Figure S4)</i>															
717-2A	3.8	148	72	166	65	H	Top-to-SE	Mixed	Prism <c>	1.43	0.01	0.04	0.11	0.85	
717-5	3.8	124	57	118	55	H	Coaxial	Prism <a>	Prism <a>	1.73	0.03	0.12	0.21	0.67	
801-4	3.7	106	50	145	59	L	Coaxial	Prism <c>	Prism <c>	1.80	0.03	0.12	0.22	0.66	
801-8C	3.7	093	51	119	70	2	Top-to-SE	Prism <a>	Mixed <a>	1.72	0.02	0.09	0.16	0.75	
801-9A	3.7	085	56	137	47	H	Top-to-NW	Prism <a>	Prism <a>	1.39	0.02	0.08	0.19	0.73	
<i>Samples whose quartz grains cannot be reconstructed due to poor raw data quality (Figure S4)</i>															
725-5B	3.8	177	75	201	62	H	Top-to-SW	Prism <c>	Mixed <a>+<c>	1.57	0.02	0.09	0.23	0.68	
726-6A	3.75	161	75	186	74	1B	Top-to-S	Prism <a>	Mixed <a>	1.59	0.03	0.11	0.21	0.68	
729-10	3.7	075	76	130	76	L	Top-to-SE	Prism <c>	Prism <a>	2.06	0.05	0.19	0.21	0.59	
801-6A	3.7	166	80	102	80	L	Coaxial	Prism <c>	Basal <a>	2.00	0.06	0.20	0.24	0.56	

^aThe locations of samples are in Figures 8a and 8b. Proposed shear zones are coded (Figures 8a and 8b) (e.g., Appel et al., 1998; Nutman & Friend, 2009) and showed if a sample is from a specific shear zone (1A and 1B are proposed terrane boundaries separating zones with different strain histories, 2–5 are proposed major shear zones inside these proposed subterrane). If a sample is not from a specific shear zone, the proposed subterrane it belongs to would be showed (L: a proposed subterrane with low strain; H: proposed subterrane with high strain). ^bTexture indexes indicate the CPO strength and styles (Bunge, 2013; Skemer et al., 2005; Ulrich & Mainprice, 2005). J <c> denotes J-index of quartz c-axis. ^cSample 715-7 is divided into two parts, one part (bqtz) with mostly >150 μm quartz grains, the other (sqtz) with mostly ~10–100 μm quartz grains (see Figure 7 for an illustration). ^dUnderlined measurements are estimated (see Methods). Samples with underlined IDs are those who show high (>80%) quartz modes in the EBSD scanned areas (Figure S4).

metatonalite (Nutman, 1986), granite and pegmatite intrusions, sigmoidal structures, and rock textures interpreted to record cataclasis (Nutman et al., 2013b).

Recent and current research focusing on field evidence and reappraisal of published petrology, structural, and geochronology data (Webb et al., 2020), metamorphism (Ramírez-Salazar et al., 2021), and the protolith(s) of ultramafic rocks (Szilas et al., 2015) posit that the arguments in support of multiphase crustal imbrication, orogenic collapse, wedge extrusion and development of a metamorphic gradient, and the petrogenesis of the basalts, peridotites, and tonalites in subduction settings are overinterpretations and do not necessarily require plate tectonic settings. First, the generation of the two types of basalts and the tonalite protoliths is possible in nonplate tectonic settings that feature extensive melting and recycling of deeply buried hydrous basalts (see next paragraph, also [Johnson et al., 2017; Pearce & Reagan, 2019; Smithies et al., 2007]). Second, B-type olivine fabrics, depleted mantle-like geochemistry, and the coexistence of

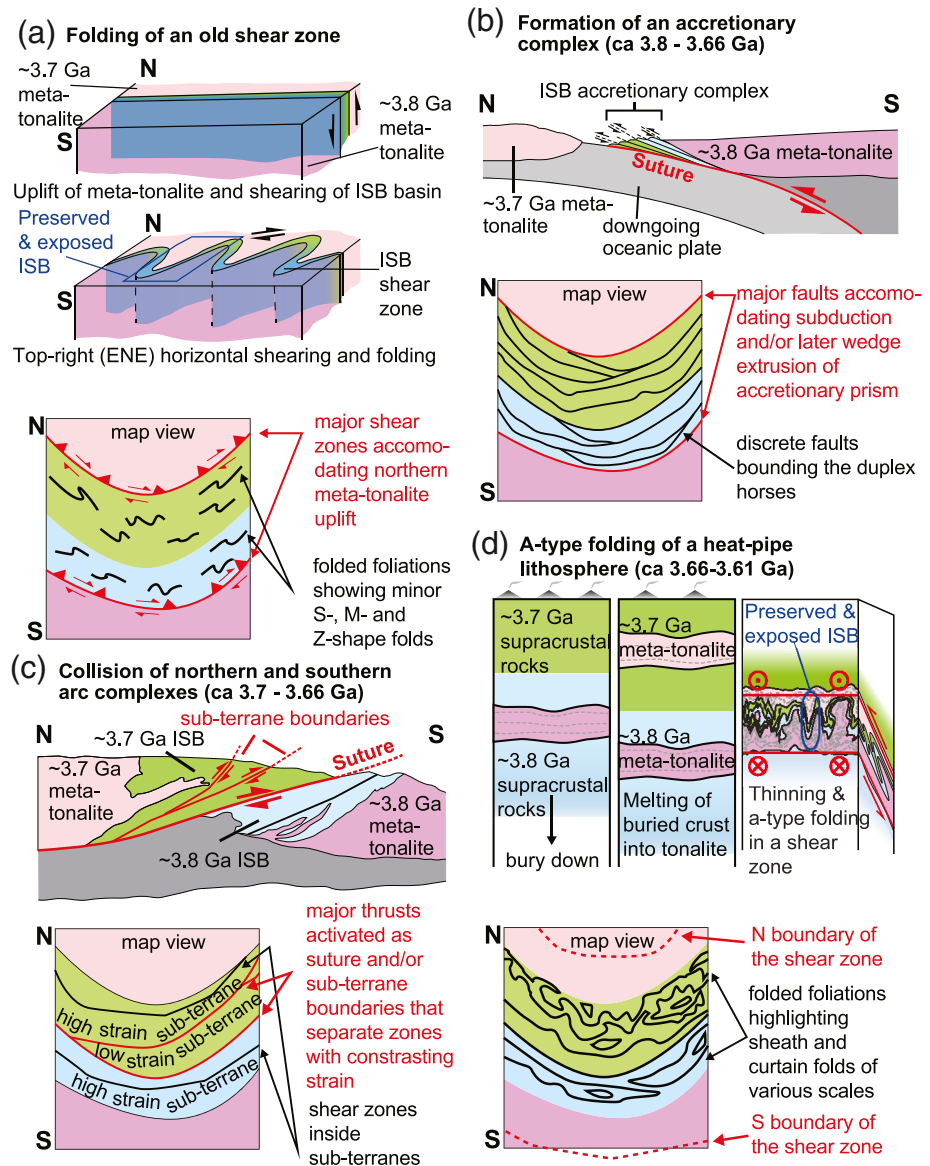


Figure 2. Proposed tectonic models for the Eoarchean Isua supracrustal belt. (a) Uplift of the 3.7 Ga metatonalite and shearing of the Isua supracrustal belt via two major shear zones in an unspecified tectonic setting, followed by horizontal shearing and folding (modified from James [1976]). (b) Development of an accretionary prism (modified from Komiya et al. (1999)) during southward subduction (in current coordinates, same for below). This model predicts duplex development via discrete, top-to-north shear zones. Later wedge extrusion of the metamorphosed accretionary prism along two major faults was proposed by Arai et al. (2015). (c) Collision of two arc complexes during a northward subduction event [modified from Nutman and Friend (2009)]. This model predicts discrete top-to-south shear zones (faults) juxtaposing rocks of contrasting ages, metamorphic facies and/or strain. (d) A-type (sheath and curtain) folding of a heat-pipe lithosphere (modified from Webb et al. [2020]) during contraction in response to downward advection or a plate-breaking/subduction event.

Ti-humite and magnesite (Dymek et al., 1988a) may not be discriminating features of subduction zone conditions, as they may be consistent with amphibolite-grade crustal cumulates (Dymek et al., 1988a; Szilas et al., 2015; Yao et al., 2019). Therefore, existing and new petrological information of the Isua supracrustal rocks can be interpreted as preserving quasi-uniform, pre-3.5 Ga amphibolite metamorphism with increasing metasomatic effects toward the northeastern part of the supracrustal belt (Ramírez-Salazar et al., 2021; Webb et al., 2020). Furthermore, field observations show that the belt can be interpreted as preserving quasi-uniformly distributed strain without major fault structures (Webb et al., 2020). Finally, previously

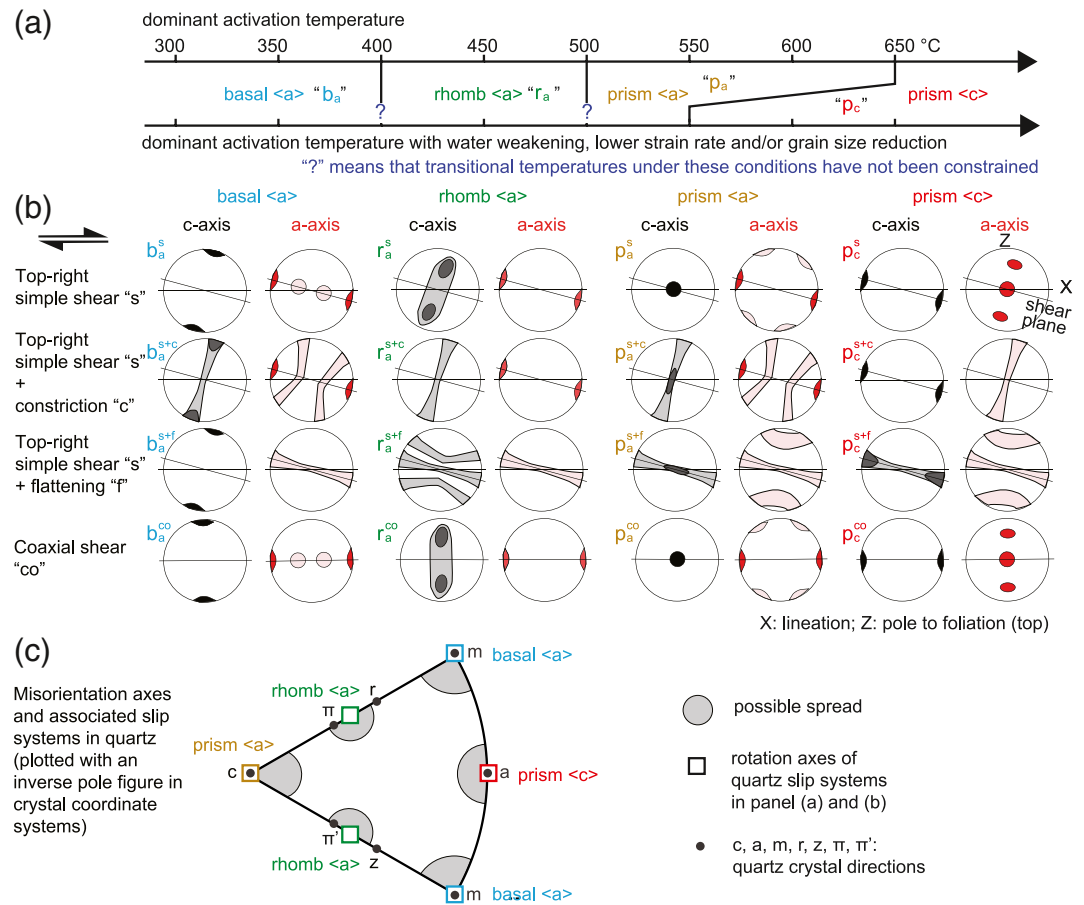


Figure 3. Examples of quartz CPO pole figure patterns and inverse pole figure patterns of misorientation axes, and their associated quartz slip systems and/or deformation conditions. (a) Dominant quartz slip systems as a function of deformation temperatures, constrained by naturally deformed quartz veins (Stipp et al., 2002). However, several factors were found to allow dominant <a> slip to dominant <c> slip transition to occur at lower temperatures (e.g., Hippertt, 1994; Kilian et al., 2011; Okudaira et al., 1995; Tullis et al., 1973). (b) Representative c-axis and a-axis pole figure patterns (modified from Barth et al. [2010]) of top-right or coaxial shear. The asymmetry of CPO pole maximums relative to the reference frame (i.e., X and Z) can indicate the shear sense. Each quartz slip system or shear style has a shortened code-name presented here and in Figures 5–7 to better support reader interpretation of quartz CPO patterns. (c) Misorientation axes of low angle grain boundaries and their associated quartz slip systems, plotted with crystal coordinate systems (modified from Neumann [2000]).

proposed age distinctions among rocks of either 3.7 or 3.8 Ga age (e.g., Friend & Nutman, 2010; Nutman et al., 2020) cannot be confidently recognized with the resolution of existing geochronology data, so faults inferred on the basis of different interpreted ages represent nonunique interpretations (Webb et al., 2020).

In light of these uncertainties in plate tectonic interpretations, recent work interprets that the Isua supracrustal belt is a fragment of a heat-pipe lithosphere that was deformed during a ca. 3.66–3.61 Ga contractional deformation event (Figure 2d) (e.g., Webb et al., 2020). Heat-pipe tectonics features planetary cooling dominated by mafic volcanism, which creates a thick, cold, and strong lithosphere as surface volcanic rocks are progressively buried by continuing deposition of volcanic materials (Moore & Webb, 2013) (To clear up a common misconception, heat pipes themselves are not equivalent to plumes: plumes are thought to span the height of the mantle, whereas heat pipes are simply volcanic conduits through the lithosphere). In the application of this model, the Isua supracrustal belt is interpreted to represent deposition of ca. 3.8 Ga volcano-sedimentary rocks, followed by a similar ca. 3.7 Ga event. Each eruptive cycle buried preexisting volcanic material, thereby generating tonalitic melts of metamorphosed hydrous basalts and potentially

low $\text{Al}_2\text{O}_3/\text{TiO}_2$ basaltic melts of high-MgO (>18 wt.%) crust at depth. Recycling of hydrous supracrustal belt material (and their melt residues) could have produced similar characteristics compared to subduction, including enrichment of various depleted mantle components. Both low and high $\text{Al}_2\text{O}_3/\text{TiO}_2$ basaltic melts can be generated with such variously depleted mantle sources. The tonalitic melts rose to roughly similar crustal levels, becoming the protoliths of the ca. 3.8 Ga and ca. 3.7 Ga metatonalite bodies. A subsequent ca. 3.66–3.61 Ga tectono-metamorphic event is speculated to represent contraction in response to either radial subsidence of heat-pipe lithosphere (i.e., downwards advection of spherical lithosphere forces it into progressively smaller areas) (e.g., Bland & McKinnon, 2016), or a plate-breaking event that signifies the transition to a plate tectonic cooling regime (e.g., Beall et al., 2018). During this proposed event, the entire belt was sheared, thinned, and stretched under amphibolite facies conditions, whereby strain was distributed quasi-uniformly and 0.1-m to km-scale curtain and sheath folds developed across the belt. Sheath folds can preserve two opposing shear senses on opposing limbs (Alsop & Holdsworth, 2012; Webb et al., 2020). Finally, later metasomatism is proposed to be responsible for the apparent metamorphic gradient (e.g., Arai et al., 2015) at the northeasternmost portion of the supracrustal belt (Ramírez-Salazar et al., 2021; Webb et al., 2020).

Major differences among these proposed tectonic models include predictions of the shear senses and strain distribution across the Isua supracrustal belt. Plate tectonic models predict strain localization in 10 m-scale shear zones that preserve dominantly unidirectional shear senses in accordance with the subduction vergences, possibly with reversal of shear sense in few structurally high shear zones during late-stage exhumation. In contrast, the heat-pipe model predicts distributed strain with two opposing shear senses located along the limbs of 0.1-m to km-scale sheath folds, such that strain magnitude is relatively uniform and opposing shear sense indicators are quasi-randomly distributed across the belt. In this study, the results of our thin-section and EBSD micro-tectonic analyses are compared with these predictions to test models.

3. Methods

For each sample collected in the field, foliation and lineation orientations were measured using a compass clinometer directly on the sample, or were estimated from measurements sighted at up to ~2.5 m away from the sample in cases of strongly magnetic outcrops (Table 2). Samples were collected from outcrops which show clear foliation and lineation to ensure preservation of significant plane strain components (which is necessary for some structural analyses used in this work). We selected 33 samples across the eastern Isua supracrustal belt. Twelve samples were collected from shear zones proposed in the literature (e.g., Appel et al., 1998; Nutman & Friend, 2009). Fourteen samples are from proposed high strain subterrane, whereas eight samples are from an area proposed to be a low strain subterrane (Tables 1 and 2; Figures 8a, 8b, and S2b) (e.g., Appel et al., 1998; Nutman & Friend, 2009). Samples were cut, polished, and made into XZ-plane thin sections, where the “X” denotes the down plunge direction of lineation, and “Z” denotes the pole to the foliation pointing upwards. Because all the sample names start with “JZ17,” for the sake of simplicity, we shortened these labels in this text (e.g., the full name of sample 714-4 in this study is JZ17714-4). Most sample names in this study are collected as a matching set to the samples of our accompanying study (Ramírez-Salazar et al., 2021), but there are a few distinctions, as explained in the supporting information. Photomicrographs were taken using a Leica petrographic microscope (for small-area plane-polarized light and cross-polarized light images) and a film scanner (for thin-section size plane-polarized light images) at the University of Hong Kong. Scanning electron microscope (SEM) images were taken with a Tescan VEGA3 XM SEM at the University of Leeds. Mineral modes are estimated from the SEM and thin section images (Table 1). We scanned the thin sections at an accelerating voltage of 20 kV and working distances of ~15 mm using an LEO 1530 scanning electron microprobe equipped with an EBSD detector. The scan areas are selected across quasi-homogeneous, multiphase assemblages or quartz-rich domains/veins. Deformed fabrics in these areas appear to be uniform and parallel to the lineation directions (Figure S4). The step sizes were generally ~5–10 μm to allow for the smallest visible quartz grains in thin sections to have at least four indexed pixels. We eliminated grains smaller than four pixels in the EBSD data and interpret them as analytical noise or polishing defects. Points with mean angular deviations larger than 1° were discarded to avoid erroneous indexing. We used the HKL Channel 5 software and the free tool MTEX (Bachmann et al., 2010) for the postanalysis processing of indexed EBSD data, such as data smoothing, grain detection,

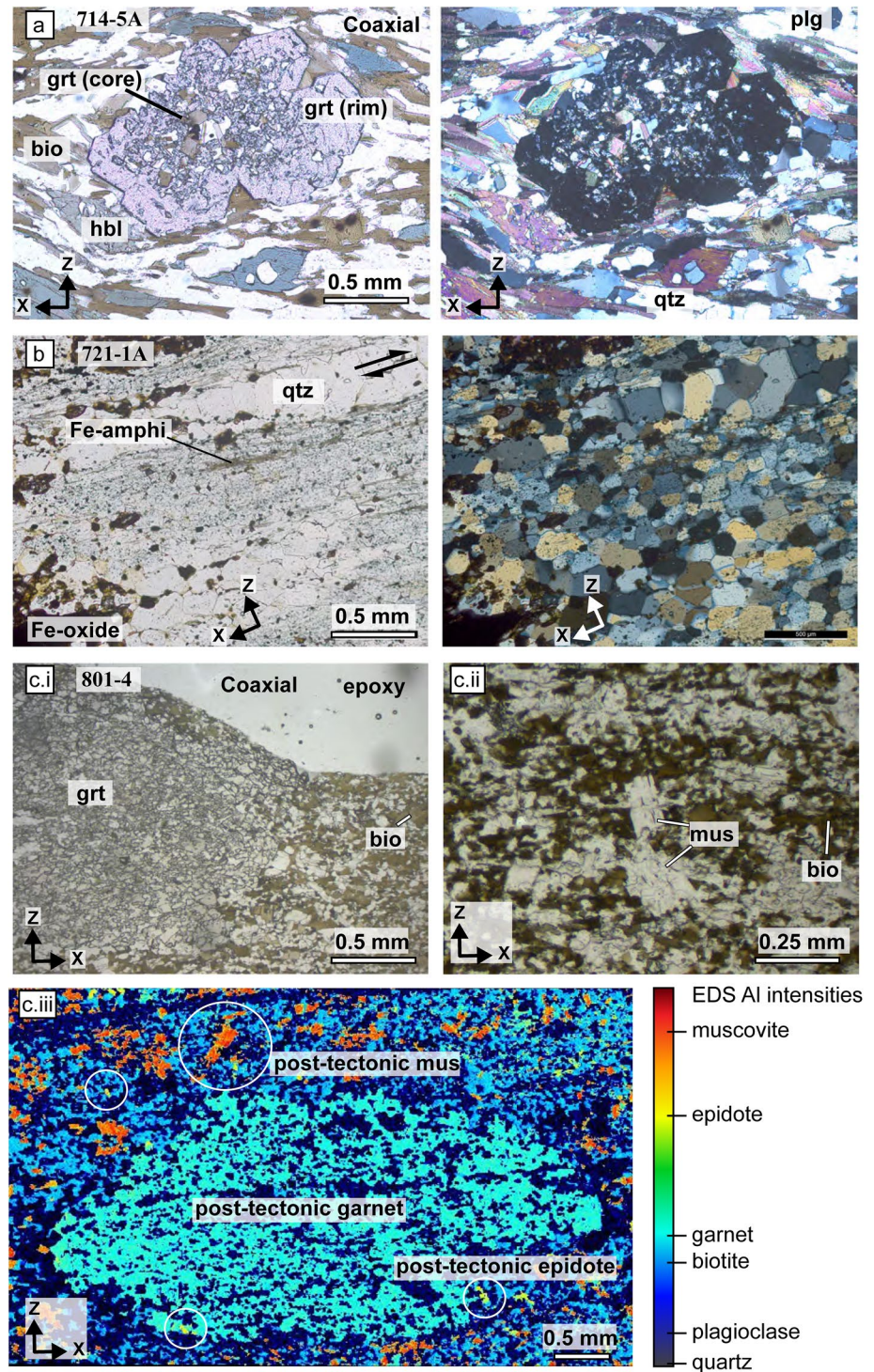


Figure 4.

map generation (e.g., Figure S4), plotting of pole figures of crystallographic axes (one point per grain, lower hemisphere, and equal area) (Figure 5), plotting of inverse pole figures of misorientation axes of subgrain boundaries, and calculation of the texture indexes (see below).

Quartz grains were reconstructed from indexed EBSD data (Figure S4). Grain boundaries were defined by $\geq 10^\circ$ misorientation. Subgrain boundaries were defined by 2° – 10° misorientation. Dauphiné twin boundaries were recognized by 60° rotation around the *c*-axis. We overlaid the quartz grain maps on respective band contrast maps to check the quality of grain reconstruction. The grain reconstruction results were accepted if (1) the reconstructed grains match the band contrast maps, (2) there were at least 200 grains identified, and (3) no artificial grains were generated by data smoothing processes. For the reconstructed quartz grains, we used their areas to calculate their equivalent diameters ($2 \times \sqrt{\text{area} / \pi}$). Grains cut by the boundaries of scanning areas are excluded from the area calculation, as the true areas of these grains cannot be obtained. We then generated the number-weighted and volume-weighted histograms of diameters, and respective number-weighted mean and volume-weighted mean of diameters for each sample (Figure S5).

Acquired quartz CPO statistics can reflect strain information such as shear sense and/or deformation temperatures (Figure 3) (Law, 2014). The asymmetry of the *c*-axis or *a*-axis skeleton with respect to the reference frames (*X* & *Z* directions) can be used to determine the sense of shear and estimate the kinematic vorticity (Law, 1990). The quantitative kinematic vorticity number can only be estimated assuming homogeneous and steady-state flow. However, the deformation paths of the Isua supracrustal rocks could have been complicated by overprinting due to multiple stages of tectonism (see above, Figure 2) (a la Price, 1972). Therefore, the kinematic vorticity estimation can only be qualitative (i.e., noncoaxial vs. coaxial) (e.g., Law, 1990; Xypolias & Koukouvelas, 2001).

The CPO statistics can be (semi-)quantitatively represented by texture indexes such as the J-index (Bunge, 2013), M-index (Skemer et al., 2005) or point (*P*), girdle (*G*), and random (*R*) values (Vollmer, 1990; Woodcock, 1977). J-index reflects the strength of the CPO pattern of a specific crystallographic axis in a pole figure. A completely random distribution of CPO would yield a J-index of 1, whereas a purely uniform CPO (for example, only one defect-free grain is plotted) would yield an infinite J-index. A similar index is the M-index, which is calculated from CPO statistics from multiple axes. $M = 0$ denotes a totally random CPO, whereas $M = 1$ denotes a purely uniform CPO. *R*-values of the *P*, *G*, and *R* systems could also reflect CPO strength, where $R = 1$ denotes a lack of CPO and a smaller *R*-value indicates a stronger CPO. The *P*- and *R*-values can indicate the constriction, flattening, or plane strain components in general shear when *R*-value is low (see Barth et al., 2010 for a review). Higher J-index, M-index or lower *R*-values derived from quartz fabrics can generally reflect higher strain intensity assuming the deformation is mostly absorbed by quartz (e.g., Heilbronner & Tullis, 2006). In contrast, in polyphase rocks, low J-index, M-index or higher *R*-values are expected because some strain could concentrate on other phases rather than quartz (e.g., Cross et al., 2017; Little et al., 2015). However, subgrain boundary characteristics and textural index data may still be used for slip system analysis and strain intensity analysis.

Symmetry versus asymmetry seen in pole figures is used to identify deformation types in terms of coaxial and noncoaxial deformation, respectively. If the pattern is asymmetric, shear sense can be derived (Figure 3) (e.g., Law, 1990). The dominant slip system activated in quartz grains can be determined using pat-

Figure 4. Representative photomicrographs of major petrologies and microstructures of samples from the Isua supracrustal belt. (a) An amphibolite with a two-phase garnet crystal: a pre-tectonic core (highlighted by randomly oriented biotites) and a posttectonic rim. (b) A metachert/BIF showing recrystallized quartz and foliated, needle-like Fe-rich amphiboles. (c) A carbonated felsic rock showing post-tectonic growth of garnet as indicated by the lack of folding in surrounding matrix (i and iii). Post-tectonic metasomatism/metamorphism may have also led to the growth of muscovite and epidote that cross-cut the earlier foliation (ii and iii). The (c) iii image is generated by a free tool XMapTools (Lanari et al., 2014), which shows an aluminum intensity map obtained by energy-dispersive X-ray spectroscopy (EDS). Typical post-tectonic minerals are highlighted. (d) A back-rotated elongated garnet (ii) (a la Ghosh & Ramberg, 1976) generated during top-to-southeast shear. Inset (i) is a backscatter electron image showing curved inclusion trails due to the rotation. An annotated thin section image (iii) highlights the elongated shape of this garnet grain, the curved inclusion trails, and the deformed mica traces in matrix. (e) A rotated syn-tectonic garnet grain (i) and S-C fabrics (iii) indicate top-to-southeast shear sense. An annotated thin section image (ii) highlights the shape of this garnet grain, inclusion trails, and folded mica traces in the matrix. (f) Pressure shadows of garnet grains showing top-to-southeast shear sense. (g) Recrystallized plagioclase sigma due to top-to-southeast shearing (left: plane-polarized light; right: cross-polarized light of the same area). (h) Shear band boudins (highlighted in ii) in a metachert/BIF sample (i) showing top-to-northwest shear sense. (i) Relict Fe-amphiboles mineral fishes (highlighted in ii) formed in a metachert/BIF sample due to top-to-northwest shearing. Abbreviations: bio, biotite; car, carbonates; Fe-amphi, Fe-amphiboles such as grunerite; ilm, ilmenite; mus, muscovite; plg, plagioclase; hbl, hornblende; qtz, quartz.

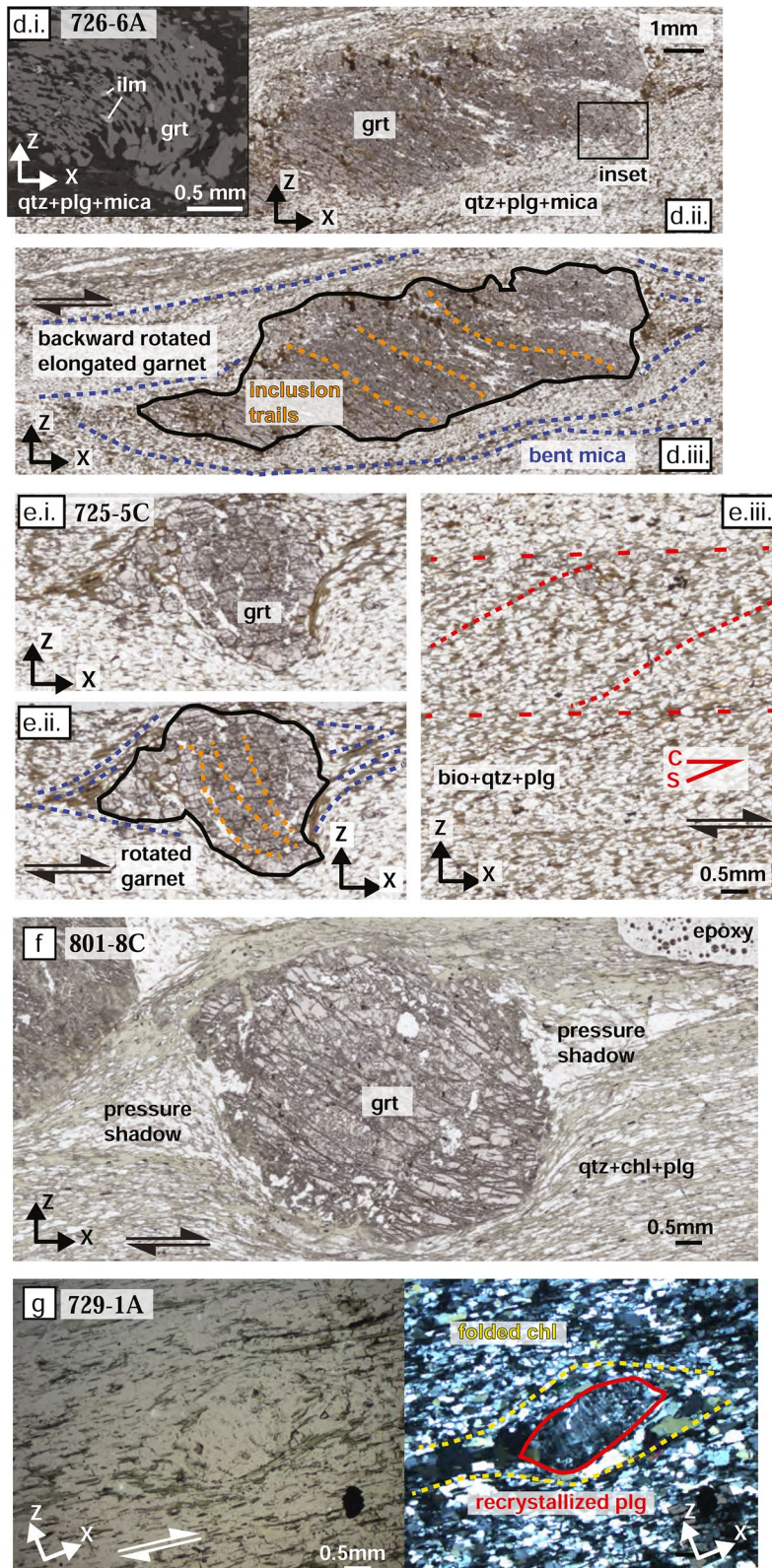


Figure 4. Continued

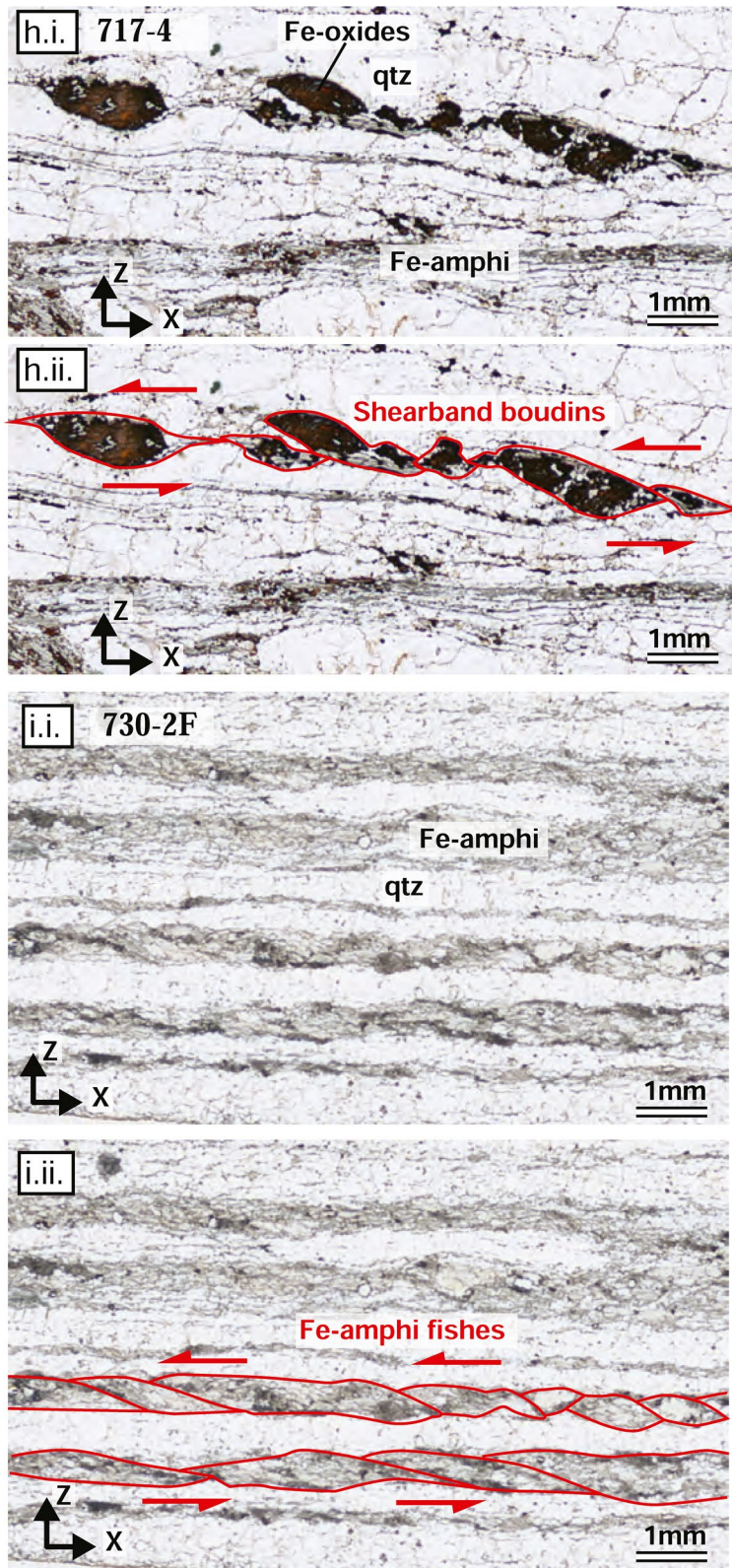


Figure 4. Continued

prism <a> slip dominant

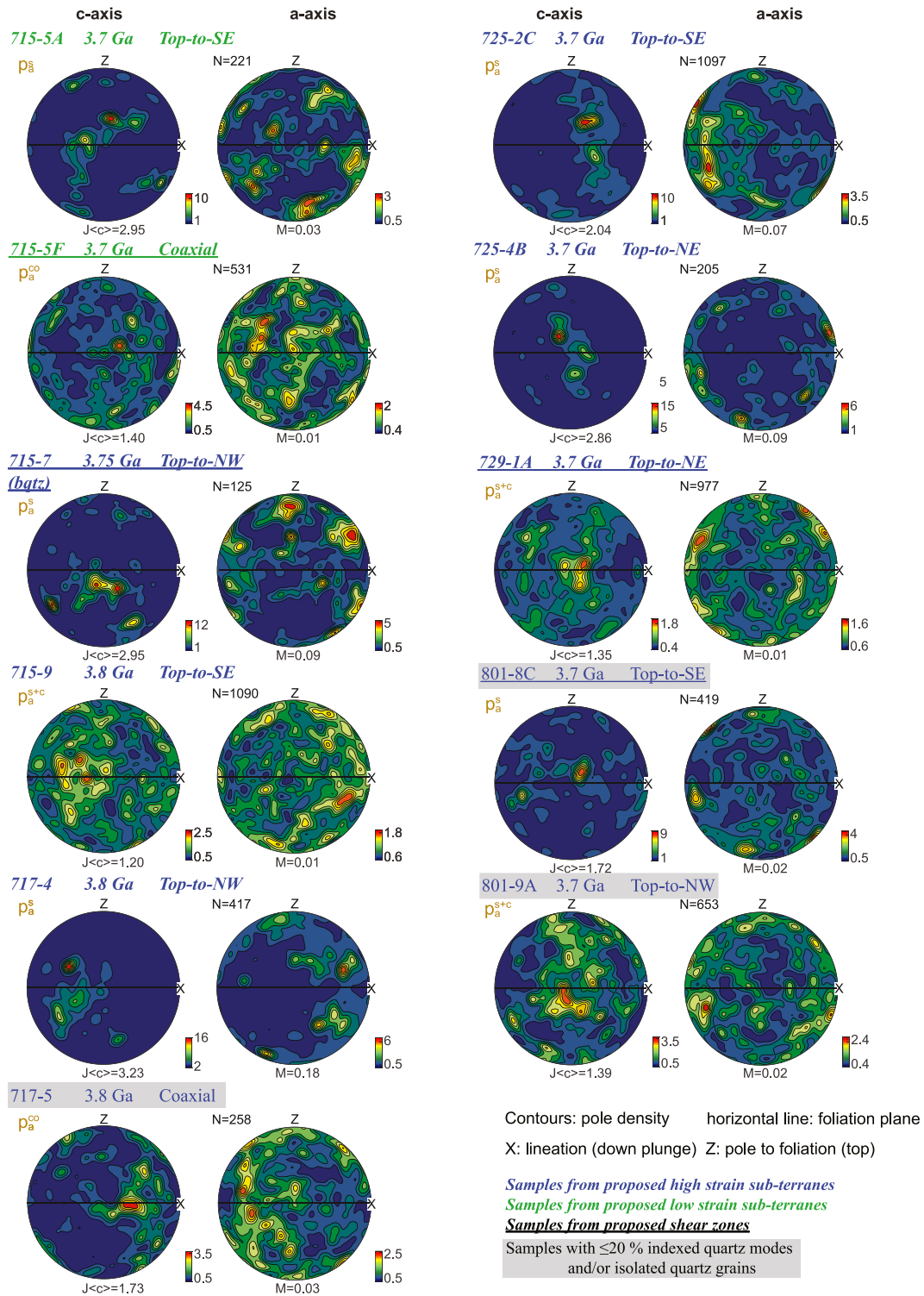


Figure 5. Quartz CPO c-axis and a-axis pole figures of samples from the Isua supracrustal belt. Data are grouped by dominant quartz slip systems interpreted from the pole figures. In each group, the samples are ordered alphabetically. Text provides sample names, sample deposition/crystallization ages, and interpreted shear senses from the pole figures. The styles of sample names (as explained in legend) reflect their positions relative to proposed subterrains and shear zones (e.g., Appel et al., 1998; Nutman & Friend, 2009) as well as their indexed quartz modes. Slip systems interpreted from CPOs of samples with isolated quartz grains and/or $\leq 20\%$ indexed quartz modes can be unreliable because this approach was built on studies focusing on quartz aggregates (e.g., Stipp et al., 2002). On the left of each set of pole figures, the interpretive code for this quartz CPO pattern (as shown in Figure 3) is provided.

prism <c> slip dominant

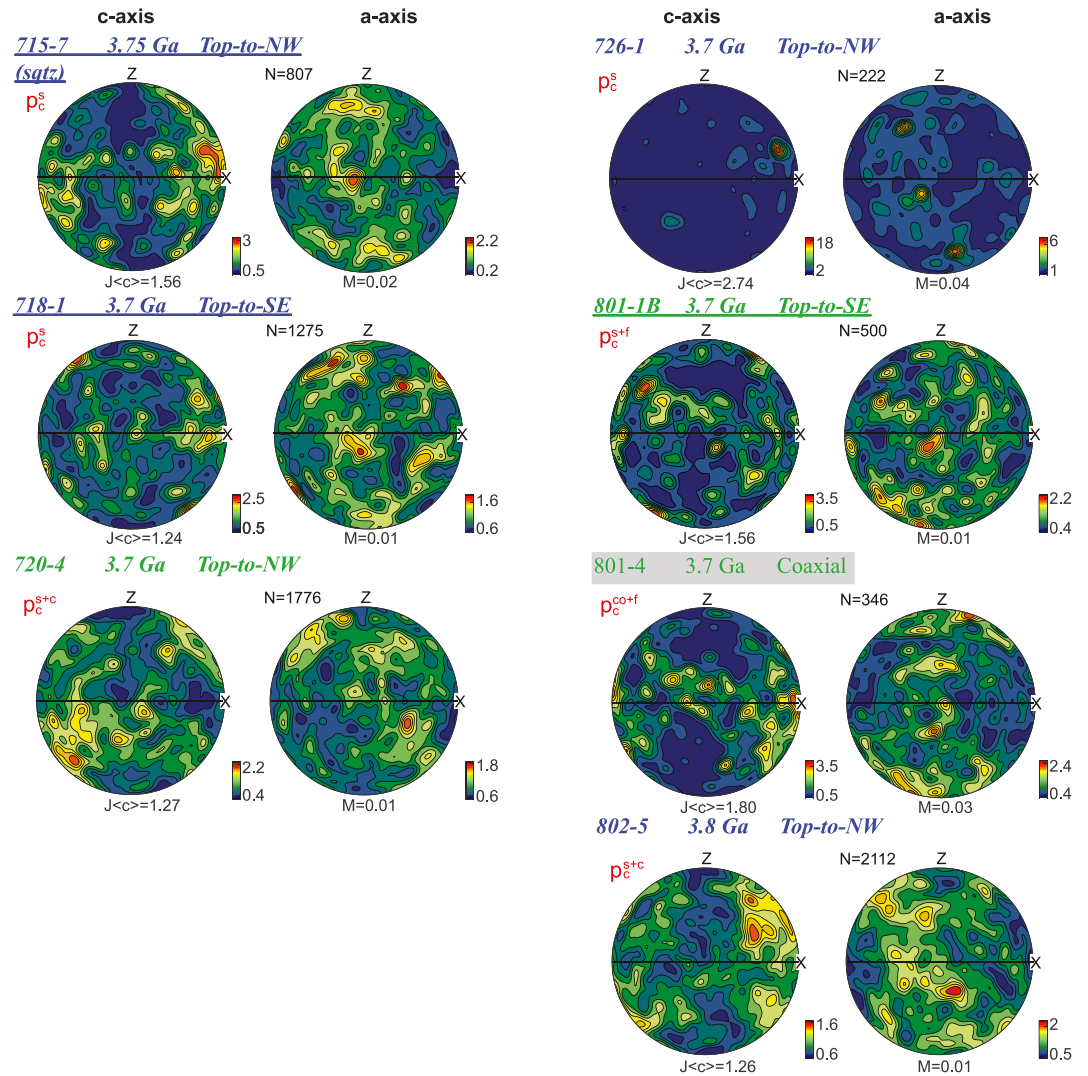
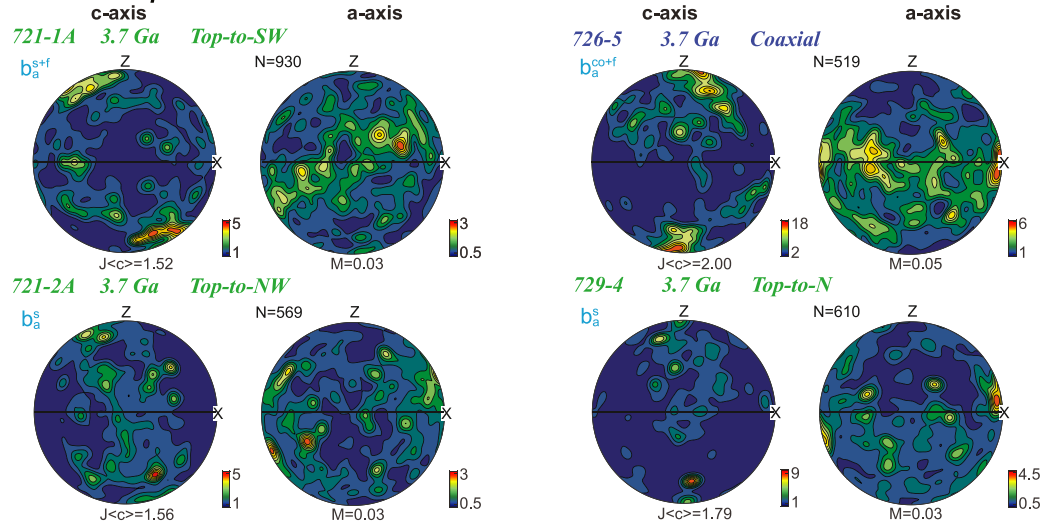


Figure 5. Continued

terns shown on pole figures (Figure 3b). Slip system activation has been proposed to be mainly temperature-dependent. Based on naturally deformed quartz-rich rocks (e.g., quartzites), Kruhl (1998) and Stipp et al. (2002) summarize that quartz would dominantly deform via basal $\langle a \rangle$, rhomb $\langle a \rangle$, prism $\langle a \rangle$ or prism $\langle c \rangle$ slip systems at $\sim 300^\circ\text{C}$ – 400°C , $\sim 400^\circ\text{C}$ – 500°C , $\sim 500^\circ\text{C}$ – 650°C or $>650^\circ\text{C}$, respectively (Figure 3a). However, many studies suggest that other factors would change these thresholds (Figure 3a) (see Law, 2014 for a review). Specifically, water weakening has been reported to enable prism $\langle c \rangle$ slip at temperatures as low as $\sim 550^\circ\text{C}$ – 600°C (e.g., Garbutt & Teyssier, 1991; Okudaira et al., 1995). Similarly, grain size reduction in lower-amphibolite facies shear zones was found to promote the c-axis CPO maximum closer to the X-direction (i.e., prism $\langle c \rangle$ style) (Kilian et al., 2011). Finally, a low strain rate would reduce the temperature required for transitioning to prism $\langle c \rangle$ dominance (Blacic, 1975; Kruhl, 1998; Tullis et al., 1973).

The dominant slip system activated in quartz can also be constrained via the misorientation axes of subgrain boundaries of quartz grains (e.g., Lloyd et al., 1997; Neumann, 2000). During deformation and recovery, intracrystalline dislocations that accommodate slip may evolve to form subgrain boundaries (e.g., Borthwick & Piazzolo, 2010) and eventually grain boundaries (with relatively higher misorientation) (e.g., Drury & Urai, 1990). Rotation of quartz subgrains along a subgrain boundary would create misorientation

basal <a> slip dominant



mixed slip

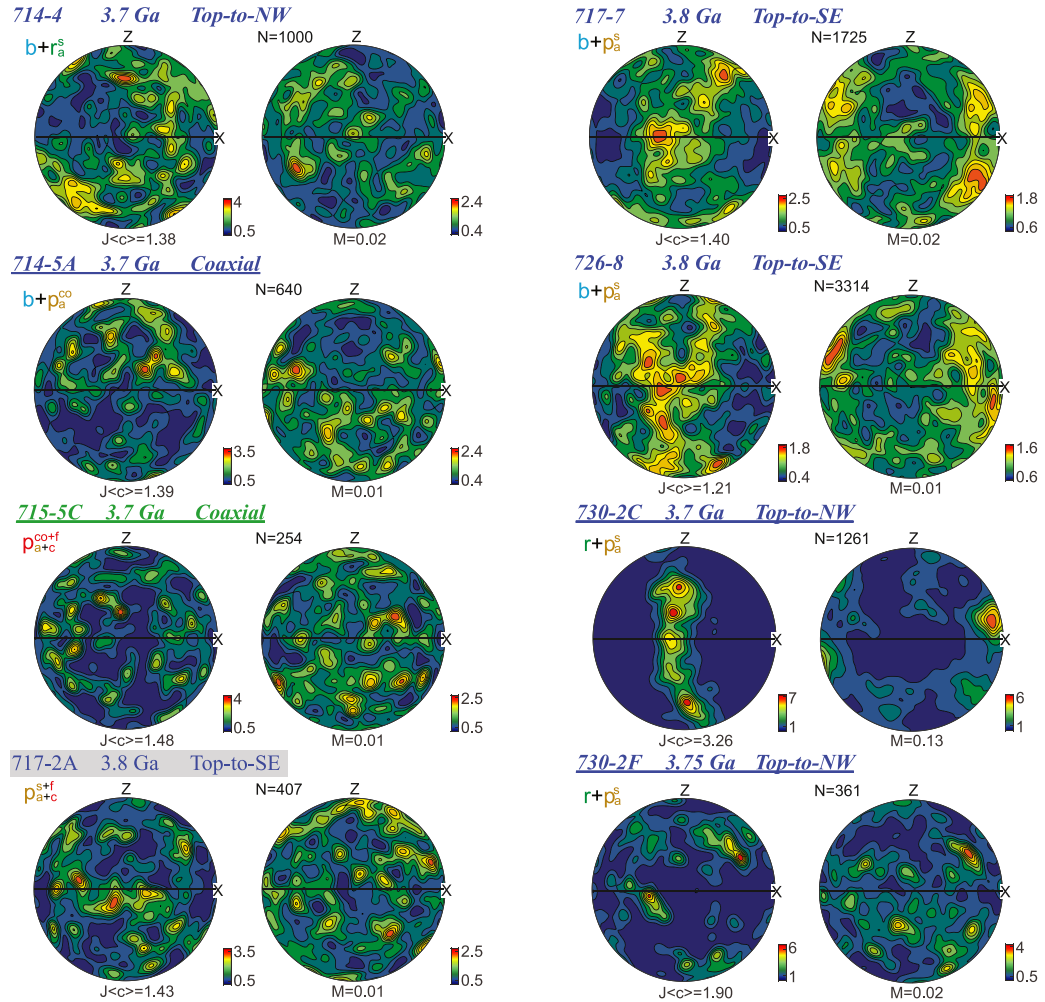


Figure 5. Continued

between two associated crystallites, with the misorientation axis being corresponding to the rotation axis of the activated slip system (some dispersions are possible, e.g., Lloyd et al., 1997; Neumann, 2000). Therefore, with an inverse pole figure (Figure 3c), a large data set (>100 is generally acceptable; Prior, 1999) of misorientation axes of subgrain boundaries in a sample can limit the dominant slip systems that formed the subgrain boundaries.

4. Results

Our samples comprise five lithologies: (1) quartz-bearing amphibolite, (2) garnet-biotite amphibolite, (3) felsic metavolcanic rocks, (4) metachert/BIF, and (5) metatonalites (Table 1; Figure 4). Their petrology and mineral assemblages are consistent with previous studies (e.g., Arai et al., 2015; Komiyama et al., 2002; Myers, 2001; Nutman et al., 1996, 2002). Quartz-bearing amphibolites generally contain (in decreasing modal percentages) amphibole, plagioclase, quartz, and biotite. Garnet-biotite amphibolite generally has biotite, quartz, plagioclase, amphibole, and garnet. Felsic metavolcanic rocks usually have quartz, biotite, plagioclase, K-feldspar, and muscovite. Metachert/BIF samples have quartz, Fe-amphiboles (e.g., cummingtonite or grunerite), and Fe-oxides (e.g., magnetite or hematite) (Figure 4b), with total modes of Fe-oxides and phyllosilicates, such as mica or amphiboles from ~5% to ~80% (Table 1). Metatonalites have quartz, feldspar, epidote, and muscovite. In all rocks, most of the phyllosilicate minerals (e.g., mica and amphibole) are aligned with foliations, sometimes forming interconnected bands (Figures 4 and S4). Chlorite, epidote, and muscovite occur in some samples (Table 1) as retrograde phases that overprint or cross-cut earlier minerals (Figures 4a, 4c, 4f, and 4g). Garnets occur in some samples (Table 1) with pre/syn-tectonic cores surrounded by deformed phyllosilicate minerals (Figures 4a and 4d–4f). Post-tectonic growth of garnet occasionally can be identified as overgrowth rims that cross-cut earlier foliations (Rollinson, 2002, 2003). In two samples (718-1 and 801-4), all garnet grains appear to be post-tectonic (Figure 4c). These post-tectonic garnets appear to overprint or overgrow the earlier quartz fabrics. Quartz grains in all samples have experienced dynamic recrystallization resulting in sutured grain boundaries when in contact with other quartz grains (Figures 4a, 4b, and 4h–4i) as well as drag and window textures associated with presence of phyllosilicate minerals (Figures 4a–4c and 4h–4i).

The quartz grains of four (725-5B, 726-6A, 729-10 and 801-6A, Table 2) out of 33 samples cannot be successfully reconstructed with the EBSD data due to relatively low degrees of indexing for a significant number of quartz grains (Figure S4). Accordingly, their quartz textures will not be discussed here. Nonetheless, their microscopic observations (i.e., lithologies and shear sense indicators in thin sections) are still valid and are used in this contribution.

Quartz grains in the remaining 29 samples feature either equant, polygonal shapes with straight boundaries (e.g., 714-4, 715-5C, 721-1A, 721-2A), or elongated, lobate, ameboid- or finger-shapes with elongation directions being subparallel to foliations (e.g., 714-5A, 718-1, 715-7sqtz, 720-4, 726-1, 726-5, 802-5), or large, ameboid shapes with irregular sutured boundaries (e.g., 715-5A, 715-7bqtz, 725-4B, 730-2C) (Figure S4). Most quartz grains in these samples yield ≤ 200 μm equivalent diameters. Some samples (715-5A, 715-7bqtz, 717-4, 718-1, 721-2A, 725-4B, 726-1, 729-4) preserve quartz grains that have ~ 200 – 500 μm equivalent diameters. There are also samples (715-5C, 715-9, 726-8, and 801-1B) that are dominated by quartz grains that show ≤ 50 μm equivalent diameters, such that their number-weighted mean and volume-weighted mean diameters are all less than 51 μm (Figures S4 and S5). In five samples (717-2A, 717-5, 801-4, 801-8C, and 801-9A), quartz grains are mostly isolated, that is, surrounded by other phases, and the modes of indexed quartz are less than 20% (Figure S4). In the other 24 samples, quartz grains form aggregates or bands, and the modes of indexed quartz are larger than or equal to 30% (Table 2).

Six samples show identifiable shear sense indicators in thin sections, such as rotated garnets (725-2C, 726-6A, Figures 4d and 4e), C-S fabrics (725-2C, Figure 4d), asymmetric pressure shadows (801-8C, Figure 4f), feldspar sigma clasts (729-1A, Figure 4g), shearband boudins (717-4, Figure 4h), and mineral fishes (730-2F, Figure 4i). These shear sense indicators show either top-to-southeast (725-2C, 726-6A, 801-8C, and 729-1A) or top-to-northwest (717-4, 730-2F) shear senses. Quartz CPO pole figures from the twenty-four quartz-rich samples (i.e., with $\geq 30\%$ indexed quartz modes and/or quartz bands/aggregates) show dominantly top-to-southeast (7 samples) and top-to-northwest (10 samples) shear senses. Only singular samples show different

shear directions, that is, top-to-north (1 sample), top-to-northeast (1 sample), or top-to-southwest (1 sample) shear senses. Four samples show coaxial strain (Table 2; Figure 5). Quartz CPO pole figures for five quartz-poor samples (i.e., with $\leq 20\%$ indexed quartz modes and/or isolated quartz grains) also show a range of shear senses, including top-to-southeast (2 samples), top-to-northwest (1 sample) shear, and coaxial strain (2 samples). Samples with thin section shear indicators show consistent EBSD results (Figures 4d–4i, and 5). The shear senses appear to have no systematic relationship with rock ages, dominant quartz slip systems, or their relative locations with respect to the proposed shear zones (Table 2; Figures 8 and 9d–9e). Specifically, shear senses of samples from the same proposed shear zone could be different. For example, the “dividing sedimentary unit” (shear zone “1B” in Figures 8a and 8b) samples 715-7 and 730-2F both show top-to-northwest shear sense, whereas sample 726-6A from the same unit shows top-to-southeast shear sense (Figure 4e).

In quartz CPO pole figures (Figure 5), the majority of the quartz-rich samples show activation of quartz prism $\langle a \rangle$ or prism $\langle c \rangle$ (13 samples) slip systems, with some of them showing mixed slip (7 samples) or basal $\langle a \rangle$ slip (4 samples). Note that in samples featuring mixed slip patterns, prism $\langle a \rangle$ or prism $\langle c \rangle$ slip could still be major components (Figure 5). The five quartz-poor samples show a dominance of prism $\langle a \rangle$ (3 samples) and prism $\langle c \rangle$ slip (1 sample), with one sample showing mixed slip (Figure 5; Table 2). We note that three out of four samples showing basal $\langle a \rangle$ slip are located near the northeastern end of the belt, which may have experienced lower metamorphic conditions (Arai et al., 2015) or higher metasomatic activities (Ramírez-Salazar et al., 2021; Webb et al., 2020) compared to the rest of the belt. Another case is distinctive: sample 715-7 has two quartz-rich bands showing different quartz grain sizes and phyllosilicate mineral abundances, yielding two types of quartz CPO patterns. The band with dominantly $\sim 10\text{--}100\ \mu\text{m}$ quartz grains and ~ 15 modal percentage Fe-amphiboles (715-7 bqtz) shows prism $\langle c \rangle$ slip, whereas the other band with dominantly $>150\ \mu\text{m}$ quartz grains and <5 modal percentage Fe-amphiboles shows prism $\langle a \rangle$ slip (Figure 7a). Both bands show top-to-northwest shear sense (Figure 5).

All samples yield $J_{\langle c \rangle}$ -indexes (J -indexes of quartz c -axis pole figures, same below) from 1.20 to 3.26, M -indexes from 0.01 to 0.18, and R -values from ~ 0.2 to ~ 0.9 (Table 2; Figures 5, 8, and S6). Due to the overall high R -values, the constriction or flattening components in these pole figures cannot be determined (Table 2; Figure S6) (Barth et al., 2010). To search for signals that indicate strain localization within proposed shear zones or proposed subterraces (e.g., Appel et al., 1998; Nutman & Friend, 2009) (Figure 2), we plotted histograms that compare texture indexes of samples from different lithological units (Figures 8a, 8b, and S6), from different age parts of the belt (Figure 8c), from within or out of the proposed shear zones (Figure 8d), from different proposed subterraces with contrasting strain histories (Figure 8e), and of different shear senses (Figure 8f). We found that no specific group of samples show systematically higher texture indexes compared to other complementary groups (Figures 8 and S6; Table 2). We also plotted texture indexes with samples' indexed quartz modes (Figures 8g–8i). These diagrams show that 17 out of 24 quartz-rich samples have $J_{\langle c \rangle}$ -indexes below 2, and only two quartz-rich samples have $J_{\langle c \rangle}$ -indexes above 3. All quartz-poor samples show $J_{\langle c \rangle}$ -indexes below 2. The modal abundance of quartz in our samples appear to have had some control on the CPO intensities, but such control was much weaker compared to Alpine Fault zone, New Zealand samples ($\sim 1.2\text{--}3.3$ vs. $\sim 1.0\text{--}12$, $J_{\langle c \rangle}$ values) studied by Little et al. (2015) (Figure 8i), in which they examined compositional layers of varying quartz modal abundances in amphibolitic rocks from a section of fault. Moreover, differences in the texture indexes of our samples are much smaller than the variances observed across a major fault zone (which may localize the strain to create stronger CPO strengths in quartz). For example, quartzite samples from within 200 or >200 m away of the Main Central thrust of the Himalaya yield M -indexes of 0.08–0.34 or 0–0.20, respectively (Starnes et al., 2020). In contrast, the M -indexes of our samples (regardless of indexed quartz modes) are mostly less than 0.1, except two outliers (717-4 and 730-2C) which still have relatively small M -indexes of 0.18 and 0.13, respectively (Table 2; Figure S6).

In contrast to the large diversity in the CPO-inferred dominant slip systems in quartz, analysis of the preference of misorientation axes of subgrain boundaries (Figures 6 and S4) shows higher constancy between samples. Most of quartz-rich and quartz poor samples show dominance of rotation axes of quartz slip systems parallel to the c -axes. Such a signal corresponds to prism $\langle a \rangle$ slip (Figure 6). Within these samples, except for 715-5A, 715-5F, and 729-1A (which show dominant prism $\langle a \rangle$ slip in quartz CPO pole figures, Figure 5), significant numbers of misorientation axes of subgrain boundaries also plotted along the peripheral representing m - a - m directions (Figure 6). Therefore, those misorientation axes also record basal $\langle a \rangle$

and/or prism $\langle c \rangle$ slip (Figure 3c). Only two samples show different results in the distribution of subgrain boundaries' misorientation axes (Figure 6). A quartz-rich sample 801-1B shows a maximum density of rotation axes parallel to the pole of $\{z\}$, matching dominance of rhomb $\langle a \rangle$ slip. A cluster near $\langle a \rangle$ direction appears as the secondary maximum of subgrain boundaries' misorientation axes of sample 801-1B, which corresponds to activation of both prism $\langle c \rangle$ and rhomb $\langle a \rangle$ slip (Figure 6). A quartz poor sample 801-4 shows a maximum near $\langle a \rangle$ direction, with a significant amount of misorientation axes plotted along the peripheral representing slip in $\langle a \rangle$ or $\langle c \rangle$ directions (Figure 6). This pattern indicates dominance of both basal $\langle a \rangle$ and prism $\langle c \rangle$ slip (Figure 3c). In most samples (e.g., 715-7sqtz, 721-1A, 730-2C), identified subgrain boundaries only occur in small fractions of quartz grains, whereas bigger fractions of quartz appear to lack intracrystalline strain or dislocations (e.g., no bending or subgrain boundaries). In contrast, most quartz grains in sample 715-5A, 715-7bqtz, 717-4, 717-7, and 726-5 appear to preserve subgrain boundaries, though the density of these is low (Figures 7 and S4). The traces of most identified subgrain boundaries are straight or slightly curved, with lengths ranging from one-third, to similar values of the diameters of quartz grains. Some subgrain boundaries are much shorter, and sometimes feature curved traces (Figure S4).

5. Discussion

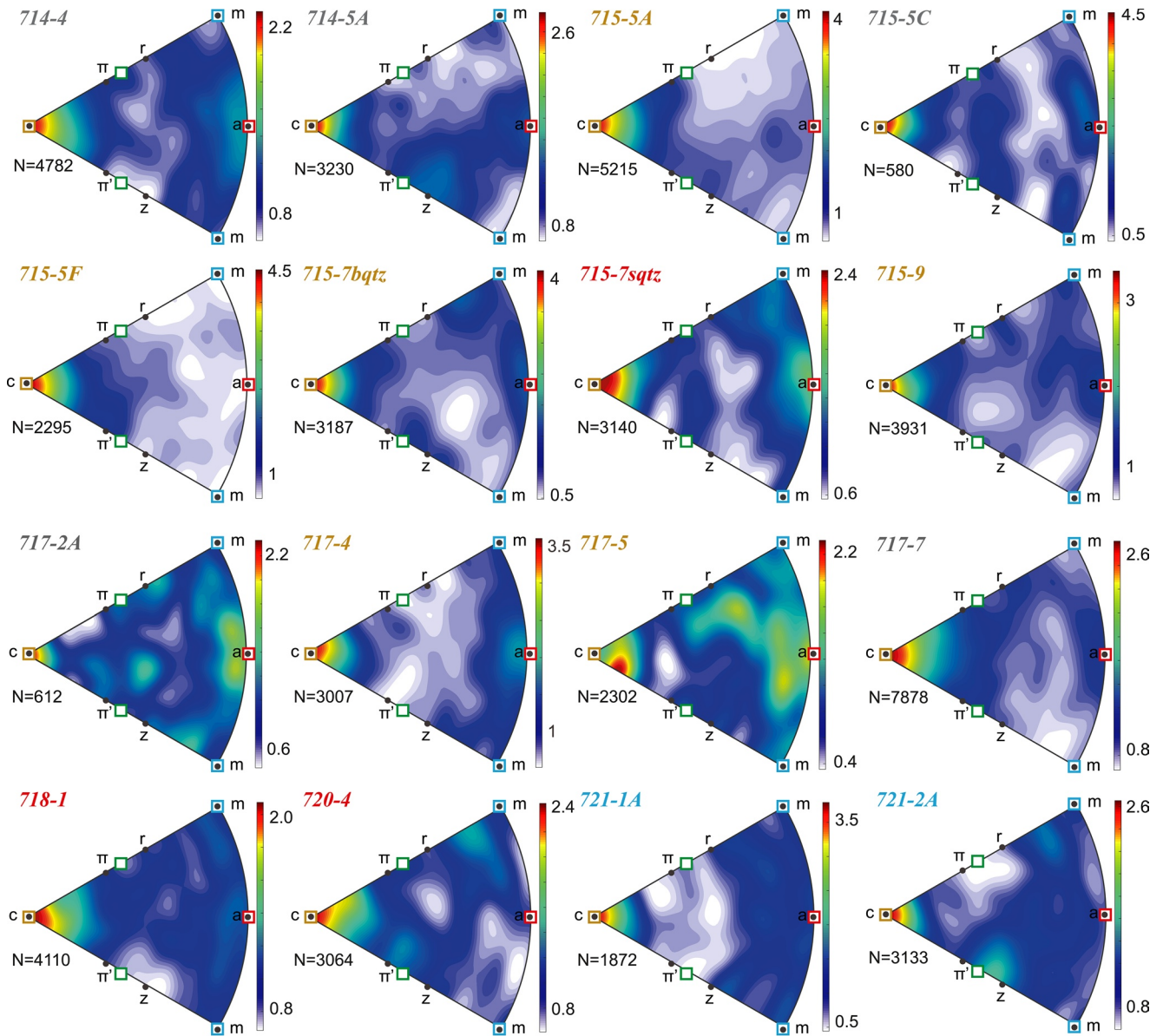
Our quantitative microstructural data from quartz CPO pole figures (Figure 5) show that rocks from the eastern Isua supracrustal belt, regardless of their ages, lithologies, or positions relative to inferred shear zones, preserve dominantly prism $\langle a \rangle$ to prism $\langle c \rangle$ quartz slip systems (17 out of 29), opposing top-to-northwest or top-to-southeast shear senses (21 out of 26 samples showing noncoaxial strain), and quasi-uniformly-low quartz CPO strengths (all quartz fabric M-indexes are under 0.1 except for two outliers at 0.13 and 0.18) that developed during syn-tectonic growth of amphibolite facies minerals like garnet. The microstructural data from inverse pole figure plots of subgrain boundaries' misorientation axes (Figure 6) show dominance of prism $\langle a \rangle$ slip (27 out of 29 samples), with two samples featuring dominantly prism $\langle c \rangle$ and/or basal $\langle a \rangle$ slip systems. No ≤ 100 -m-scale, discrete shear zones that would have localized strain can be identified within our quartz fabric strength data, consistent with the lack of such zones as identified in the field (Webb et al., 2020). Furthermore, interpretation of the “dividing sedimentary unit” as the top-to-south subduction interface appears inconsistent with the opposing shear senses recorded in samples from this unit (715-7 and 730-2F vs. 726-6A) (Figures 4d, 4i, 8a, and 8b) (Table 2). In the following sections, we discuss the implications of these findings for the viabilities of proposed tectonic models, the deformation conditions of the observed strain, and the P-T-t evolution of the Isua supracrustal belt.

5.1. Viability of Proposed Tectonic Models

Proposed tectonic models predict contrasting strain distributions (i.e., whether the strain is distributed, or it is localized in m-scale shear zones) and shear sense indicators across the belt (see *Tectonic Models* section). The shearing and horizontal shortening model (Figure 2a) predicts top-to-south shearing during the uplift of the northern tonalite, and some top-to-east-northeast horizontal shearing during the later shortening and folding. These model predictions are not consistent with the observed widespread top-to-north shear sense indicators across the belt.

The southward subduction model predicts top-to-north shearing along numerous m-scale discrete shear zones during subduction (Figure 2b). Proposed later wedge extrusion along a structurally high, top-to-south shear zone (i.e., the boundary between the Isua supracrustal belt and south metatonalite) predicts a local reversal of shear sense. These predicted shear zones are not identified with our quartz fabric strength data. The spatially random distribution of opposing top-to-southeast and top-to-northwest shear sense indicators across the belt (Figures 8 and 8) does not agree with the model predictions that the top-to-south shear sense indicators should only be observed at or near the proposed structurally high shear zone.

The northward subduction model (Figure 2c) predicts top-to-south shearing along discrete m-scale shear zones during both the ca. 3.7–3.66 Ga arc-collision stage and the ca. 3.66–3.61 Ga orogenic collapse stage (Nutman et al., 2013b). This model also involves a subterranean preserving significantly lower strain versus other proposed subterranean in the Isua supracrustal belt (e.g., Appel et al., 1998; Nutman et al., 2007). Rocks



Inverse pole figure with 2°-10° boundaries' misorientation axes in crystal coordinate systems

- rotation axes of quartz slip systems in Fig. 3
- c, a, m, r, z, π, π': quartz crystal directions

Sample names are color coded via the dominant slip systems as indicated by their CPO pole figures.

Basal<a> Prism<a> Prism<c> Mixed

Figure 6. Inverse pole figures (in crystal coordinate systems) of 2°-10° subgrain boundaries in quartz. Most samples show dominance of prism <a> slip in quartz. The corresponding quartz subgrains and subgrain boundaries are illustrated in Figure S4. Locations of quartz crystal directions and rotation axes of quartz slip systems follow Figure 3c.

within highly strained areas (e.g., shear zones or highly strained terranes) might yield higher texture indexes comparing to rocks from weakly strained areas (e.g., Little et al., 2015; Starnes et al., 2020). However, our microstructural data show no evidence of systematically higher texture indexes within the proposed shear zones (Figure 8d) and in these proposed subterranes (Figure 8e). Such findings may indicate a lack of significant strain localization and preservation of quasiuniform strain intensities across the belt, consistent with our field observations (see Figures 4a and DR2 of Webb et al., 2020). Observed top-to-north

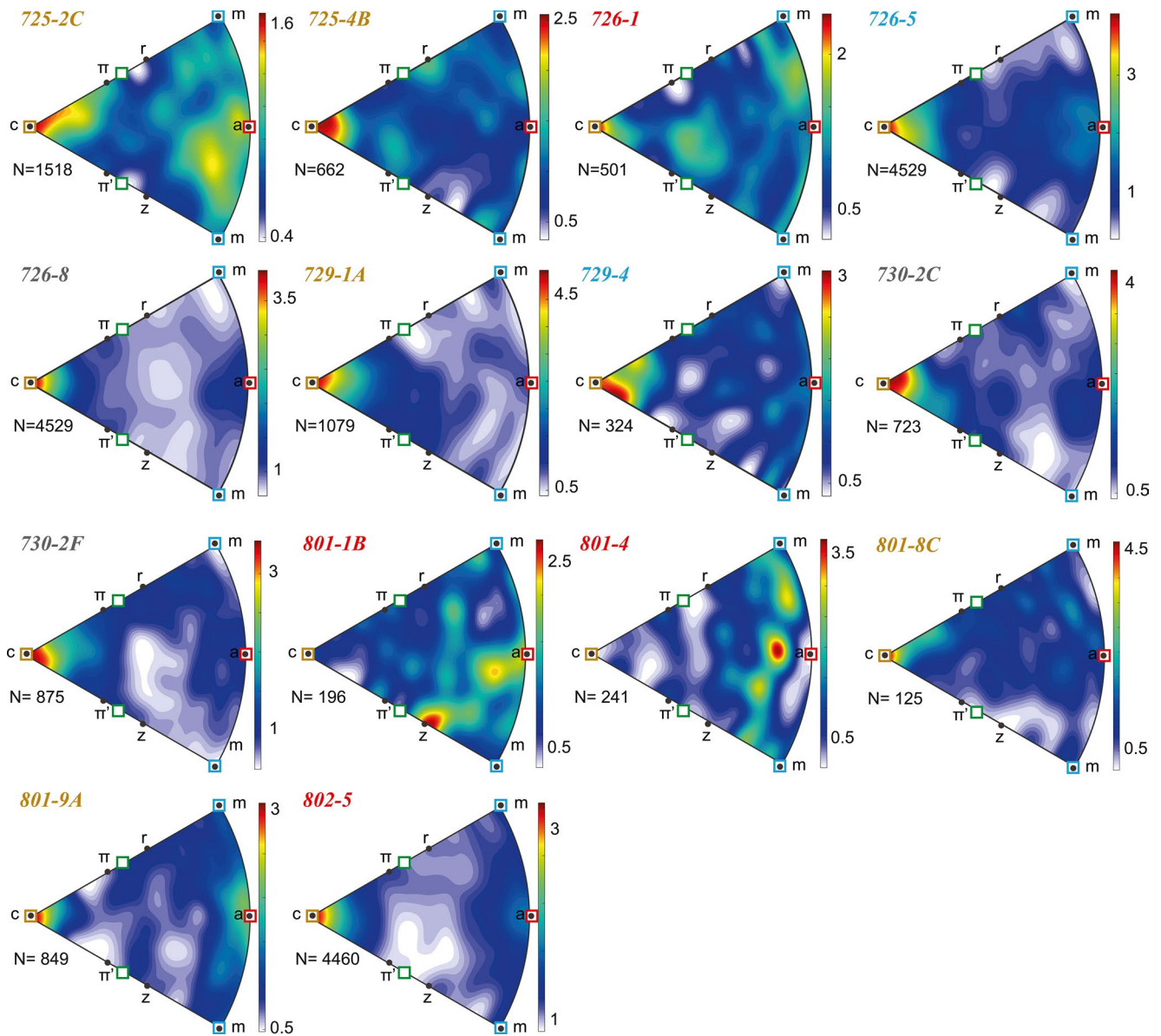


Figure 6. Continued

and top-to-northwest shear sense indicators across the belt and in the proposed top-to-south suture do not match the model predictions (Figures 8a-8f).

The occurrence of quasirandomly distributed, opposing shear sense indicators, quasiuniform quartz fabric strengths, and syn-tectonic garnets across the belt is consistent with the entire belt and adjacent tonalite being deformed into ≥ 0.1 -m-scale sheath and curtain folds under amphibolite facies conditions. Although our structural data are from the eastern belt, published field observations show that the structural geometries and deformation styles of the western belt are similar (Figure 1) (e.g., Hanmer & Greene, 2002; James, 1976; Nutman & Friend, 2009): (1) the entire supracrustal belt features southeast-plunge mineral stretching lineations that are generally subparallel to fold axes of 0.1–1 m-scale curtain folds; and (2) the km-scale fold limbs yield stereographic projection intersections coincident with the projections of lineations (Figure 9c) (Webb et al., 2020). Similar deformation fabrics occur in the ca. 3.8–3.7 Ga metatonalite and the ca. 3.66–3.61 Ga granite/pegmatite sheets, with the exception of the northern part of the ca. 3.7 Ga metatonalite (Figures 9a, 9b, and S1a) (Crowley, 2003; Crowley et al., 2002; Nutman et al., 2013b). Therefore, a reasonable

extrapolation is that the macro-/microstructural patterns of the Isua supracrustal belt and the adjacent metatonalites can all be interpreted as preserving 0.1-m to km-scale sheath and curtain folds and homogeneously distributed strain (Webb et al., 2020). Therefore, our microstructural data, and protolith settings, macrostructures, and metamorphic patterns (see in *Tectonic Models* section) (Ramírez-Salazar et al., 2021; Szilas et al., 2015; Webb et al., 2020) agree with the recent proposal that the geology the Isua supracrustal belt can be interpreted via heat-pipe tectonics, with or without a late Eoarchean transition to plate tectonics (Webb et al., 2020).

5.2. Origins of Observed Structures

Our maximum quartz fabric strength (3.26 $J_{<c>}$ index or 0.18 M-index, Figures 9a, 9b, and S6) is distinctly lower than the highly strained quartzite samples from plate tectonic major shear zones (with $J_{<c>}$ indexes up to ~ 12 and M-indexes up to 0.34). Assuming dominance of dislocation creep, the lack of high quartz fabric strength indicates that the investigated quartz grains record low finite strain. This interpretation seems to be inconsistent with prior observations, as well as the heat-pipe model prediction, indicating that the entire belt has been dramatically stretched and thinned (e.g., Fedo, 2000; Furnes et al., 2007; Webb et al., 2020). However, there are several factors in the Isua supracrustal belt that may have permitted weak CPO development even under high strain. First, the presence of fluids or other phases between quartz, or dominance of small recrystallized grains may promote diffusion creep or grain boundary sliding for deforming quartz at natural conditions (see below) (e.g., Halfpenny et al., 2012; Rahl & Skemer, 2016). These two mechanisms may not produce a CPO (Cross et al., 2017) and could weaken the preexisting CPO (e.g., Cross et al., 2017; Wheeler, 2009; Zhang et al., 1994); Second, abundant weak phases such as biotite, muscovite, or Fe-oxides may form interconnected networks and accommodate most of the strain, leaving the quartz relatively weakly strained and weakly preferably oriented (Cross et al., 2017; Cyprych et al., 2016; Gardner et al., 2019; Gonçalves et al., 2015; Hunter et al., 2016; Little et al., 2015). Third, means of grain size of our samples can be as low as ~ 10 – $30 \mu\text{m}$, a grain size that has been postulated to enable dominance of diffusion creep at amphibolite facies conditions (e.g., Kilian et al., 2011). Consequently, bands of fine-grained quartz may have deformed by diffusion creep. Furthermore, abundant quartz grains in some of our samples (e.g., 720-4, 721-1A, 802-5) show polygonal or lobate shapes, straight boundaries and a tendency of being aligned with the orientations of foliations (Figure S4), features previously linked to grain boundary sliding associated with diffusion or dissolution-precipitation creep (Halfpenny et al., 2012; Rahl & Skemer, 2016). Furthermore, deformed, interconnecting bands of phyllosilicates and Fe-oxides indeed occur in our samples (e.g., Figures 4c–4f, S3, and S4). The difference in $J_{<c>}$ -indexes between quartz-poor samples (all below 2) and quartz-rich samples (many above 2) also implies a connection between secondary phases and quartz CPO intensities. Therefore, during prograde amphibolite metamorphism, presence of fluids, quartz recrystallization and formation of abundant, sometimes interconnecting weak phases such as biotites or amphiboles (Table 2; Figure S5) may have (1) promoted diffusion creep and/or grain boundary sliding, and/or (2) accommodated most of strain, and thus allowed for the development of weak quartz CPO under high strain.

Based on a widely used quartz fabric thermometer (Stipp et al., 2002), the occurrence of basal $\langle a \rangle$ to prism $\langle c \rangle$ dominance in our quartz c -axes pole figures (Figure 5) indicates deformation under greenschist to granulite (i.e., $\sim 300^\circ\text{C}$ to $>650^\circ\text{C}$) conditions. However, this wide temperature range conflicts with petrological observations (for example, there are no relict metamorphic assemblages or chess-board extinction of quartz to confirm $>650^\circ\text{C}$ conditions) (this study and Webb et al., 2020) and results from phase equilibria modeling of syn-tectonic paragenesis (Ramírez-Salazar et al., 2021) which indicate that the entire belt was deformed and metamorphosed under amphibolite conditions prior to ca. 3.5 Ga. Interestingly, the dominant slip system (i.e., prism $\langle a \rangle$ slip) in quartz as defined by the misorientation axes of quartz subgrain boundaries in most samples (Figure 6; Table 2) matches the temperature range constrained by petrological evidence (i.e., amphibolite facies conditions). Below, we discuss the apparent mismatch between the CPO-constrained dominant slip systems in quartz (Figure 5) and the petrological evidence, as well as the misorientation axes plots (Figure 6). We show how these quartz CPO patterns can be interpreted as compatible with amphibolite facies conditions. We note that in the discussions below, all CPO-inferred quartz slip systems are from quartz-rich samples because the relationships between CPO and slip systems were mostly built on quartz aggregates (e.g., Stipps et al., 2002).

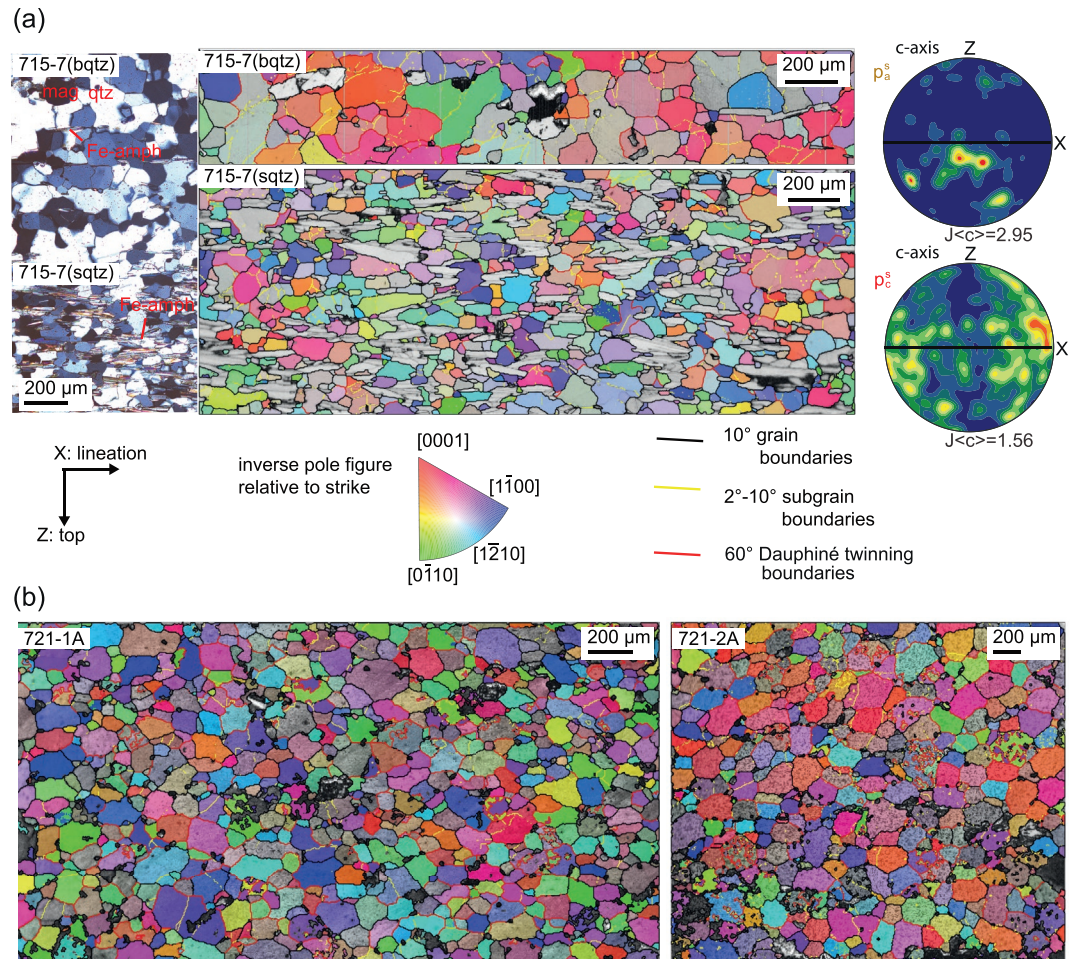


Figure 7. Representative quartz grain maps (overlying band contrast maps). (a) Sample 715-7 has two zones with different dominant quartz slip systems activated. The area with mostly $>150\ \mu\text{m}$ quartz grains and <5 modal percentage Fe-amphiboles (upper) shows prism $\langle a \rangle$ slip, whereas the area with mostly $\sim 10\text{--}100\ \mu\text{m}$ quartz grains and ~ 15 modal percentage Fe-amphiboles (lower) shows prism $\langle c \rangle$ slip. The inverse pole figures only show quartz grains and are color-coded relative to the strike direction. On the right are their c -axis pole figures. The code for quartz CPO patterns on the left of each pole figure is the same as in Figure 3 (b) Samples 721-1A and 721-2A preserve equant, polygonal-shaped quartz grains. These quartz grains show basically no intracrystalline deformation, and the density of subgrain boundaries is low.

First, the observed prism $\langle c \rangle$ patterns do not necessarily reflect $>650^\circ\text{C}$ temperatures. Factors such as low strain rate, water weakening, and/or grain size reduction could reduce the transitional temperature from prism $\langle a \rangle$ to prism $\langle c \rangle$ to $\sim 550^\circ\text{C}\text{--}600^\circ\text{C}$ (Figure 3a) (e.g., Blacic, 1975; J. Kruhl, 1998; Okudaira et al., 1995; Toy et al., 2008; Tullis et al., 1973). Water weakening should have been possible since hydrous minerals (e.g., mica and amphiboles) are present as both peak metamorphic phases and deformation fabric elements (Figure 4, Table 2), such that phase equilibria modeling efforts assume presence of fluids during the prograde metamorphism (e.g., Arai et al., 2015; Ramírez-Salazar et al., 2021). These mechanisms could explain sample 801-8B and 801-4 where there are significant numbers of subgrain boundaries' misorientation axes plotted at the $\langle a \rangle$ direction (Figure 6), indicating dislocation creep via prism $\langle c \rangle$ slip systems.

In misorientation axes plots, a band of sample 715-7 (see below) and samples 718-1, 720-4, 726-1, and 802-5 show strong signals of prism $\langle a \rangle$ slip, and much weaker signals of prism $\langle c \rangle$ slip (Figure 6). These patterns are in conflict with the prism $\langle c \rangle$ slip dominance inferred from their quartz CPO patterns (Figure 5). Findings from sample 715-7 may provide an explanation for such a conflict and show how a prism $\langle c \rangle$ type quartz CPO could form at temperatures consistent with activation of prism $\langle a \rangle$ slip in quartz

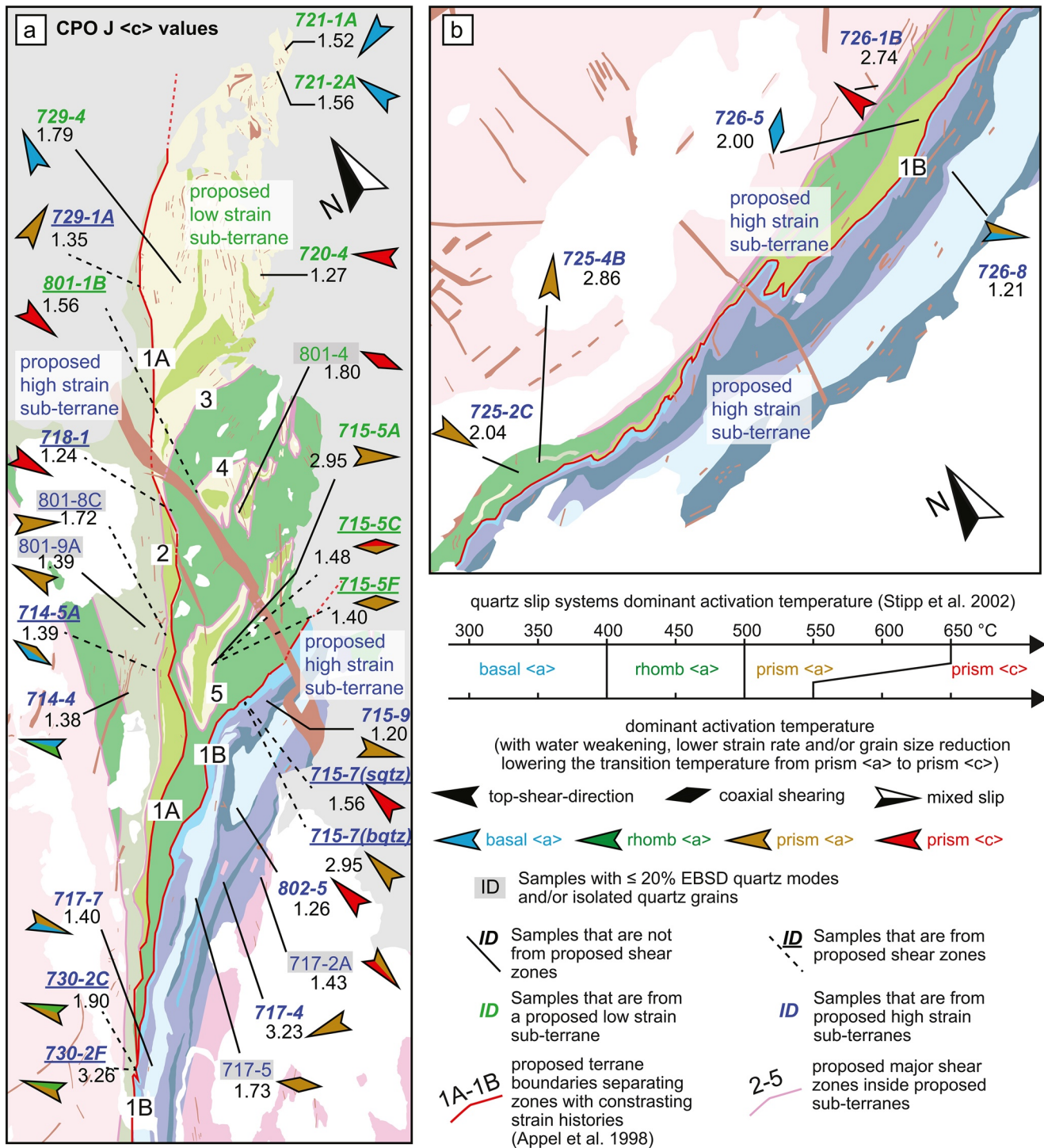


Figure 8.

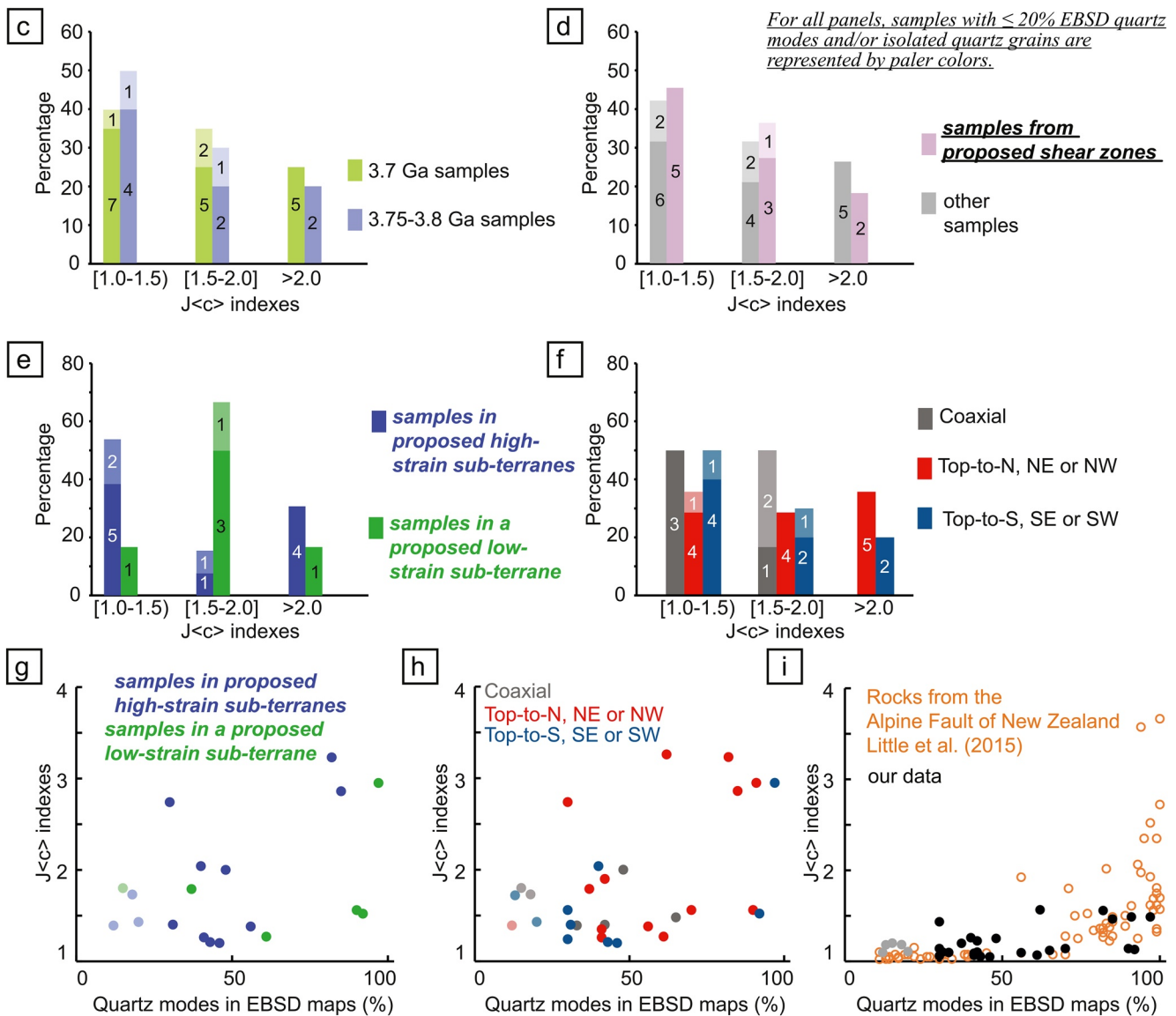


Figure 8. Continued

(Figures 5–7a). There, a band (715-7sqtz) with relatively small, elongated-shaped quartz grains (with a volume-weighted mean of diameters of $\sim 84 \mu\text{m}$) as well as high Fe-amphibole modal percentage (15 vol%) yields prism $\langle c \rangle$ quartz CPO, whereas another band (715-7bqtz) with bigger, polygonal- or ameboid-shaped quartz grains (with a volume-weighted mean of diameters of $\sim 166 \mu\text{m}$) and a lower Fe-amphibole modal

Figure 8. Sample locations and quartz CPO texture index statistics. (a and b) Sample locations and their J $\langle c \rangle$ indexes (J-index of c-axis pole figure). The blue or green texts are sample names, which are color-coded based on their relationships to the proposed subterrane (Appel et al., 1998). See Figures S2b and S2c for clearer visualization of locations of samples relative to proposed shear zones and subterrane. Samples with bold text are those show quartz aggregates or bands and/or $\geq 30\%$ quartz modes in EBSD maps. Samples with regular text in gray boxes are those with $\leq 20\%$ quartz modes and/or isolated quartz grains in EBSD maps (Figure S4). Black numbers are J $\langle c \rangle$ values of quartz c-axis pole figures. Lines indicate the locations of the samples (solid lines: samples not from a proposed shear zone; dashed: samples from a proposed shear zone [Appel et al., 1998; Nutman & Friend, 2009]). Some of these shear zones are coded to better support readers to check the locations of samples in Table 2. Arrows and diamonds are oriented parallel to the stretching lineations at the sample locations. Arrows point toward the top-shear-directions. Color codes for lithologies and map locations are given in Figure 1. We note that the dominant quartz slip systems of investigated sample could be far more uniform (i.e., mostly prism $\langle a \rangle$) than the CPO results presented here (cf. Figure 6). (c–f). Histograms showing the distributions of J $\langle c \rangle$ values grouped by different types of samples. (g and h) J $\langle c \rangle$ value of the quartz c-axis pole figure as a function of indexed quartz percentage in the EBSD map of each sample. These scatterplots show a weak increase of average CPO strengths toward higher quartz modal percentages in our samples. However, in contrast to amphibolite rocks from the Alpine Fault zone in New Zealand (i) (Little et al., 2015), the increase here is modest/negligible.

percentage (5 vol%) shows prism $\langle a \rangle$ slip (Figure 7a). There is no evidence indicating that these two bands were deformed during different events with different temperatures. We suggest that in 715-7sqtz, the smaller grain sizes as well as the presence of phyllosilicate phases may have localized stress at the microscopic grain scales. Higher stress may permit more activities of energetically unfavored slip systems (e.g., Chauve et al., 2017; Morales et al., 2011). Also, as mentioned before, water weakening could make activation of prism $\langle c \rangle$ slip in quartz easier (e.g., Blacic, 1975). These hypotheses are consistent with the differences in the distribution of misorientation axes of quartz subgrain boundaries in both areas of 715-7. In the inverse pole figures, 715-7sqtz shows a much stronger cluster at $\langle a \rangle$ direction compared to 715-7bqtz, suggesting higher activities in prism $\langle c \rangle$ slip systems in quartz of 715-7sqtz (Figure 6). Previous work found that a quartz CPO indicating prism $\langle a \rangle$ slip could be developed from growth (via grain boundary migration) of quartz grains with $[c]$ axes pointing to a sample's Y direction (i.e., a direction on the foliation plane that normal to the lineation direction) at the expense of quartz grains pointing toward other directions (e.g., Muto et al., 2011). Therefore, if the quartz grains are unfavorably oriented (e.g., Ceccato et al., 2017; Muto et al., 2011), and/or the growth of quartz grains is limited by other phases (e.g., Cross et al., 2017; Cyrpch et al., 2016), a prism $\langle a \rangle$ type quartz CPO may not develop even if subgrain boundaries indicate dominance of prism $\langle a \rangle$ slip (e.g., Ceccato et al., 2017). In 715-7sqtz, most quartz grains and all the Fe-amphiboles show alignment to the lineation direction (Figure 7a). This texture could have prevented the development of a prism $\langle a \rangle$ type CPO while both prism $\langle a \rangle$ and prism $\langle c \rangle$ slip were activated in quartz under amphibolite facies conditions. Such an explanation could also be applied to 718-1, 720-4, 726-1, and 802-5, where quartz bands/aggregates are interleaved with other phases, and all minerals are aligned with the lineation directions (Figure S4).

Lastly, samples 721-1A, 721-2A, 726-5, and 729-4 show clear dominance of the basal $\langle a \rangle$ slip system (Figures 5 and 8). In contrast, their misorientation axes of subgrain boundaries show dominance of prism $\langle a \rangle$ slip system in quartz. Weaker signals of slip on the basal planes are also present (Figure 6). A later, low-temperature deformation (e.g., a retrogressive event) that overprinted earlier high-temperature fabrics is possible (although no textural evidence for this was found). Findings from 721-1A and 721-2A (Figures 5–7b) may offer another explanation for the apparent mismatch between the dominant slip systems determined by two methods. In 721-1A and 721-2A, quartz grains show equant, polygonal shapes. Other than extraordinarily few subgrain boundaries, there is little intracrystalline deformation (i.e., lattice orientation of the crystal [represented by colors in Figure 7b] shows negligible variation within the grain boundary). Such patterns imply postdeformational recovery at or near the deformational temperatures (e.g., Heilbronner & Tullis, 2002; Trimby et al., 1998; Tullis & Yund, 1989). During postdeformational recovery, positions of (sub)grain boundaries and the associated dislocations may change to minimize the stored energy, leading to annealing of subgrain boundaries, formation of new grain boundaries, as well as grain boundary migration which forms equant, polygonal shapes for quartz (e.g., Borthwick et al., 2014; Heilbronner & Tullis, 2002; Trimby et al., 1998) (for comparisons between preannealing quartz and annealed quartz, please see Heilbronner and Tullis [2002], Trimby et al. [1998], and Tullis and Yund [1989]). The annealing process, which can reduce the density of subgrain boundaries, could be more prominent in certain types of subgrain boundaries. Controlling factors include the annealing temperatures and the slip systems associated with the subgrain boundaries (e.g., Borthwick et al., 2014; V Borthwick & Piazzolo, 2010). Therefore, it is possible that samples 721-1A and 721-2A have been deformed with activation of both basal $\langle a \rangle$ and prism $\langle a \rangle$ slip systems in quartz, with the peak deformational temperatures matching lower amphibolite facies conditions. Postdeformational recovery under lower amphibolite facies to greenschist facies conditions may have preferentially moved the dislocations associated with the basal $\langle a \rangle$ slip system, accentuating the basal $\langle a \rangle$ type signal in CPO patterns for these samples. In contrast, dislocations associated with prism $\langle a \rangle$ slip system may be harder to annihilate under similar conditions, forming the majority of preserved subgrain boundaries. In all Isua supracrustal belt samples, we find that most quartz grains have small to zero intracrystalline distortion, whereas the density of subgrain boundaries in the majority of quartz grains is low (Figure S4) (see Kruhl and Peternell [2002] for examples of subgrain boundary density in annealed quartz grains). Therefore, we interpret that all Isua samples have recorded postdeformational recovery to various degrees, possibly under greenschist to amphibolite facies conditions.

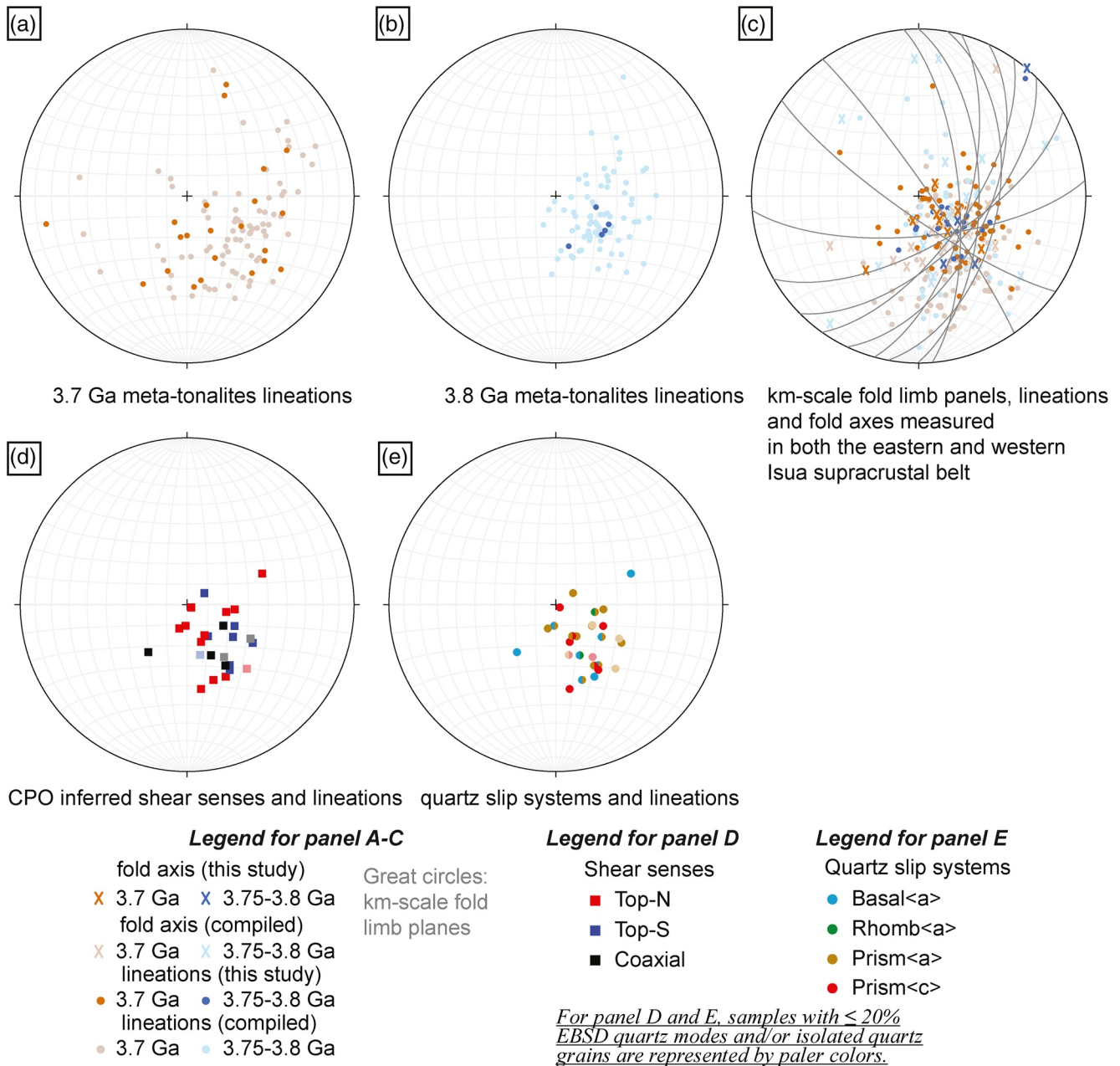
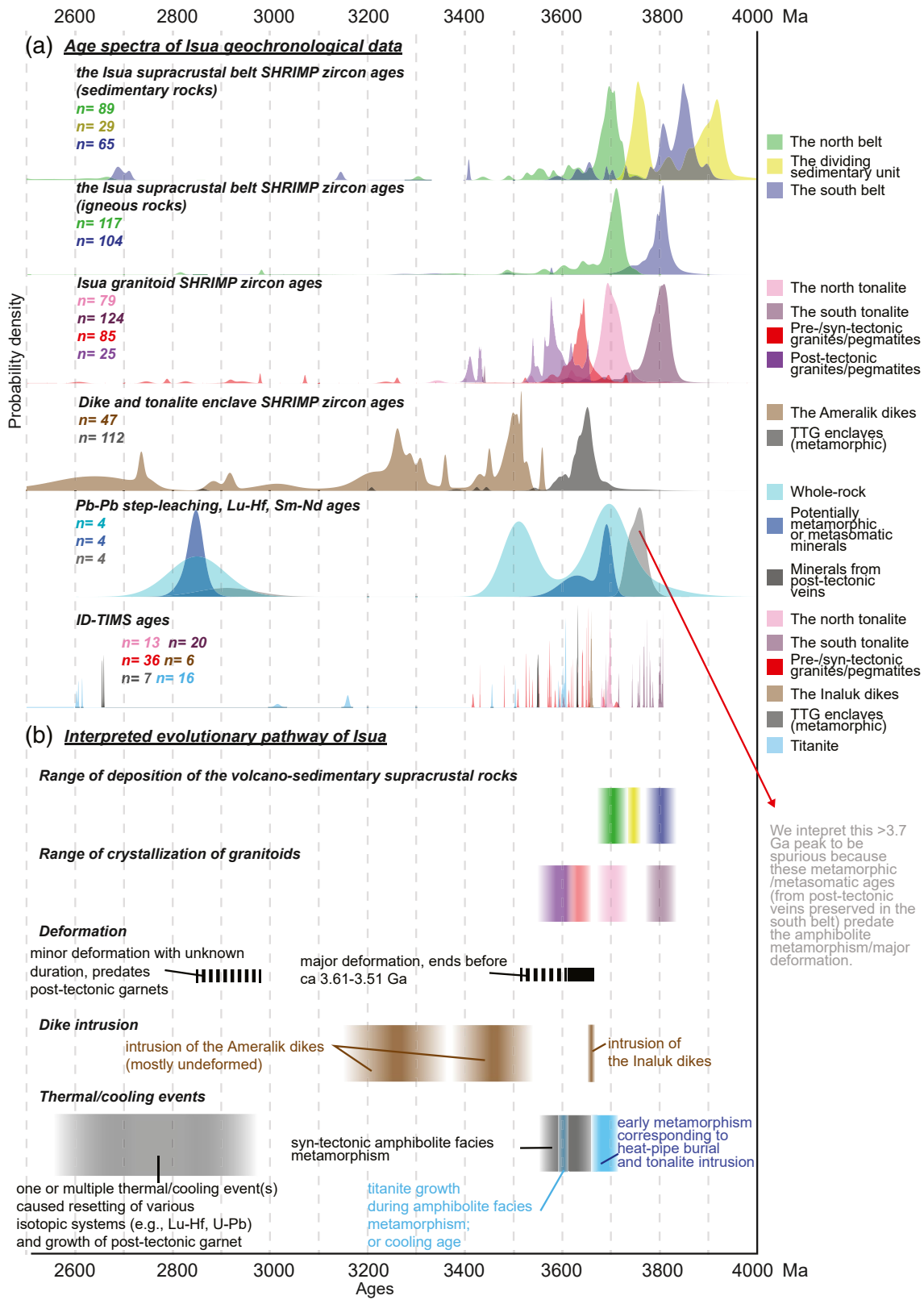


Figure 9. Stereonets showing the stretching lineations and fold axes measured across the belt and adjacent metatonalites (a–c) and their relationships with interpreted shear senses and dominant quartz slip systems as indicated by pole figures (d and e). Data sources: lineation and fold axis (this study; James, 1976; Nutman & Friend, 2009); interpreted shear senses (this study); dominant quartz slip systems (this study); fold limb plane data (Webb et al., 2020).

In keeping with the above discussions, we suggest that the dominant quartz slip systems activated in these samples are not only temperature-dependent, but also reflect other metamorphic/deformational conditions such as water content, presence of other phases, or postdeformational annealing. These complexities may explain the large diversity in quartz CPO patterns (Figure 5) and the high similarities in quartz subgrain boundaries' misorientation axis records (Figure 6). We interpret that basal $\langle a \rangle$, prism $\langle a \rangle$ and prism $\langle c \rangle$ slip observed in the quartz CPOs of Isua samples are consistent with deformation under peak temperatures of $\sim 500^\circ\text{C}$ – 650°C (i.e., amphibolite facies condition) in hydrous environments (Figures 3, 5, 6, 8a, and 8b). This interpretation is in accordance with the observed pre/syn-tectonic amphibolite facies mineral assemblages (Figure 4; Table 1, also Ramírez-Salazar



et al. [2021]). Deformation could have been followed by static, postdeformational recovery at similar and/or lower temperatures.

The interpreted deformation and postdeformation annealing conditions are consistent with the observed syn-tectonic garnets (Table 1; Figure 4), the $\sim 550^{\circ}\text{C}$ garnet-biotite temperature estimates (Rollinson, 2002 and references therein), and the $\sim 540^{\circ}\text{C}$ – 600°C estimates from phase equilibria modeling and cation-exchange thermobarometry on the prograde metamorphic paragenesis (Ramírez-Salazar et al., 2021). Similarly, a later static metamorphism event at $<540^{\circ}\text{C}$ or retrogression at $<500^{\circ}\text{C}$ (see Ramírez-Salazar et al. [2021]) could also promote postdeformational recovery as discussed above. The deformation temperatures ($\sim 500^{\circ}\text{C}$ – 650°C) from our results correspond to ~ 24 km depth (Ramírez-Salazar et al., 2021) assuming a geothermal gradient of $\sim 21^{\circ}\text{C}$ – $27^{\circ}\text{C}/\text{km}$, comparable with other Archean records (Brown & Johnson, 2018) and subducting slabs in relatively warm subduction systems (Chi & Reed, 2008; Zheng et al., 2016). The calculated geothermal gradient and interpreted deformation conditions may reflect local settings during (1) a small fraction of “heat-pipe” cooling history when the deformation occurred (i.e., ca. 3.7–3.6 Ga), and/or (2) during the predicted ca. 3.66–3.61 Ga plate-breaking/subduction. In the first scenario, the cold geotherm versus what is expected from Archean heat flow (nearly double of the present-day values, assuming conductive cooling only) (e.g., Jaupart, 2006; Jaupart & Mareschal, 2010) reflects the chilling effect of the rapid burial of cooled, hydrous surface volcanic rocks (Moore & Webb, 2013). Such conditions in combination with predicted radial constriction in response to volcanic burial (e.g., Bland & McKinnon, 2016; Schenk & Bulmer, 1998) would have produced the observed metamorphism and deformation. In the second scenario, the plate-breaking/subduction event would have recycled most of the Eoarchean crust and strongly shortened the rest (e.g., Beall et al., 2018). In response to crustal recycling, proto-subduction zones would have developed, where collisional deformation and a cold geotherm are expected.

5.3. A New P-T-t-d Pathway for the Isua Supracrustal Belt

Our results show that the geology of the Isua supracrustal belt and adjacent tonalites can be viably interpreted by the following P-T-t-d evolution pathway (Figure 10) (in chronological order):

1. Eruption and deposition of voluminous ca. 3.8 Ga supracrustal materials onto older lithosphere in a marine setting as fed by the partially molten mantle in heat-pipe settings
2. Intrusion of ca. 3.8 Ga tonalite at depths of ~ 15 km. The tonalite was generated by partial melting of cold, hydrated lower crust (Kamber et al., 2003) in response to downward burial due to deposition of the thick ca. 3.8 Ga supracrustal sequence
3. Deposition of the “dividing sedimentary unit” onto ca. 3.8 Ga materials before ca. 3.7 Ga, followed by eruption and deposition of voluminous ca. 3.7 Ga supracrustal materials
4. Intrusion of ca. 3.7 Ga tonalite into the ca. 3.7 Ga supracrustal materials at depths of ~ 15 km as a result of melting of the deeper lithosphere in response to burial
5. Potentially early metamorphism of the ca. 3.8 Ga rocks at ca. 3.7 Ga in response to burial of the 3.8 Ga crust under potentially ~ 20 km-thick ca. 3.7 Ga crustal materials, generating metamorphic magnetites with ca. 3.7 Ga ages (Frei et al., 1999)
6. Intrusion of the Inaluk dikes at ca. 3.66 Ga (Crowley, 2003; Crowley et al., 2002)
7. Regional deformation and metamorphism at ca. 3.66 to 3.61 Ga (or potentially extending as late as 3.5 Ga) in association with dramatic thinning, stretching, and shearing, which generated the observed macro and microstructures, syn-tectonic amphibolite metamorphism, and granite intrusions (Figure 9a). This event may reflect contraction during heat-pipe downward advection in response to the reduction of spherical area, or a plate-breaking/subduction event that marked the end of heat-pipe cooling and the initiation of plate tectonics (Beall et al., 2018; Moore & Webb, 2013; Webb et al., 2020)

Figure 10. A compilation of geochronology data from the Isua supracrustal belt and adjacent metatonalites, followed by our preferred evolution history of the belt and metatonalites (see text for detailed discussion). We note that compiled Pb-Pb step-leaching ages, Lu-Hf ages, and Sm-Nd ages are from rocks or minerals sampled from the south belt. Abbreviations: SHRIMP, sensitive high-resolution ion microprobe; ID-TIMS, Isotopic dilution thermal ionization mass spectrometry. Raw age data (spot ages) are presented in Figure S6. Data sources are: Blichert-Toft and Frei (2001), Compston et al. (1986), Crowley (2003), Crowley et al. (2002), Frei and Rosing (2001), Frei et al. (2004), Frei et al. (1999), Friend and Nutman (2010), Friend et al. (2002), Gruau et al. (1996), Hanmer et al. (2002), Kamber et al. (2005), Nutman and Friend (2009), Nutman et al. (1996, 1997, 1999, 2000, 2002, 2004, 2007, 2009, 2013b), and Rosing and Frei (1999).

8. Cooling at ca. 3.6 Ga from amphibolite facies conditions recorded by titanite (Figure 9a), that is, if such ages are interpreted as cooling ages rather than growth ages (Figure 10b) (Crowley, 2003; Crowley et al., 2002). Post deformational recovery in quartz followed the cessation of regional deformation
9. Intrusion of the ca. 3.5–3.2 Ga Ameralik dikes in combination with partial resetting of various isotopic systems. Rifting of a primordial southwest Greenland craton may have led to crustal thinning and intrusion of the Ameralik dikes (e.g., Nutman et al., 2004). Alternatively, these dikes may reflect remnants of melt transportation pipes feeding younger, unspecified (or unexposed) supracrustal rocks (e.g., Gill & Bridgwater, 1979)
10. One or multiple thermal/cooling event(s) within the ca. 3.0–2.6 Ga period, which produced the observed posttectonic garnets and metasomatic minerals (Figures 4c, 10a, and S7) (Ramírez-Salazar et al., 2021; Rollinson, 2003), further postdeformational recovery in quartz, amphibolite metamorphism in the Ameralik dikes (Nutman et al., 2004), minor deformation (Nutman, 1986; Nutman et al., 2002), and partial resetting of various isotopic systems (Figure 10). This event(s) has been associated with tectonic and thermal responses of multiple terrane collision events interpreted from the geology of adjacent areas within Meso and Neoproterozoic time (Nutman et al., 2015b)

6. Conclusions

Our results show that the pre-3.5 Ga structural patterns of the Isua supracrustal belt are not consistent with Eoarchean plate tectonic models (e.g., Komiya et al., 1999; Nutman & Friend, 2009). In contrast, the geology of the belt is consistent with the predictions of a heat-pipe tectonic model (Webb et al., 2020). Thus, the belt is not an exception to the growing consensus that global plate tectonics did not start until ca. 3.2 Ga or later (Condie & Puetz, 2019; Naeraa et al., 2012; M. Tang et al., 2016). Similar heat-pipe tectonic regimes have been proposed for other cooling terrestrial bodies in the solar system (Lenardic, 2018; Moore et al., 2017; Stern et al., 2017). Specifically, it is thought that after the magma ocean stage, heat-pipe cooling dominated and subsequently transitioned to plate tectonics (in Earth's case) or to a cold stagnant-lid regime (Mars, Mercury, the Moon, and Venus). Our results do not preclude the possibility of pre-3.2 Ga plate tectonic deformation, as the main ca. 3.6 Ga phase of deformation across the supracrustal belt could potentially reflect a plate-breaking event. Existing compilations of Eoarchean geology (Nutman et al., 2015a) and evidence from zircon isotopes can be interpreted to indicate a geodynamic transition at ca. 3.6 Ga (Bell et al., 2014; Mueller & Wooden, 2012; Ranjan et al., 2020). Such an event may have led to episodic stagnant-lid cooling punctuated by short-lived subduction (e.g., Van Kranendonk, 2010), such that the ca. 3.6–3.2 Ga interval might represent a stagnant lid regime prior to transition to plate tectonics during ca. 3.2–2.5 Ga (e.g., Condie & Puetz, 2019; M. Tang et al., 2016).

Acknowledgments

The authors thank Dr. Hanwen Dong, Mr. Jiagsong Chen and Miss Lily Chiu for their assistance in thin section preparation. The authors thank Dr. Richard Walshaw and Mr. Y. F. Chan Frankie for their assistance in acquiring images, geochemical and microstructural data from scanning electron microscopes. The authors are grateful to Dr. Nick Roberts and Dr. Constantin Balica for their constructive reviews which helped improve the original manuscript. The authors specially thank Dr. Nick Roberts for suggesting using misorientation analyses on the EBSD dataset. Sample collection was supported by a Seed Fund for Basic Research grant (project code: 201610159002) to A. A. G. Webb and T. Müller as well as start-up funds to A. A. G. Webb, both from the University of Hong Kong. Analytical work was supported by the Hong Kong Research Grants Council via a General Research Fund grant (project code: 17305718) to AAGW.

Data Availability Statement

Data sets for this research are included in this paper (Tables 1 and 2), the supporting information file, and references. Data sets generated by this research can also be found at the DataHub repository (<https://datahub.hku.hk/>) following the link <https://doi.org/10.25442/hku.12932830.v2>.

References

- Allwood, A. C., Rosing, M. T., Flannery, D. T., Hurowitz, J. A., & Heirweh, C. M. (2018). Reassessing evidence of life in 3,700-million-year-old rocks of Greenland. *Nature*, 563(7730), 241–244. <https://doi.org/10.1038/s41586-018-0610-4>
- Alsop, G., & Holdsworth, R. (1999). Vergence and facing patterns in large-scale sheath folds. *Journal of Structural Geology*, 21(10), 1335–1349. [https://doi.org/10.1016/S0191-8141\(99\)00099-1](https://doi.org/10.1016/S0191-8141(99)00099-1)
- Alsop, G., & Holdsworth, R. (2012). The three dimensional shape and localisation of deformation within multilayer sheath folds. *Journal of Structural Geology*, 44, 110–128. <https://doi.org/10.1016/j.jsg.2012.08.015>
- Appel, P. W., Fedo, C. M., Moorbath, S., & Myers, J. S. (1998). Recognizable primary volcanic and sedimentary features in a low-strain domain of the highly deformed, oldest known (-3.7-3.8 Gyr) Greenstone Belt, Isua, West Greenland. *Terra Nova*, 10(2), 57–62. <https://doi.org/10.1046/j.1365-3121.1998.00162.x>
- Arai, T., Omori, S., Komiya, T., & Maruyama, S. (2015). Intermediate P/T-type regional metamorphism of the Isua Supracrustal Belt, southern west Greenland: The oldest Pacific-type orogenic belt? *Tectonophysics*, 662, 22–39. <https://doi.org/10.1016/j.tecto.2015.05.020>
- Bachmann, F., Hielscher, R., & Schaeben, H. (2010). Texture analysis with MTEX—free and open source software toolbox. Proceedings solid state phenomena (Vol. 160, pp. 63–68). Trans Tech Publications. <https://doi.org/10.4028/www.scientific.net/SSP.160.63>

- Barth, N. C., Hacker, B. R., Seward, G. G., Walsh, E. O., Young, D., & Johnston, S. (2010). Strain within the ultrahigh-pressure Western Gneiss region of Norway recorded by quartz CPOs. *Geological Society, London, Special Publications*, 335(1), 663–685. <https://doi.org/10.1144/SP335.27>
- Beall, A., Moresi, L., & Cooper, C. M. (2018). Formation of cratonic lithosphere during the initiation of plate tectonics. *Geology*, 46(6), 487–490. <https://doi.org/10.1130/G39943.1>
- Bell, E. A., Harrison, T. M., Kohl, I. E., & Young, E. D. (2014). Eoarchean crustal evolution of the Jack Hills zircon source and loss of Hadean crust. *Geochimica et Cosmochimica Acta*, 146, 27–42. <https://doi.org/10.1016/j.gca.2014.09.028>
- Blacic, J. D. (1975). Plastic-deformation mechanisms in quartz: The effect of water. *Tectonophysics*, 27(3), 271–294. [https://doi.org/10.1016/0040-1951\(75\)90021-9](https://doi.org/10.1016/0040-1951(75)90021-9)
- Bland, M. T., & McKinnon, W. B. (2016). Mountain building on Io driven by deep faulting. *Nature Geoscience*, 9(6), 429–432. <https://doi.org/10.1038/ngeo2711>
- Blichert-Toft, J., & Frei, R. (2001). Complex Sm-Nd and Lu-Hf isotope systematics in metamorphic garnets from the Isua supracrustal belt, West Greenland. *Geochimica et Cosmochimica Acta*, 65(18), 3177–3189. [https://doi.org/10.1016/S0016-7037\(01\)00680-9](https://doi.org/10.1016/S0016-7037(01)00680-9)
- Borthwick, V. E., & Piazzolo, S. (2010). Post-deformational annealing at the subgrain scale: Temperature dependent behaviour revealed by in-situ heating experiments on deformed single crystal halite. *Journal of Structural Geology*, 32(7), 982–996. <https://doi.org/10.1016/j.jsg.2010.06.006>
- Borthwick, V. E., Piazzolo, S., Evans, L., Griera, A., & Bons, P. D. (2014). What happens to deformed rocks after deformation? A refined model for recovery based on numerical simulations. *Geological Society, London, Special Publications*, 394(1), 215–234. <https://doi.org/10.1144/SP394.11>
- Brenner, A. R., Fu, R. R., Evans, D. A., Smirnov, A. V., Trubko, R., & Rose, I. R. (2020). Paleomagnetic evidence for modern-like plate motion velocities at 3.2 Ga. *Science Advances*, 6(17), eaaz8670. <https://doi.org/10.1126/sciadv.aaz8670>
- Bridgwater, D., McGregor, V., & Myers, J. (1974). A horizontal tectonic regime in the Archaean of Greenland and its implications for early crustal thickening. *Precambrian Research*, 1(3), 179–197. [https://doi.org/10.1016/0301-9268\(74\)90009-6](https://doi.org/10.1016/0301-9268(74)90009-6)
- Brown, M., & Johnson, T. (2018). Secular change in metamorphism and the onset of global plate tectonics. *American Mineralogist*, 103(2), 181–196. <https://doi.org/10.2138/am-2018-6166>
- Bunge, H.-J. (2013). *Texture analysis in materials science: Mathematical methods*. Elsevier.
- Ceccato, A., Pennacchioni, G., Menegon, L., & Bestmann, M. (2017). Crystallographic control and texture inheritance during mylonitization of coarse grained quartz veins. *Lithos*, 290–291, 210–227. <https://doi.org/10.1016/j.lithos.2017.08.005>
- Chauve, T., Montagnat, M., Piazzolo, S., Journaux, B., Wheeler, J., Barou, F., et al. (2017). Non-basal dislocations should be accounted for in simulating ice mass flow. *Earth and Planetary Science Letters*, 473, 247–255. <https://doi.org/10.1016/j.epsl.2017.06.020>
- Chi, W.-C., & Reed, D. L. (2008). Evolution of shallow, crustal thermal structure from subduction to collision: An example from Taiwan. *Geological Society of America Bulletin*, 120(5–6), 679–690. <https://doi.org/10.1130/B26210.1>
- Collins, W. J., Van Kranendonk, M. J., & Teyssier, C. (1998). Partial convective overturn of Archaean crust in the east Pilbara Craton, Western Australia: Driving mechanisms and tectonic implications. *Journal of Structural Geology*, 20(9–10), 1405–1424. [https://doi.org/10.1016/S0191-8141\(98\)00073-X](https://doi.org/10.1016/S0191-8141(98)00073-X)
- Compston, W., Kinny, P., Williams, I., & Foster, J. (1986). The age and Pb loss behaviour of zircons from the Isua supracrustal belt as determined by ion microprobe. *Earth and Planetary Science Letters*, 80(1–2), 71–81. [https://doi.org/10.1016/0012-821X\(86\)90020-8](https://doi.org/10.1016/0012-821X(86)90020-8)
- Condie, K. C., & Puetz, S. J. (2019). Time series analysis of mantle cycles Part II: The geologic record in zircons, large igneous provinces and mantle lithosphere. *Geoscience Frontiers*, 10(4), 1327–1336. <https://doi.org/10.1016/j.gsf.2019.03.005>
- Cross, A. J., Hirth, G., & Prior, D. J. (2017). Effects of secondary phases on crystallographic preferred orientations in mylonites. *Geology*, 45(10), 955–958. <https://doi.org/10.1130/G38936>
- Crowley, J. (2003). U–Pb geochronology of 3810–3630 Ma granitoid rocks south of the Isua greenstone belt, Southern West Greenland. *Precambrian Research*, 126(3–4), 235–257. [https://doi.org/10.1016/S0301-9268\(03\)00097-4](https://doi.org/10.1016/S0301-9268(03)00097-4)
- Crowley, J., Myers, J., & Dunning, G. (2002). Timing and nature of multiple 3700–3600 Ma tectonic events in intrusive rocks north of the Isua greenstone belt, southern West Greenland. *Geological Society of America Bulletin*, 114(10), 1311–1325. [https://doi.org/10.1130/0016-7606\(2002\)114<1311:TANOMM>2.0.CO;2](https://doi.org/10.1130/0016-7606(2002)114<1311:TANOMM>2.0.CO;2)
- Cyprich, D., Piazzolo, S., Wilson, C. J., Luzin, V., & Prior, D. (2016). Rheology, microstructure and crystallographic preferred orientation of matrix containing a dispersed second phase: Insight from experimentally deformed ice. *Earth and Planetary Science Letters*, 449, 272–281. <https://doi.org/10.1016/j.epsl.2016.06.010>
- Drury, M. R., & Urai, J. L. (1990). Deformation-related recrystallization processes. *Tectonophysics*, 172(3–4), 235–253. [https://doi.org/10.1016/0040-1951\(90\)90033-5](https://doi.org/10.1016/0040-1951(90)90033-5)
- Dymek, R. F., Boak, J. L., & Brothers, S. C. (1988a). Titanian chondrodite-and titanian clinohumite-bearing metadunite from the 3800 Ma Isua supracrustal belt, West Greenland; chemistry, petrology and origin. *American Mineralogist*, 73(5–6), 547–558. <https://doi.org/10.1093/petrology/29.6.1353>
- Dymek, R. F., Brothers, S. C., & Schiffrins, C. M. (1988b). Petrogenesis of Ultramafic Metamorphic Rocks from the 3800-Ma Isua Supracrustal Belt, West Greenland. *Journal of Petrology*, 29(6), 1353–1397. <https://doi.org/10.1093/petrology/29.6.1353>
- Fedo, C. M. (2000). Setting and origin for problematic rocks from the >37 Ga Isua Greenstone Belt, southern west Greenland: Earth's oldest coarse clastic sediments. *Precambrian Research*, 101(1), 69–78. [https://doi.org/10.1016/S0301-9268\(99\)00100-X](https://doi.org/10.1016/S0301-9268(99)00100-X)
- Frei, R., Bridgwater, D., Rosing, M., & Stecher, O. (1999). Controversial Pb-Pb and Sm-Nd isotope results in the early Archean Isua (West Greenland) oxide iron formation: Preservation of primary signatures versus secondary disturbances. *Geochimica et Cosmochimica Acta*, 63(3–4), 473–488. [https://doi.org/10.1016/S0016-7037\(98\)00290-7](https://doi.org/10.1016/S0016-7037(98)00290-7)
- Frei, R., Polat, A., & Meibom, A. (2004). The Hadean upper mantle conundrum: Evidence for source depletion and enrichment from Sm-Nd, Re-Os, and Pb isotopic compositions in 3.71 Gy boninite-like metabasalts from the Isua Supracrustal Belt, Greenland. *Geochimica et Cosmochimica Acta*, 68(7), 1645–1660. <https://doi.org/10.1016/j.gca.2003.10.009>
- Frei, R., & Rosing, M. T. (2001). The least radiogenic terrestrial leads; implications for the early Archean crustal evolution and hydrothermal-metasomatic processes in the Isua Supracrustal Belt (West Greenland). *Earth and Planetary Science Letters*, 181(1–4), 47–66. [https://doi.org/10.1016/S0009-2541\(01\)00263-7](https://doi.org/10.1016/S0009-2541(01)00263-7)
- Friend, C. R. L., Bennett, V. C., & Nutman, A. P. (2002). Abyssal peridotites > 3,800 Ma from southern West Greenland: Field relationships, petrography, geochronology, whole-rock and mineral chemistry of dunite and harzburgite inclusions in the Itsaq Gneiss Complex. *Contributions to Mineralogy and Petrology*, 143(1), 71–92. <https://doi.org/10.1007/s00410-001-0332-7>
- Friend, C. R. L., & Nutman, A. P. (2005). Complex 3670–3500 Ma orogenic episodes superimposed on juvenile crust accreted between 3850 and 3690 Ma, Itsaq Gneiss Complex, southern West Greenland. *The Journal of Geology*, 113(4), 375–397. <https://doi.org/10.1086/430239>

- Friend, C. R. L., & Nutman, A. P. (2010). Eoarchean ophiolites? New evidence for the debate on the Isua supracrustal belt, southern West Greenland. *American Journal of Science*, 310(9), 826–861. <https://doi.org/10.2475/09.2010.04>
- Friend, C. R. L., & Nutman, A. P. (2011). Dunites from Isua, Greenland: A ca. 3720 Ma window into subcrustal metasomatism of depleted mantle. *Geology*, 39(7), 663–666. <https://doi.org/10.1130/G31904.1>
- Furnes, H., de Wit, M., Staudigel, H., Rosing, M., & Muehlenbachs, K. (2007). A vestige of Earth's oldest ophiolite. *Science*, 315(5819), 1704–1707. <https://doi.org/10.1126/science.1139170>
- Garbutt, J. M., & Teyssier, C. (1991). Prism<c> slip in the quartzites of the Oakhurst Mylonite Belt, California. *Journal of Structural Geology*, 13(6), 657–666. [https://doi.org/10.1016/0191-8141\(91\)90028-H](https://doi.org/10.1016/0191-8141(91)90028-H)
- Gardner, R. L., Piazzolo, S., Daczko, N. R., & Evans, L. (2019). Ductile Deformation Without Localization: Insights From Numerical Modeling. *Geochemistry, Geophysics, Geosystems*, 20(12), 5710–5726. <https://doi.org/10.1029/2019GC008633>
- Gauthiez-Putallaz, L., Nutman, A., Bennett, V., & Rubatto, D. (2020). Origins of high $\delta^{18}\text{O}$ in 3.7–3.6 Ga crust: A zircon and garnet record in Isua clastic metasedimentary rocks. *Chemical Geology*, 537, 119474. <https://doi.org/10.1016/j.chemgeo.2020.119474>
- Gerya, T. V., Stern, R. J., Baes, M., Sobolev, S. V., & Whattam, S. A. (2015). Plate tectonics on the Earth triggered by plume-induced subduction initiation. *Nature*, 527(7577), 221–225. <https://doi.org/10.1038/nature15752>
- Ghosh, S., & Ramberg, H. (1976). Reorientation of inclusions by combination of pure shear and simple shear. *Tectonophysics*, 34(1–2), 1–70. [https://doi.org/10.1016/0040-1951\(76\)90176-1](https://doi.org/10.1016/0040-1951(76)90176-1)
- Gill, R., & Bridgwater, D. (1979). Early Archaean basic magmatism in West Greenland: The geochemistry of the Ameralik dykes. *Journal of Petrology*, 20(4), 695–726. <https://doi.org/10.1093/petrology/20.4.695>
- Gonçalves, C. C., Gonçalves, L., & Hirth, G. (2015). The effects of quartz recrystallization and reaction on weak phase interconnection, strain localization and evolution of microstructure. *Journal of Structural Geology*, 71, 24–40. <https://doi.org/10.1016/j.jsg.2014.11.010>
- Gruau, G., Rosing, M., Bridgwater, D., & Gill, R. (1996). Resetting of Sm-Nd systematics during metamorphism of >3.7-Ga rocks: Implications for isotopic models of early Earth differentiation. *Chemical Geology*, 133(1–4), 225–240. [https://doi.org/10.1016/S0009-2541\(96\)00092-7](https://doi.org/10.1016/S0009-2541(96)00092-7)
- Halfpenny, A., Prior, D. J., & Wheeler, J. (2012). Electron backscatter diffraction analysis to determine the mechanisms that operated during dynamic recrystallisation of quartz-rich rocks. *Journal of Structural Geology*, 36, 2–15. <https://doi.org/10.1016/j.jsg.2012.01.001>
- Hanmer, S., & Greene, D. C. (2002). A modern structural regime in the Paleoproterozoic (~3.6 Ga); Isua Greenstone Belt, southern West Greenland. *Tectonophysics*, 346(3–4), 201–222. [https://doi.org/10.1016/S0040-1951\(02\)00029-X](https://doi.org/10.1016/S0040-1951(02)00029-X)
- Hanmer, S., Hamilton, M. A., & Crowley, J. L. (2002). Geochronological constraints on Paleoproterozoic thrust-nappe and Neoproterozoic accretionary tectonics in southern West Greenland. *Tectonophysics*, 350(3), 255–271. [https://doi.org/10.1016/S0040-1951\(02\)00120-8](https://doi.org/10.1016/S0040-1951(02)00120-8)
- Hansen, V. (2007). Subduction origin on early Earth: A hypothesis. *Geology*, 35(12), 1059–1062. <https://doi.org/10.1130/G24202A.1>
- Heilbronner, R., & Tullis, J. (2002). The effect of static annealing on microstructures and crystallographic preferred orientations of quartzites experimentally deformed in axial compression and shear. *Geological Society, London, Special Publications*, 200(1), 191–218. <https://doi.org/10.1144/GSL.SP.2001.200.01.12>
- Heilbronner, R., & Tullis, J. (2006). Evolution of c axis pole figures and grain size during dynamic recrystallization: Results from experimentally sheared quartzite. *Journal of Geophysical Research: Solid Earth*, 111(B10). <https://doi.org/10.1029/2005JB004194>
- Hieiss, J., Bennett, V. C., & Nutman, A. P. (2011). Archaean fluid-assisted crustal cannibalism recorded by low $\delta^{18}\text{O}$ and negative $\epsilon_{\text{HT}}(\text{T})$ isotopic signatures of West Greenland granite zircon. *Contribution to Mineralogy and Petrology*, 161(6), 1027–1050. <https://doi.org/10.1007/s00410-010-0578-z>
- Hippert, J. (1994). Microstructures and c-axis fabrics indicative of quartz dissolution in sheared quartzites and phyllonites. *Tectonophysics*, 229(3–4), 141–163. [https://doi.org/10.1016/0040-1951\(94\)90026-4](https://doi.org/10.1016/0040-1951(94)90026-4)
- Hoffmann, J. E., Nagel, T. J., Munker, C., Naeraa, T., & Rosing, M. T. (2014). Constraining the process of Eoarchean TTG formation in the Itsaq Gneiss Complex, southern West Greenland. *Earth and Planetary Science Letters*, 388, 374–386. <https://doi.org/10.1016/j.epsl.2013.11.050>
- Hopkins, M., Harrison, T. M., & Manning, C. E. (2008). Low heat flow inferred from >4 Gyr zircons suggests Hadean plate boundary interactions. *Nature*, 456(7221), 493–496. <https://doi.org/10.1038/nature07465>
- Hunter, N. J., Hasalová, P., Weinberg, R. F., & Wilson, C. J. (2016). Fabric controls on strain accommodation in naturally deformed mylonites: The influence of interconnected micaceous layers. *Journal of Structural Geology*, 83, 180–193. <https://doi.org/10.1016/j.jsg.2015.12.005>
- James, P. R. (1976). Deformation of the Isua block, West Greenland: A remnant of the earliest stable continental crust. *Canadian Journal of Earth Sciences*, 13(6), 816–823. <https://doi.org/10.1139/e76-084>
- Jaupart, C. (2006). Archean thermal regime and stabilization of the cratons. *Archean Geodynamics and Environments*, 164, 61. <https://doi.org/10.1029/164GM06>
- Jaupart, C., & Mareschal, J.-C. (2010). *Heat generation and transport in the Earth*. Cambridge University Press. Retrieved from <https://doi.org/10.1017/CBO9780511781773>
- Johnson, T. E., Brown, M., Gardiner, N. J., Kirkland, C. L., & Smithies, R. H. (2017). Earth's first stable continents did not form by subduction. *Nature*, 543(7644), 239–243. <https://doi.org/10.1038/nature21383>
- Johnson, T. E., Brown, M., Kaus, B. J. P., & VanTongeren, J. A. (2014). Delamination and recycling of Archaean crust caused by gravitational instabilities. *Nature Geoscience*, 7(1), 47–52. <https://doi.org/10.1038/ngeo2019>
- Kaczmarek, M. A., Reddy, S. M., Nutman, A. P., Friend, C. R. L., & Bennett, V. C. (2016). Earth's oldest mantle fabrics indicate Eoarchean subduction. *Nature Communications*, 7. <https://doi.org/10.1038/ncomms10665>
- Kamber, B. S., Collerson, K. D., Moorbath, S., Whitehouse, M. J. (2003). Inheritance of early Archaean Pb-isotope variability from long-lived Hadean protocrust. *Contributions to Mineralogy and Petrology*, 145(1), 25–46. <https://doi.org/10.1007/s00410-002-0429-7>
- Kamber, B. S., Whitehouse, M. J., Bolhar, R., & Moorbath, S. (2005). Volcanic resurfacing and the early terrestrial crust: Zircon U–Pb and REE constraints from the Isua Greenstone Belt, southern West Greenland. *Earth and Planetary Science Letters*, 240(2), 276–290. <https://doi.org/10.1016/j.epsl.2005.09.037>
- Keto, L., & Kurki, J. (1967). Report on the exploration activity at Isua 1967. *Kryolitselskabet Øresund A/S prospecting report*. reports lodged at the Geological Survey of Denmark and Greenland (Vol. 20024). Kryolitselskabet Øresund A/S.
- Kilian, R., Heilbronner, R., & Stünitz, H. (2011). Quartz grain size reduction in a granitoid rock and the transition from dislocation to diffusion creep. *Journal of Structural Geology*, 33(8), 1265–1284. <https://doi.org/10.1016/j.jsg.2011.05.004>
- Komiya, T., Hayashi, M., Maruyama, S., & Yurimoto, H. (2002). Intermediate-P/T type Archaean metamorphism of the Isua supracrustal belt: Implications for secular change of geothermal gradients at subduction zones and for Archaean plate tectonics. *American Journal of Science*, 302(9), 806–826. <https://doi.org/10.2475/ajs.302.9.806>

- Komiya, T., Maruyama, S., Masuda, T., Nohda, S., Hayashi, M., & Okamoto, K. (1999). Plate tectonics at 3.8–3.7 Ga: Field evidence from the Isua Accretionary Complex, southern West Greenland. *Journal of Geology*, *107*(5), 515–554. <https://doi.org/10.1086/314371>
- Kruhl, J. H. (1998). Prism and basal-plane parallel subgrain boundaries in quartz: A microstructural geothermobarometer-Reply. *Journal of Metamorphic Geology*, *16*(1), 142–146. <https://doi.org/10.1111/j.1525-1314.1998.00063.x>
- Kruhl, J. H., & Petermann, M. (2002). The equilibration of high-angle grain boundaries in dynamically recrystallized quartz: The effect of crystallography and temperature. *Journal of Structural Geology*, *24*(6–7), 1125–1137. [https://doi.org/10.1016/S0191-8141\(01\)00096-7](https://doi.org/10.1016/S0191-8141(01)00096-7)
- Lanari, P., Vidal, O., De Andrade, V., Dubacq, B., Lewin, E., Grosch, E. G., & Schwartz, S. (2014). XMapTools: A MATLAB[®]-based program for electron microprobe X-ray image processing and geothermobarometry. *Computers & Geosciences*, *62*, 227–240. <https://doi.org/10.1016/j.cageo.2013.08.010>
- Law, R. D. (1990). Crystallographic fabrics: A selective review of their applications to research in structural geology. *Geological Society, London, Special Publications*, *54*(1), 335–352. <https://doi.org/10.1144/GSL.SP.1990.054.01.30>
- Law, R. D. (2014). Deformation thermometry based on quartz *c*-axis fabrics and recrystallization microstructures: A review. *Journal of Structural Geology*, *66*, 129–161. <https://doi.org/10.1016/j.jsg.2014.05.023>
- Law, R. D., Searle, M., & Simpson, R. (2004). Strain, deformation temperatures and vorticity of flow at the top of the Greater Himalayan Slab, Everest Massif, Tibet. *Journal of the Geological Society*, *161*(2), 305–320. <https://doi.org/10.1144/0016-764903-047>
- Lenardic, A. (2018). The diversity of tectonic modes and thoughts about transitions between them. *Philosophical Transactions of the Royal Society A: Mathematical, Physical and Engineering Sciences*, *376*(2132), 20170416. <https://doi.org/10.1098/rsta.2017.0416>
- Little, T. A., Prior, D. J., Toy, V. G., & Lindroos, Z. R. (2015). The link between strength of lattice preferred orientation, second phase content and grain boundary migration: A case study from the Alpine Fault zone, New Zealand. *Journal of Structural Geology*, *81*, 59–77. <https://doi.org/10.1016/j.jsg.2015.09.004>
- Lloyd, G. E., Farmer, A. B., & Mainprice, D. (1997). Misorientation analysis and the formation and orientation of subgrain and grain boundaries. *Tectonophysics*, *279*(1–4), 55–78. [https://doi.org/10.1016/S0040-1951\(97\)00115-7](https://doi.org/10.1016/S0040-1951(97)00115-7)
- Moore, W. B., Simon, J. I., & Webb, A. A. G. (2017). Heat-pipe planets. *Earth and Planetary Science Letters*, *474*, 13–19. <https://doi.org/10.1016/j.epsl.2017.06.015>
- Moore, W. B., & Webb, A. A. G. (2013). Heat-pipe Earth. *Nature*, *501*(7468), 501–505. <https://doi.org/10.1038/nature12473>
- Morales, L. F., Mainprice, D., Lloyd, G. E., & Law, R. D. (2011). Crystal fabric development and slip systems in a quartz mylonite: An approach via transmission electron microscopy and viscoplastic self-consistent modelling. *Geological Society, London, Special Publications*, *360*(1), 151–174. <https://doi.org/10.1144/SP360.9>
- Mueller, P. A., & Wooden, J. L. (2012). Trace element and Lu-Hf systematics in Hadean-Archean detrital zircons: Implications for crustal evolution. *The Journal of Geology*, *120*(1), 15–29. <https://doi.org/10.1086/662719>
- Muto, J., Hirth, G., Heilbronner, R., & Tullis, J. (2011). Plastic anisotropy and fabric evolution in sheared and recrystallized quartz single crystals. *Journal of Geophysical Research*, *116*(B2). <https://doi.org/10.1029/2010JB007891>
- Myers, J. S. (2001). Protoliths of the 3.8–3.7 Ga Isua greenstone belt, west Greenland. *Precambrian Research*, *105*(2–4), 129–141. [https://doi.org/10.1016/S0301-9268\(00\)00108-X](https://doi.org/10.1016/S0301-9268(00)00108-X)
- Naeraa, T., Schersten, A., Rosing, M. T., Kemp, A. I. S., Hoffmann, J. E., Kokfelt, T. F., & Whitehouse, M. J. (2012). Hafnium isotope evidence for a transition in the dynamics of continental growth 3.2 Gyr ago. *Nature*, *485*(7400), 627–630. <https://doi.org/10.1038/nature11140>
- Nagel, T. J., Hoffmann, J. E., & Münker, C. (2012). Generation of Eoarchean tonalite-trondhjemite-granodiorite series from thickened mafic arc crust. *Geology*, *40*(4), 375–378. <https://doi.org/10.1130/G32729.1>
- Neumann, B. (2000). Texture development of recrystallised quartz polycrystals unravelled by orientation and misorientation characteristics. *Journal of Structural Geology*, *22*(11–12), 1695–1711. [https://doi.org/10.1016/S0191-8141\(00\)00060-2](https://doi.org/10.1016/S0191-8141(00)00060-2)
- Nutman, A. P. (1986). The early Archaean to Proterozoic history of the Isukasia area, southern West Greenland. *Grønlands Geologiske Undersøgelse Bulletin*, *154*, 1–80.
- Nutman, A. P., & Bennett, V. C. (2019). The 3.9–3.6 Ga Itsaq Gneiss Complex of Greenland. *Earth's oldest rocks*. (2nd ed., pp. 375–399). Berlin: Elsevier. Retrieved from <https://doi.org/10.1016/B978-0-444-63901-1.00017-4>
- Nutman, A. P., Bennett, V. C., & Friend, C. R. L. (2013a). The emergence of the Eoarchean proto-arc: Evolution of a c. 3700 Ma convergent plate boundary at Isua, southern West Greenland. *Geological Society, London, Special Publications*, *389*(1), 113. <https://doi.org/10.1144/SP389.5>
- Nutman, A. P., Bennett, V. C., & Friend, C. R. L. (2015a). Proposal for a continent 'Itsaqia'amalgamated at 3.66 Ga and rifted apart from 3.53 Ga: Initiation of a Wilson Cycle near the start of the rock record. *American Journal of Science*, *315*(6), 509–536. <https://doi.org/10.2475/06.2015.01>
- Nutman, A. P., Bennett, V. C., Friend, C. R. L., Hidaka, H., Yi, K., Lee, S. R., & Kamiuchi, T. (2013b). The Itsaq Gneiss Complex of Greenland: Episodic 3900 to 3660 Ma juvenile crust formation and recycling in the 3660 to 3600 Ma Isukasian orogeny. *American Journal of Science*, *313*(9), 877–911. <https://doi.org/10.2475/09.2013.03>
- Nutman, A. P., Bennett, V. C., Friend, C. R. L., & McGregor, V. R. (2000). The early Archaean Itsaq Gneiss Complex of southern West Greenland: The importance of field observations in interpreting age and isotopic constraints for early terrestrial evolution. *Geochimica et Cosmochimica Acta*, *64*(17), 3035–3060. [https://doi.org/10.1016/S0016-7037\(99\)00431-7](https://doi.org/10.1016/S0016-7037(99)00431-7)
- Nutman, A. P., Bennett, V. C., Friend, C. R. L., & Norman, M. D. (1999). Meta-igneous (non-gneissic) tonalites and quartz-diorites from an extensive ca. 3800 Ma terrain south of the Isua supracrustal belt, southern West Greenland: Constraints on early crust formation. *Contributions to Mineralogy and Petrology*, *137*(4), 364–388. <https://doi.org/10.1007/s004100050556>
- Nutman, A. P., Bennett, V. C., Friend, C. R. L., & Rosing, M. T. (1997). ~3710 and ≥3790 Ma volcanic sequences in the Isua (Greenland) supracrustal belt; structural and Nd isotope implications. *Chemical Geology*, *141*(3–4), 271–287. [https://doi.org/10.1016/S0009-2541\(97\)00084-3](https://doi.org/10.1016/S0009-2541(97)00084-3)
- Nutman, A. P., Bennett, V. C., Friend, C. R. L., Van Kranendonk, M. J., & Chivas, A. R. (2016). Rapid emergence of life shown by discovery of 3,700-million-year-old microbial structures. *Nature*, *537*(7621), 535–538. <https://doi.org/10.1038/nature19355>
- Nutman, A. P., Bennett, V. C., Friend, C. R. L., Van Kranendonk, M. J., Rothacker, L., & Chivas, A. R. (2019). Cross-examining Earth's oldest stromatolites: Seeing through the effects of heterogeneous deformation, metamorphism and metasomatism affecting Isua (Greenland)~3700 Ma sedimentary rocks. *Precambrian Research*, *331*, 105347. <https://doi.org/10.1016/j.precamres.2019.105347>
- Nutman, A. P., Bennett, V. C., Friend, C. R. L., & Yi, K. (2020). Eoarchean contrasting ultra-high-pressure to low-pressure metamorphisms (< 250 to > 1000°C/GPa) explained by tectonic plate convergence in deep time. *Precambrian Research*, *344*, 105770. <https://doi.org/10.1016/j.precamres.2020.105770>

- Nutman, A. P., Bennett, V. C., Friend, C. R. L., Yi, K., & Lee, S. R. (2015b). Mesoarchean collision of Kapisilik terrane 3070 Ma juvenile arc rocks and >3600 Ma Isukasia terrane continental crust (Greenland). *Precambrian Research*, 258, 146–160. <https://doi.org/10.1016/j.precamres.2014.12.013>
- Nutman, A. P., & Bridgwater, D. (1986). Early Archaean Amitsoq tonalites and granites of the Isukasia area, southern West Greenland: Development of the oldest-known sial. *Contributions to Mineralogy and Petrology*, 94(2), 137–148. <https://doi.org/10.1007/BF00592931>
- Nutman, A. P., & Collerson, K. D. (1991). Very early Archean crustal-accretion complexes preserved in the North Atlantic craton. *Geology*, 19(8), 791–794. [https://doi.org/10.1130/0091-7613\(1991\)019<0791:VEACAC>2.3.CO;2](https://doi.org/10.1130/0091-7613(1991)019<0791:VEACAC>2.3.CO;2)
- Nutman, A. P., & Friend, C. R. L. (2009). New 1:20,000 scale geological maps, synthesis and history of investigation of the Isua supracrustal belt and adjacent orthogneisses, southern West Greenland: A glimpse of Eoarchean crust formation and orogeny. *Precambrian Research*, 172(3–4), 189–211. <https://doi.org/10.1016/j.precamres.2009.03.017>
- Nutman, A. P., Friend, C. R. L., & Bennett, V. C. (2002). Evidence for 3650–3600 Ma assembly of the northern end of the Itsaq Gneiss Complex, Greenland: Implication for early Archaean tectonics. *Tectonics*, 21(1), 5–1–5–28. <https://doi.org/10.1029/2000TC001203>
- Nutman, A. P., Friend, C. R. L., Bennett, V. C., & McGregor, V. R. (2004). Dating of the Ameralik dyke swarms of the Nuuk district, southern West Greenland: Mafic intrusion events starting from c. 3510 Ma. *Journal of the Geological Society*, 161(3), 421–430. <https://doi.org/10.1144/0016-764903-043>
- Nutman, A. P., Friend, C. R. L., Bennett, V. C., Wright, D., & Norman, M. D. (2010). ≥3700 Ma pre-metamorphic dolomite formed by microbial mediation in the Isua supracrustal belt (W. Greenland): Simple evidence for early life? *Precambrian Research*, 183(4), 725–737. <https://doi.org/10.1016/j.precamres.2010.08.006>
- Nutman, A. P., Friend, C. R. L., Horie, K., & Hidaka, H. (2007). The Itsaq Gneiss Complex of Southern West Greenland and the Construction of Eoarchean Crust at Convergent Plate Boundaries. *Earth's Oldest Rocks*, Developments in Precambrian Geology, 15, 1st ed., 187–218. [https://doi.org/10.1016/S0166-2635\(07\)15033-7](https://doi.org/10.1016/S0166-2635(07)15033-7)
- Nutman, A. P., Friend, C. R. L., & Paxton, S. (2009). Detrital zircon sedimentary provenance ages for the Eoarchean Isua supracrustal belt southern West Greenland: Juxtaposition of an imbricated ca. 3700 Ma juvenile arc against an older complex with 3920–3760 Ma components. *Precambrian Research*, 172(3–4), 212–233. <https://doi.org/10.1016/j.precamres.2009.03.019>
- Nutman, A. P., McGregor, V. R., Friend, C. R. L., Bennett, V. C., & Kinny, P. D. (1996). The Itsaq Gneiss Complex of southern west Greenland; The world's most extensive record of early crustal evolution (3900–3600 Ma). *Precambrian Research*, 78(1–3), 1–39. [https://doi.org/10.1016/0301-9268\(95\)00066-6](https://doi.org/10.1016/0301-9268(95)00066-6)
- Okudaira, T., Takeshita, T., Hara, I., & Ando, J.-i. (1995). A new estimate of the conditions for transition from basal <a> to prism [c] slip in naturally deformed quartz. *Tectonophysics*, 250(1–3), 31–46. [https://doi.org/10.1016/0040-1951\(95\)00039-4](https://doi.org/10.1016/0040-1951(95)00039-4)
- O'Neill, C., & Debaille, V. (2014). The evolution of Hadean–Eoarchean geodynamics. *Earth and Planetary Science Letters*, 406, 49–58. <https://doi.org/10.1016/j.epsl.2014.08.034>
- Pearce, J. A., & Reagan, M. K. (2019). Identification, classification, and interpretation of boninites from Anthropocene to Eoarchean using Si-Mg-Ti systematics. *Geosphere*, 15(4), 1008–1037. <https://doi.org/10.1130/GES01661.1>
- Pease, V., Percival, J., Smithies, H., Stevens, G., & Van Kranendonk, M. (2008). When did plate tectonics begin? Evidence from the orogenic record. *When Did Plate Tectonics Begin on Planet Earth?*, Geological Society of America Special Paper, 440, (199–228). The Geological Society of America.
- Polat, A., Appel, P. W. U., & Fryer, B. J. (2011). An overview of the geochemistry of Eoarchean to Mesoarchean ultramafic to mafic volcanic rocks, SW Greenland: Implications for mantle depletion and petrogenetic processes at subduction zones in the early Earth. *Gondwana Research*, 20(2–3), 255–283. <https://doi.org/10.1016/j.gr.2011.01.007>
- Polat, A., & Hofmann, A. W. (2003). Alteration and geochemical patterns in the 3.7–3.8 Ga Isua greenstone belt, West Greenland. *Precambrian Research*, 126(3–4), 197–218. [https://doi.org/10.1016/S0301-9268\(03\)00095-0](https://doi.org/10.1016/S0301-9268(03)00095-0)
- Price, R. A. (1972). The distinction between displacement and distortion in flow, and the origin of diachronism in tectonic overprinting in orogenic belts. *Proceedings of the 24th International Geological Congress*, (545–551). International Geological Congress.
- Prior, D. (1999). Problems in determining the misorientation axes, for small angular misorientations, using electron backscatter diffraction in the SEM. *Journal of Microscopy*, 195(3), 217–225. <https://doi.org/10.1046/j.1365-2818.1999.00572.x>
- Rahl, J. M., & Skemer, P. (2016). Microstructural evolution and rheology of quartz in a mid-crustal shear zone. *Tectonophysics*, 680, 129–139. <https://doi.org/10.1016/j.tecto.2016.05.022>
- Ramírez-Salazar, A., Muller, T., Piazzolo, S., Webb, A. A. G., Zuo, J., Hauzenberger, C., et al. (2021). Tectonics of the Isua supracrustal belt. Part 1: P-T-X-d constraints of a poly-metamorphic terrane. *Tectonics*, 40, e2020TC006516. <https://doi.org/10.1029/2020TC006516>
- Ranjan, S., Upadhyay, D., Pruseth, K. L., & Nanda, J. K. (2020). Detrital zircon evidence for change in geodynamic regime of continental crust formation 3.7–3.6 billion years ago. *Earth and Planetary Science Letters*, 538, 116206. <https://doi.org/10.1016/j.epsl.2020.116206>
- Rey, P. F., Coltice, N., & Flament, N. (2014). Spreading continents kick-started plate tectonics. *Nature*, 513(7518), 405–408. <https://doi.org/10.1038/nature13728>
- Rollinson, H. (2002). The metamorphic history of the Isua greenstone belt, West Greenland. *Geological Society, London, Special Publications*, 199(1), 329–350. <https://doi.org/10.1144/GSL.SP.2002.199.01.16>
- Rollinson, H. (2003). Metamorphic history suggested by garnet-growth chronologies in the Isua Greenstone Belt, West Greenland. *Precambrian Research*, 126(3–4), 181–196. [https://doi.org/10.1016/S0301-9268\(03\)00094-9](https://doi.org/10.1016/S0301-9268(03)00094-9)
- Rosing, M. T., & Frei, R. (1999). Late Archaean metasomatism and kyanite formation in the >3700 Ma Isua supracrustals, west Greenland. *Journal of Conference Abstracts*, 4(1), 144.
- Schenk, P. M., & Bulmer, M. H. (1998). Origin of mountains on Io by thrust faulting and large-scale mass movements. *Science*, 279(5356), 1514–1517. <https://doi.org/10.1126/science.279.5356.1514>
- Schmid, S., & Casey, M. (1986). Complete fabric analysis of some commonly observed quartz c-axis patterns. *Geophysical Monograph*, 36(6), 263–286. <https://doi.org/10.1029/GM036p0263>
- Skemer, P., Katayama, I., Jiang, Z., & Karato, S.-i. (2005). The misorientation index: Development of a new method for calculating the strength of lattice-preferred orientation. *Tectonophysics*, 411(1–4), 157–167. <https://doi.org/10.1016/j.tecto.2005.08.023>
- Smithies, R., Champion, D., Van Kranendonk, M., & Hickman, A. (2007). Geochemistry of volcanic rocks of the northern Pilbara Craton, Western Australia. *Geological Survey of Western Australia Report*, 104.1–47.
- Starnes, J. K., Long, S. P., Gordon, S. M., Zhang, J., & Soignard, E. (2020). Using quartz fabric intensity parameters to delineate strain patterns across the Himalayan Main Central thrust. *Journal of Structural Geology*, 131, 103941. <https://doi.org/10.1016/j.jsg.2019.103941>
- Stern, R. J., Gerya, T., & Tackley, P. J. (2017). Stagnant lid tectonics: Perspectives from silicate planets, dwarf planets, large moons, and large asteroids. *Geoscience Frontiers*, 9(1), 103–119. <https://doi.org/10.1016/j.gsf.2017.06.004>

- Stipp, M., StuEñitz, H., Heilbronner, R., & Schmid, S. M. (2002). The eastern Tonale fault zone: A 'natural laboratory' for crystal plastic deformation of quartz over a temperature range from 250 to 700°C. *Journal of Structural Geology*, 24(12), 1861–1884. [https://doi.org/10.1016/S0191-8141\(02\)00035-4](https://doi.org/10.1016/S0191-8141(02)00035-4)
- Szilas, K., Kelemen, P. B., & Rosing, M. T. (2015). The petrogenesis of ultramafic rocks in the >3.7 Ga Isua supracrustal belt, southern West Greenland: Geochemical evidence for two distinct magmatic cumulate trends. *Gondwana Research*, 28(2), 565–580. <https://doi.org/10.1016/j.gr.2014.07.010>
- Tang, C., Webb, A., Moore, W., Wang, Y., Ma, T., & Chen, T. (2020). Breaking Earth's shell into a global plate network. *Nature Communications*, 11(1), 1–6. <https://doi.org/10.1038/s41467-020-17480-2>
- Tang, M., Chen, K., & Rudnick, R. L. (2016). Archean upper crust transition from mafic to felsic marks the onset of plate tectonics. *Science*, 351(6271), 372–375. <https://doi.org/10.1126/science.aad5513>
- Toy, V. G., Prior, D. J., & Norris, R. J. (2008). Quartz fabrics in the Alpine Fault mylonites: Influence of pre-existing preferred orientations on fabric development during progressive uplift. *Journal of Structural Geology*, 30(5), 602–621. <https://doi.org/10.1016/j.jsg.2008.01.001>
- Trimby, P. W., Prior, D. J., and Wheeler, J. (1998). Grain boundary hierarchy development in a quartz mylonite. *Journal of Structural Geology*, 20(7), 917–935. [https://doi.org/10.1016/S0191-8141\(98\)00026-1](https://doi.org/10.1016/S0191-8141(98)00026-1)
- Tullis, J., Christie, J. M., & Griggs, D. T. (1973). Microstructures and preferred orientations of experimentally deformed quartzites. *Geological Society of America Bulletin*, 84(1), 297–314. [https://doi.org/10.1130/0016-7606\(1973\)84<297:MAPOOE>2.0.CO;2](https://doi.org/10.1130/0016-7606(1973)84<297:MAPOOE>2.0.CO;2)
- Tullis, J., & Yund, R. A. (1989). Hydrolytic weakening of quartz aggregates: The effects of water and pressure on recovery. *Geophysical Research Letters*, 16(11), 1343–1346. <https://doi.org/10.1029/GL016101p01343>
- Ulrich, S., & Mainprice, D. (2005). Does cation ordering in omphacite influence development of lattice-preferred orientation? *Journal of Structural Geology*, 27(3), 419–431. <https://doi.org/10.1016/j.jsg.2004.11.003>
- van de Löcht, J., Hoffmann, J., Li, C., Wang, Z., Becker, H., Rosing, M. T., et al. (2018). Earth's oldest mantle peridotites show entire record of late accretion. *Geology*, 46(3), 199–202. <https://doi.org/10.1130/G39709.1>
- van de Löcht, J., Hoffmann, J., Rosing, M., Sprung, P., & Münker, C. (2020). Preservation of Eoarchean mantle processes in ~3.8 Ga peridotite enclaves in the Itsaq Gneiss Complex, southern West Greenland. *Geochimica et Cosmochimica Acta*, 280, 1–25. <https://doi.org/10.1016/j.gca.2020.03.043>
- Van Kranendonk, M. J. (2010). Two types of Archean continental crust: Plume and plate tectonics on early Earth. *American Journal of Science*, 310(10), 1187–1209. <https://doi.org/10.2475/10.2010.01>
- Vollmer, F. W. (1990). An application of eigenvalue methods to structural domain analysis. *Geological Society of America Bulletin*, 102(6), 786–791. [https://doi.org/10.1130/0016-7606\(1990\)102<0786:AAOEMT>2.3.CO;2](https://doi.org/10.1130/0016-7606(1990)102<0786:AAOEMT>2.3.CO;2)
- Webb, A. A. G., Müller, T., Zuo, J., Haproff, P. J., & Ramirez-Salazar, A. (2020). A non-plate tectonic model for the Eoarchean Isua supracrustal belt. *Lithosphere*, 12(1), 166–179. <https://doi.org/10.1130/L1130.1>
- Wheeler, J. (2009). The preservation of seismic anisotropy in the Earth's mantle during diffusion creep. *Geophysical Journal International*, 178(3), 1723–1732. <https://doi.org/10.1111/j.1365-246X.2009.04241.x>
- White, R. V., Crowley, J. L., & Myers, J. S. (2000). Earth's oldest well-preserved mafic dyke swarms in the vicinity of the Isua greenstone belt, southern West Greenland. *Geology of Greenland Survey Bulletin*, 186, 65–72. <https://doi.org/10.34194/ggub.v186.5217>
- Woodcock, N. (1977). Specification of fabric shapes using an eigenvalue method. *Geological Society of America Bulletin*, 88(9), 1231–1236. [https://doi.org/10.1130/0016-7606\(1977\)88<1231:S0FSUA>2.0.CO;2](https://doi.org/10.1130/0016-7606(1977)88<1231:S0FSUA>2.0.CO;2)
- Xypolias, P., & Koukouvelas, I. (2001). Kinematic vorticity and strain rate patterns associated with ductile extrusion in the Chelmos Shear Zone (External Hellenides, Greece). *Tectonophysics*, 338(1), 59–77. [https://doi.org/10.1016/S0040-1951\(01\)00125-1](https://doi.org/10.1016/S0040-1951(01)00125-1)
- Yao, Z., Qin, K., Wang, Q., & Xue, S. (2019). Weak B-Type Olivine Fabric Induced by Fast Compaction of Crystal Mush in a Crustal Magma Reservoir. *Journal of Geophysical Research: Solid Earth*, 124(4), 3530–3556. <https://doi.org/10.1029/2018JB016728>
- Zawaski, M. J., Kelly, N. M., Orlandini, O. F., Nichols, C. I., Allwood, A. C., & Mojzsis, S. J. (2020). Reappraisal of purported ca. 3.7 Ga stromatolites from the Isua Supracrustal Belt (West Greenland) from detailed chemical and structural analysis. *Earth and Planetary Science Letters*, 545, 116409. <https://doi.org/10.1016/j.epsl.2020.116409>
- Zhang, Y., Hobbs, B., & Jessell, M. (1994). The effect of grain-boundary sliding on fabric development in polycrystalline aggregates. *Journal of Structural Geology*, 16(9), 1315–1325. [https://doi.org/10.1016/0191-8141\(94\)90072-8](https://doi.org/10.1016/0191-8141(94)90072-8)
- Zheng, Y., Chen, R., Xu, Z., & Zhang, S. (2016). The transport of water in subduction zones. *Science China Earth Sciences*, 59(4), 651–682. <https://doi.org/10.1007/s11430-015-5258-4>
- Zibra, I., Lu, Y., Clos, F., Winberg, R. F., Peternell, M., Wingate, M. T. D., et al. (2020). Regional-scale polydiapirism predating the Neoproterozoic Yilgarn Orogeny. *Tectonophysics*, 779, 228–375. <https://doi.org/10.1016/j.tecto.2020.228375>